Structural design of plate fixation implants for Open Wedge High Tibial Osteotomy

by

João Óscar Ornelas Costa Freitas

Thesis submitted to
Faculdade de Engenharia da Universidade do Porto (FEUP)

MSc degree in Mechanical Engineering

Supervision from

Prof. Jorge Américo Oliveira Pinto Belinha (FEUP),

Prof. Renato Manuel Natal Jorge (FEUP) and

Prof. Adélio Justino Vilaça (ICBAS)

Porto, June 2017

I thank my parents, brother and sister for their tireless and precious support over the years, and my girlfriend, for being an amazing person.

Structural design of fixation implants for Open Wedge High Tibial Osteotomy

by

João Óscar Ornelas Costa Freitas

Supervision from

Professor Jorge Américo Oliveira Pinto Belinha (FEUP),

professor Renato Manuel Natal Jorge (FEUP) and professor

Adélio Justino Vilaça (ICBAS)

Abstract

The Open Wedge High Tibial Osteotomy (OWHTO) is a well-established procedure to treat varus/valgus deformities of the knee, with or without uni-compartmental arthrosis. Nevertheless, the stability of the various fixation implants used in this procedure has not been previously demonstrated. In the present work, new designs for those implants are ultimately studied and structurally analysed. Three-dimensional models of the tibia were reconstructed from computed tomography images (DICOM's), obtained from the anonymized medical images of MIMCS® database. Both the osteotomy with different cutting lengths and with the fixation models will be simulated through computational processing using different numerical methodologies. The main objective is to achieve or find optimal configurations for the fixation implant, capable to provide the necessary structural resistance, during and after the surgery (intraoperative and postoperative situations). The structural analysis will be performed using the well-known finite element method and a newly developed class of discrete numerical methods: the meshless methods (RPIM); comparing both methods (secondary objective).

Key words: Open wedge high tibial osteotomy (OWHTO), fixation implant, structural analysis, meshless methods, biomechanics, varus deformity

Structural design of fixation implants for Open Wedge High Tibial Osteotomy

by

João Óscar Ornelas Costa Freitas

Supervision from

Professor Jorge Américo Oliveira Pinto Belinha (FEUP),

professor Renato Manuel Natal Jorge (FEUP) and professor

Adélio Justino Vilaça (ICBAS)

Resumo

A osteotomia tibial superior aberta é uma cirurgia bem estabelecida para tratar deformações varus/valgus do joelho, com ou sem artrose unicompartimental. No entanto, a estabilidade estrutural dos mais variados implantes utilizados ainda não foi demonstrada. No presente trabalho, novos designs para estes implantes são estudados e estruturalmente analisados. Os modelos tridimensionais da tíbia utilizados foram reconstruídos a partir de imagens tomográficas computorizadas (DICOM's), retiradas do conjunto de imagens médicas anonimizadas da base de dados do MIMICS®. Neste trabalho, a osteotomia com diferentes comprimentos no corte e os implantes são alvos de simulação, utilizando metodologias numéricas diferentes. O objetivo principal é obter ou descobrir configurações ótimas dos implantes de fixação, capazes de fornecer a resistência estrutural necessária, durante e após a cirurgia. A análise estrutural será feita utilizando o método de elementos finitos, deveras conhecido, e por recurso a métodos numéricos discretos recentemente desenvolvidos: os métodos sem malha (RPIM); comparando ambos os métodos (objetivo secundário).

Palavras-chave: Open wedge high tibial osteotomy (OWHTO), fixation implant, structural analysis, meshless methods, biomechanics, varus deformity

Acknowledgments

I really want to thank Professor Jorge Belinha, not only for his unique capacity in solving all kinds of problems/challenges that inevitably appeared, but also for his full availability and effort, during this present work.

I also want to thank professors Renato Natal Jorge and Adélio Justino Vilaça for the accompaniment and support and, still, I thank Marco Marques for his availability in sharing his knowledge, making the learning of the software programs required, very fast.

To my family, in special my parents, I thank all their love, incentive, dedication and their tireless support, that gave me the opportunity of having a superior course outdoors. Despite of not being easy, all the effort was worth.

Finally, I want to thank to Liliana Ferreira, for the affection, love, companionship and support through the whole process.

Agradecimentos

Quero agradecer ao Professor Jorge Belinha, não apenas pela sua única capacidade em solucionar todo o tipo de problemas/desafios que foram inevitavelmente aparecendo, mas também pela sua total disponibilidade e empenho, ao longo de todo este trabalho.

Agradeço também aos professores Renato Natal Jorge e Adélio Justino Vilaça pelo acompanhamento e apoio e, ainda, agradeço ao Marco Marques pela sua disponibilidade em divulgar os seus conhecimentos, possibilitando a rápida aprendizagem de como manusear os programas que me foram fornecidos.

À minha família, em especial os meus pais, agradeço todo o seu amor, incentivo, dedicação e o incansável esforço, para que fosse possível eu ter a oportunidade de tirar um curso superior fora de casa. Apesar de não ter sido fácil, valeu todo o esforço.

Finalmente, quero agradecer à Liliana Ferreira, pelo carinho, amor, companheirismo e apoio ao longo de todo este processo.

Institutional Acknowledgments

The author truly acknowledges the work conditions provided by the Applied Mechanics Division (SMAp) of the department of mechanical engineering (DEMec) of FEUP and by the inter-institutional project “BoneSys – Bone biochemical and biomechanic integrated modeling: addressing remodeling, disease and therapy dynamics” funded by the “Laboratório Associado de Energia Transportes e Aeronáutica” (UID/EMS/50022/2013) and by the project NORTE-01-0145-FEDER-000022 – SciTech – Science and Technology for Competitive and Sustainable Industries, co-financed by Programa Operacional Regional do Norte (NORTE2020), through Fundo Europeu de Desenvolvimento Regional (FEDER).

Table of Contents

List of figures

List of tables

1 Introduction

Over the last 20 years, the evaluation of healthcare interventions from both efficacy and value standpoints has become increasingly important as all nations face pressure to control rising healthcare costs. Osteoarthritis (OA) is a leading cause of disability and affects more people than any other joint disease. The worldwide market for knee replacement surgery approaches €5,7 billion annually, and the number of procedures is expected to grow rapidly as the prevailing demographic ages in the industrialized nationsc The High Tibial Osteotomy is a well-established procedure to treat, in the majority of cases, knee osteoarthritis on the medial compartment (MCOA). Other procedures, such as the Arthroplasty, are, still, more extensively used to treat this problem. Nevertheless, HTO is considered the most cost-effective option when treating MCOA in patients under 60 years old, (W. B. Smith et al. 2017) and the optimization of their fixation implants has, consequently, a huge importance in the future.

1.1 Finite Element Method

Finite Element Method (FEM) is one of the computational methods that has received wide acceptance in orthopaedics research. In this technique, three dimensional models of bone-implant systems are converted into finite elements (with simulated physiological loads applied) to analyse and predict the outcome of surgery. (Raja Izaham et al. 2012)(Weng et al. 2017) From the collection of all those elements, a mesh is created which, aside of containing them, also finds the connectivity relations between each element. After the problem has been discretised, the field function of the domain is interpolated within each element in terms of an assumed approximation function (shape function). The approximation function is used because the real solution of the element's field variable, represented by the mentioned differential equations, is normally more complex. Finally, the global domain equation system is obtained by assembling of each element's local equation system. (Reddy's 2005)

However, despite this numerical method has been the most accepted by the scientific community in recent years, there are other methods recently developed capable of meeting the design needs of an engineer and, in some cases, capable of obtaining a better reproduction of the studied phenomenon. For example, a lack of precision is found in the FEM when considering large deformations, complex geometries or fractures propagation. These shortcomings are caused by its own nature, by building a mesh that hinders the treatment of discontinuities which do not coincide with the original meshlines. Meshless methods are supported by a formulation that eliminates the necessity of the mesh, constructing the approximation exclusively in terms of an arbitrary nodal set of nodes. (Reddy's 2005)

1.2 Meshless Methods

In the last few years meshless methods for numerically solving partial differential equations came into focus of interest, especially in the computational mechanics community. In meshless methods, the nodes can be arbitrary distributed, once the field functions are approximated within an influence-domain rather than an element. In opposition to the no-overlap rule between

elements in the Finite Element Method (FEM), in meshless methods the influence-domains may and must overlap each other. (Belinha 2014)

1.2.1 Relevant Meshless Methods History

The initially created meshless methods used approximation functions, since it produces smoother solutions, the implementation of the influence-domain concept was easier and the background integration scheme was nodal independent. The first meshless method using the Moving Least Square approximants (MLS) in the construction of the approximation function was the Diffuse Element Method (DEM). (Nayroles, Touzot, and Villon 1992) The MLS was proposed by Lancaster and Salkauskas (Lancaster and Salkauskas 1981) for surface fitting. Belytschko evolved the DEM and developed one of the most popular meshless methods, the Element Free Galerkin Method (EFGM), which uses a nodal independent background integration mesh. (Belytschko and Tabbara 1996) One of the oldest meshless methods is the Smooth Particle Hydrodynamics Method (SPH) (Monaghan 1977), which is in the origin of the Reproducing Kernel Particle Method (RKPM). (Liu, Jun, and Zhang 1995)

Other very popular approximant meshless methods are: The Meshless Local Petrov-Galerkin Method (MLPG) (Atluri and Zhu 1998) evolving later into the Method of the Finite Spheres (MFS) (KJ 2000), the Reproducing Kernel Particle Method (RKPM), the Finite Point Method (FPM) (Oñate et al. 1996) or the Radial Basis Function Method (RBFM) (Kansa 1990) that uses radial basis functions, respecting a Euclidean norm, to approximate the variable fields within the entire domain or in small domains.

Even though the mentioned meshless methods have been successfully applied in computational mechanics, there were several problems not completely solved. One of these problems, and perhaps the most important unsolved issue, was the lack of the Kronecker delta property, $\varphi_i(x_j) \neq \delta_{ij}$, on the approximation functions, which difficult the imposition of essential and natural boundary conditions. The Point Interpolation Method (PIM) (G. Wang and Liu 2001) and the Radial Point Interpolation Method (RPIM) are recent developments that solve this problem. (Belinha 2014)

More recently, the development of the concept of natural neighbours (the Voronoï Diagram concept) combined with RPIM resulted in the creation of the Natural Neighbour Radial Point Interpolation Method (NNRPIM). (Belinha 2014) This relevant method will be also described in the present work, but not used in the analysis due to the lack of time.

1.2.2 Radial Point Interpolation Method

The RPIM emerged as a development of PIM (G. Wang and Liu 2001). The technique consisted in constructing polynomial interpolants, possessing the Kronecker delta property, based only on a group of arbitrarily distributed points. However, this technique has too many numerical problems, for instance the perfect alignment of the nodes produces singular solutions in the interpolation function construction process. The RPIM was proposed in 2002 (J. G. Wang and Liu 2002b)(J. G. Wang and Liu 2002a), and suggests a combination of the polynomial basis functions used in PIM with Radial Basis Functions (RBF) to construct the shape functions. With this combination, the method is stabilized. (Belinha 2014)

The RPIM uses the influence-domain concept and the nodal connectivity is established by the overlap of each influence-domain (generating sparse and banded stiffness matrices, more adequate to complex geometry problems, by opposition to the global domain concept). (Belinha 2014) The shape functions in RPIM are interpolation shape functions, which solves the issue of the essential and natural boundary imposition. Regarding the integration scheme, the RPIM uses a background integration mesh that is nodal independent.

1.3 Osteotomy

Osteotomy is an ancient surgical skill recognized for centuries as a surgical technique that could address deformity thereby improving function or appearance. The surgery involves dividing a bone at a selected site to create an "artificial fracture" (realigning in the correct position), to change the biomechanics of a joint and the corresponding transmitted force through this joint. These procedures must be performed very accurately, not only to create the desired geometries but also to provide biological environments for rapid and effective healing. (Ellis et al. 1999)

Osteotomy is extensively used in a diverse range of problems through the whole skeleton: Facial parts, spine, knee, hip, foot, etc. The Figure 1 summarizes the most common osteotomy procedures in function of the body deformity or disease. In the present work, only the High Tibial Osteotomy (HTO) variant will be analysed.

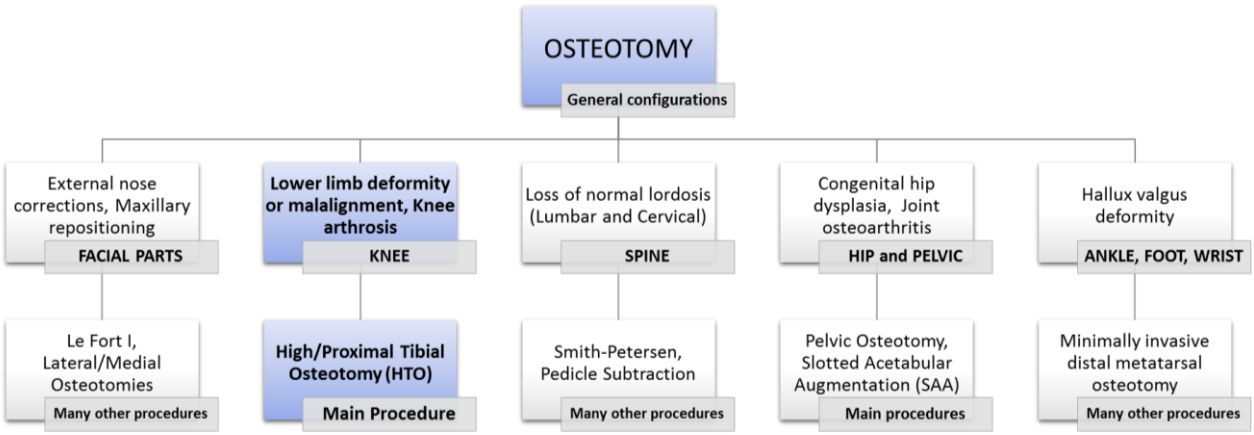

Figure 1 - General osteotomy configurations performed in the human's skeleton for the different diseases/deformities. (Waddell 2012) (Wang 1962)

So, for problems related to the lower limb deformity or knee arthrosis, normally a high tibial osteotomy procedure is required. Nowadays, the most used variant of this procedure is the Opening-Wedge (or Open Wedge) High Tibial Osteotomy (OWHTO), which is the variant here in study, but there are also other variants that will be later described. To maintain the stability of the OWHTO, specialized implants were introduced. A huge variety of fixation implants are utilized in this procedure, and it's almost impossible to find which one has the optimal design in terms of system stability or rigidity ("anchorage"). In the present work, the best reviewed "metal plate" fixation implant obtained from literature was the ContourLock® (from Arthrex®). This implant design and another created designs will be structurally analysed and compared.

1.4 Thesis objectives

The ultimate objective of this thesis, is to encounter an optimal prosthesis design, capable of providing the necessary structural resistance, varying the number of fixation screws and volume of material. The structural analysis is performed with FEM and the meshless method - RPIM, always comparing both numeric results.

In order to achieve the pretended objective, many other will have to be accomplished, such as:

i. Define the state-of-art concerning the high tibial osteotomy and show the clinical point of view of the high tibial osteotomy, exploring their configurations and finding which are the fixation implants normally used;
ii. Understand the principles of both numeric methods that will be used during the structural analysis;

iii. Explore and define the material properties that will be assigned for the structural analysis;
iv. Create a 2D geometric models to obtain different natural boundary conditions for later implementation in the 3D tibial models;
v. Calculate the initial stress distribution of the tibial models, applying those previous boundary conditions, for different deformity situations and compare both FEM and NRPIM results;
vi. Create 3D tibial models with different osteotomy cutting lengths/configurations, comparing the obtained results;
vii. Create 3D tibial models with the chosen fixation implants, for an intraoperative and postoperative analysis (variation of the natural boundary conditions);
viii. Structural analysis with FEM and NRPIM of the final 3D models, comparing both obtained results;
ix. Formulate final conclusions regarding the previous objectives and the choice of the fixation implant.

1.5 Thesis arrangement

The thesis is divided in six major topics: Introduction, High Tibial Osteotomy (HTO), Meshless Methods, Numeric Analysis, Resume and Conclusions and Future recommendations.

In topic 1, **Introduction**, a review on the state of art of the Meshless Methods and on the definition about the general Osteotomy procedure is given. Also, the objectives of the present work are described.

In topic 2, **High Tibial osteotomy (HTO)**, a state-of-art concerning the High Tibial Osteotomy is fully explored. Beginning with a basic presentation of basic anatomic terms used, and then describing the clinical point of view, the different existing variants, the fixation implants used and some other topics.

In topic 3, **Meshless Methods**, the RPIM and the NNRPIM are described and their formulation is presented.

In topic 4, **Numeric Analysis**, the development of how the problem of creating a new fixation implant was addressed, in multiple sections, is presented. It includes the calculation of the forces acting on the tibia for different situations, an initial stress distribution analysis provoked by those forces, explains every model construction, analyses the effect of different lengths of the osteotomy on the tibia and, finally, explains the implant design choice and models created to make the final Intraoperative and Postoperative analysis.

In topic 5, **Resume**, a review of the whole work is given, describing the accomplished objectives.

In topic 6, **Conclusions and Future Recommendations**, the main conclusions regarding the fixation implants and the comparison between the numeric methods results are stated, and some recommendations, for future work improvement, are also given.

2 High Tibial Osteotomy (HTO)

2.1 Anatomic terminology

To better understand lower limb deformities, it is important to firstly review some anatomic literature and concepts that will be used later. In medical terms, the tri-dimensional planes, dividing the human body, are classified as Frontal or Coronal plane, Sagittal plane (Right) and Transverse plane (Top). As anatomic terms of location, the human parts and/or structures are divided in (Figure 2):

- Medial – means towards the Sagittal midline;
- Lateral – means away from the Sagittal midline;
- Superior and inferior – meaning higher and lower;
- Anterior and posterior – referring to the front and the back respectively. (James 2017)

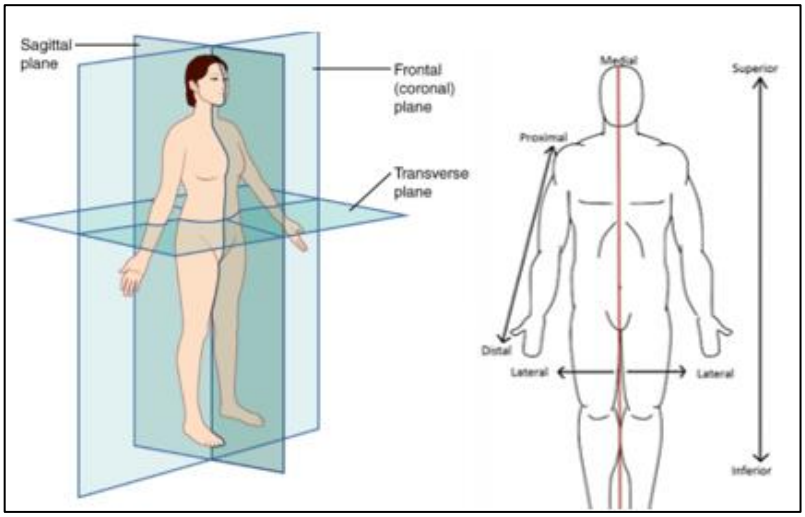

Figure 2 - Anatomical planes and location terms.(James 2017)

Proximal and Distal terms are used in structures that are considered to have a beginning and an end (such as the upper and lower limb). They describe the position of a structure with reference to its origin – proximal means closer to its origin, distal means further away. (James 2017)

Each long bone has a mechanical and an anatomic axis: The tibial mechanical axis, represented in Figure 3, is the line from the center of the proximal joint (knee joint) to the center of the distal joint (ankle joint) and the anatomic axis of a long bone is the *mid-diaphyseal* line (center line) of that bone. The mechanical and anatomic axes, of a tibia, are very close but not the same. The anatomic axis is slightly medial to the mechanical axis (does not pass through the center of the knee joint).

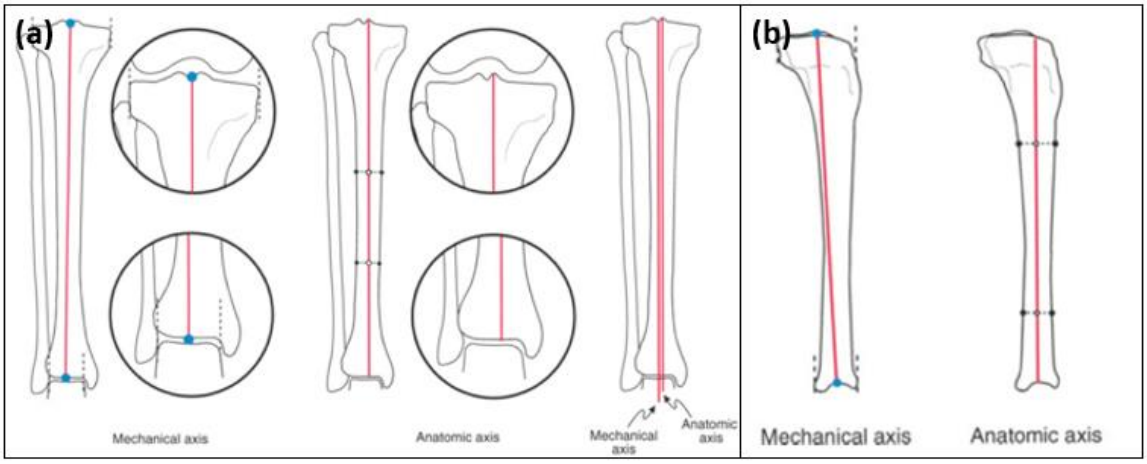

Figure 3 - Mechanical and Anatomic axes of a tibia in the frontal plane (a) and in the sagittal plane (b). (Paley 2005)

The femoral mechanical axis, represented in Figure 4, is not parallel with the anatomical axis like the tibia. Between both, it's defined an Anatomical-Mechanical Axis (AMA) that is approximately equal to 7°.

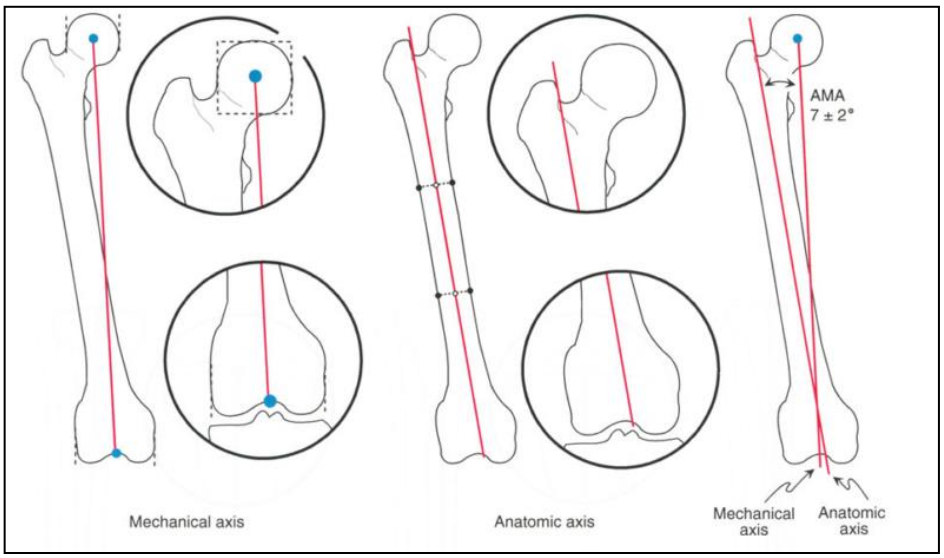

Figure 4 - In the frontal plane, femoral mechanical and anatomic axes are not parallel. The angle between the femoral mechanical and anatomic axes (AMA) is 7±2°. (Paley 2005)

2.2 Methodologies to define a Tibial Deformity

2.2.1 Mikulicz line and the Fujisawa point

Mikulicz line refers to the mechanical axis of the lower limb and is drawn in the long-standing radiograph of the entire leg, from the center of the femur head to the centre of the ankle point. The planned mechanical axis is drawn linking the femur head and the Fujisawa point, which is the point laterally located at 62.5% of the width of the tibial plateau (or plate). In general, if those two lines are not coincident, a tibial osteotomy will be needed to correct the Mikulicz line into the planned mechanical axis. After locating the hinge point or crack tip (tip of the osteotomy cut), the correction angle can be easily obtained. (Monk et al. 2016)

2.2.2 Paley's methodology

A very pertinent and complete work by an Canadian Doctor named *Dror Paley* was made to identify all sorts of lower limb deformities. Here, multiple angles are defined and a range of normal values is given (Figure 5).

Here's the following angles definitions:

- *LPFA* - Lateral Proximal Femoral Angle with a mean value of 90º (normal range 85-95º);
- *mLDFA* - mechanical Lateral Distal Femoral Angle with a mean value of 87.5º (normal range 85-90º);
- *JLCA* – Joint Lateral Convergence Angle with a normal range from 0-2º;
- *MPTA* - Medial Proximal Tibial Angle with a mean value of 87.5º (normal range 85-90º);
- *LDTA* - Lateral Distal Tibial Angle with a mean value of 89º (normal range 86-92º); PPTA - Posterior Proximal Tibial Angle with a value of 80.4º ± 1.6º.

The mLDFA and MPTA is the angle between the femoral and tibial mechanical axis, respectively, with the line linking the condyles contacting points. (Paley 2005)

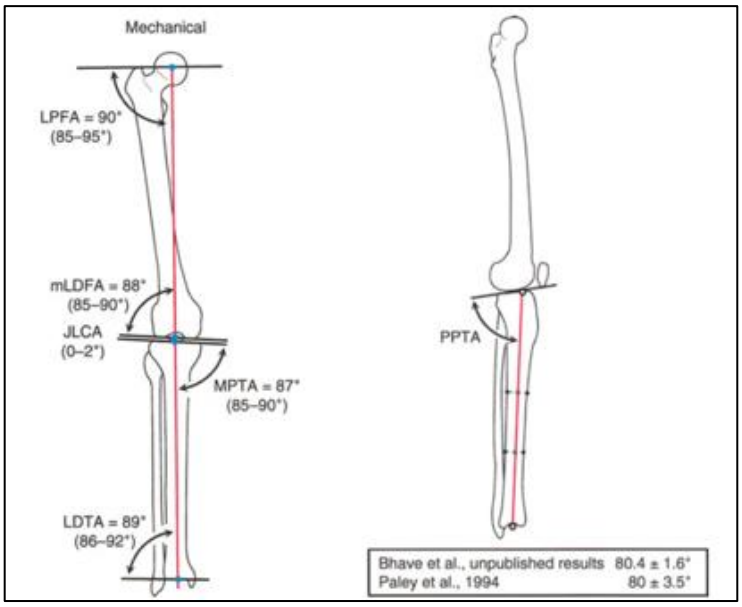

Figure 5 – Frontal and Sagittal plane joint orientation angle nomenclature and normal value' range relative to the mechanical axis. (Paley 2005)

In the frontal plane, the line passing from the center of the femoral head to the center of the ankle plafond is called the mechanical axis of the lower limb. The Mechanical Axis Deviation (MAD) is the perpendicular and medial distance from the mechanical axis line to the center of the knee joint line. The currently normal average MAD is 8±7 mm and its normal representation is exemplified in Figure 6.

"Alignment refers to the collinearity of the hip, knee, and ankle and, by definition, malalignment occurs when the center of the knee does not lie close to this line (loss of collinearity)". (Paley 2005)

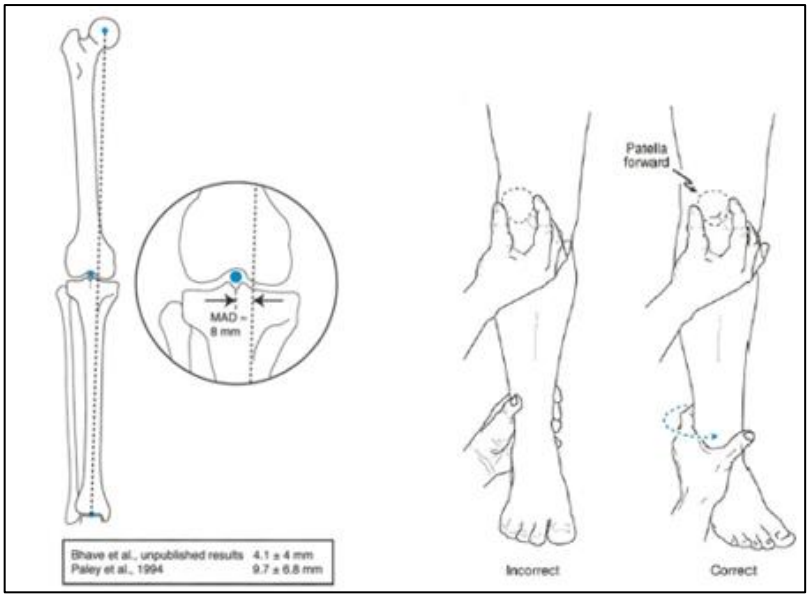

Figure 6 - Representation of the normal Mechanical Axis Deviation. On the right there's the correct (patella is positioned forward with right foot slightly rotated) and incorrect position of the lower limb, for a frontal Radiography. (Paley 2005)

The previous terms are used to identify the source of an abnormal MAD in the Frontal or Coronal plane, which is called the malalignment test. This test processes trough the following steps:

1. Measure the MAD. If the value is outside range, then MAD could be a *varus* (if MAD > 8+7mm=15mm) or a *valgus* (if MAD < 8-7mm=1mm) deformity;
2. Measure the mLDFA. If the mLDFA is outside the normal range (85°-90°), the femur is contributing to the MAD. Less than 85º is a lateral MAD (*valgus*) and greater than 90º is medial MAD (*varus*); If not the process continues knowing that the femur is not the problem;
3. Measure the MPTA. If the MPTA is outside the normal range (85°-90°), the tibia is contributing to the MAD. Less than 85º is an abnormal medial MAD (*varus*) and greater than 90º is an abnormal lateral MAD (*varus*). If not, the process continues knowing that the tibia isn't also the problem (very rare);
4. Measure the lateral and medial JLCA. The normal range is 0-2º. Greater than 2º means that the lateral/medial *ligamento-capsular* laxity or lateral/medial cartilage loss is the source of *varus/valgus* MAD.

The continuation of this methodology leads us to the identification of knee joint subluxation or femoral condylar malalignment as medial or lateral MAD. Other malorientation problems, related to the ankle and hip, can be also identify, however those are irrelevant for the HTO. (Paley 2005)

In Figure 7, there are three examples of medial MAD problems associated with the deformity of the lower limb.

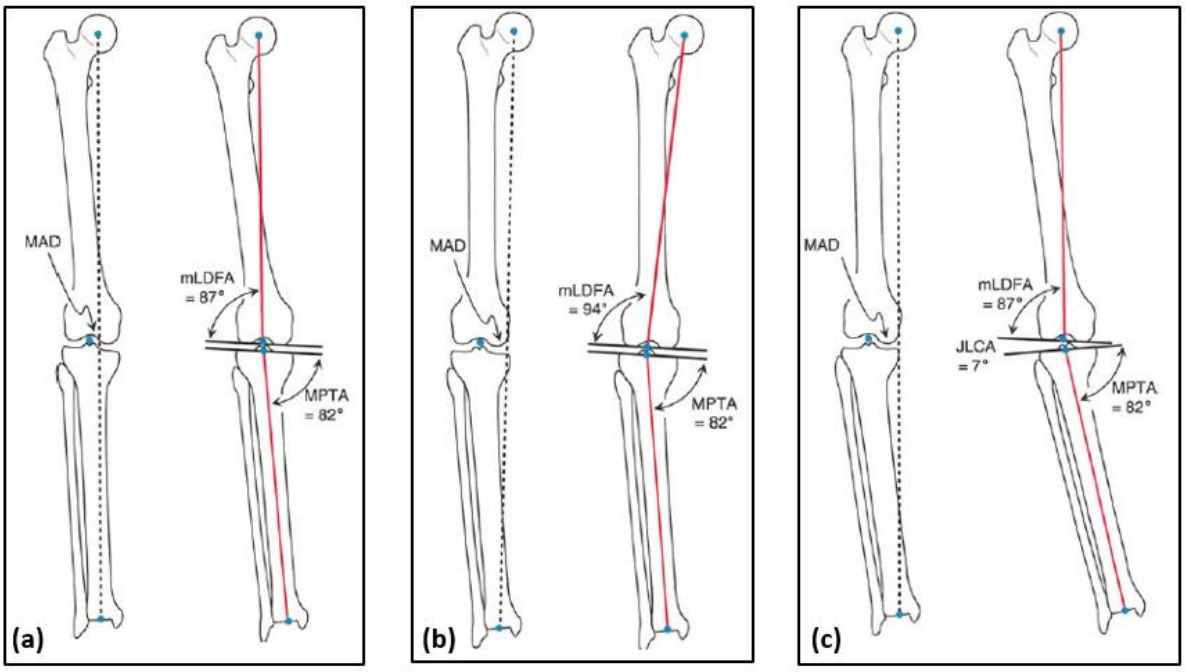

Figure 7 - (a) Medial MAD, mLDFA=87°, MPTA=82°, JLCA=0°: malalignment due to tibial deformity (primary varus). (b) Medial MAD, mLDFA = 94°, MPTA=82°, JLCA=0°: malalignment due to femoral and tibial deformity (primary varus). (c) MediaI MAD, mLDFA=87°, MPTA=82°, JLCA=7°: malalignment due to tibial deformity and lateral collateral ligament laxity (double varus). (Paley 2005)

Only considering the Figure 7-a situation, where only the tibia is the source of malalignment and the only one needing an intervention, the angle of correction is 5°, equal to the difference between the normal mean MPTA (87°) with the current MPTA (82°). For the other situations (Figure 7-b, c), a tibial osteotomy can, sometimes, solve the malalignment of the lower limb.

2.3 Clinical point of view

HTO is a well-established procedure used to correct axial misalignment of the lower limb and knee osteoarthritis (OA). It aims to improve the pain and/or knee functions, through the correction of varus (primary, double and triple) or valgus (rarer) deformities. Concerning the knee OA, the goal of osteotomy is to transfer the weight-bearing loads from the damaged area to an undamaged (relatively unloaded) compartment as well, in order to delay a joint arthroplasty (replacement) in 8-10 years and reduce pain. It is also convenient in some countries for socio-economic reasons. (Benzakour 2010) (Brinkman et al. 2008)

In Figure 8, the two types of deformities are exemplified. In varus deformity the medial compartment load of the tibia and femur is higher than the lateral compartment. In valgus deformity, we have the opposite (higher loads in the lateral compartment). Those deformities increase the risk of medial or lateral progression of knee OA. (Brouwer et al. 2006)

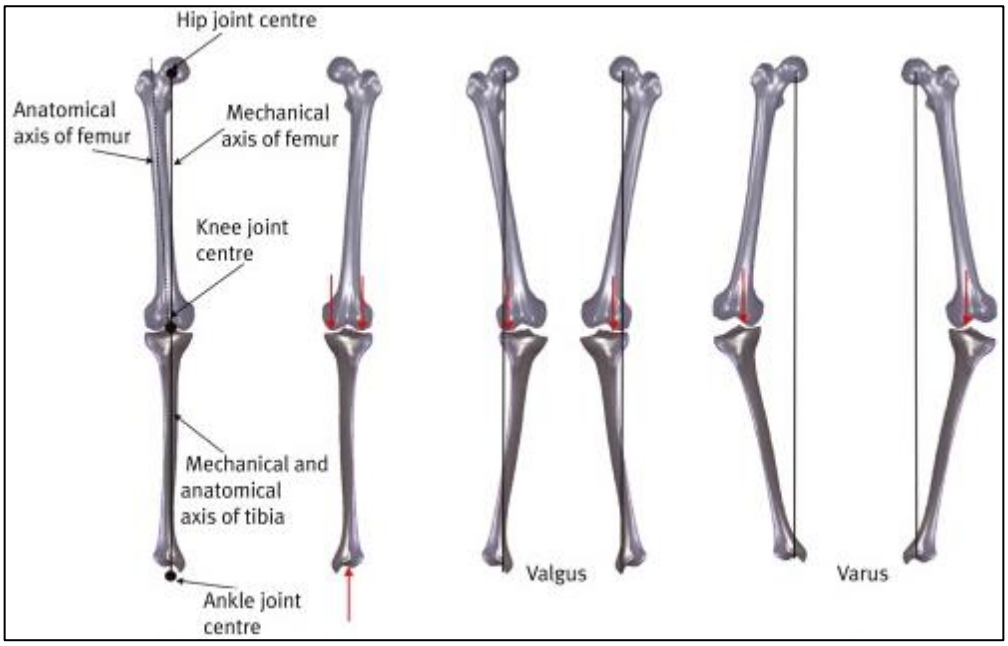

Figure 8 - Normal alignment; Valgus deformity – increases lateral tibiofemoral load; Varus deformity - increases medial tibiofemoral load. (Monk et al. 2016)

2.3.1 Indicated and contraindicated patients

In a simplistic way, the ideal patient for this surgery has between 40 to 60 years old (or even younger) with a body mass index (BMI) below 30, with a high-demanding activity life style but no running or jumping, a varus malalignment below 5º (angle between normal and abnormal mechanical axis of the lower limb) non-smoker and with a normal ligament balance, as is defined in (Brinkman et al. 2008) by *the International Society of Arthroscopy, Knee Surgery and Orthopaedic Sports Medicine*. Also, the patient needs to have some degree of pain tolerance and an almost normal range of motion (10º of extension deficit can be corrected). (Staubli 2011)

Recall that the body mass index is obtained with the expression: $BMI(kg/m^2) = mass(kg)/height^2(m^2)$.

Is contraindicated in patients with signs of tri-compartmental arthrosis, injury in the lateral compartment (meniscus and/or osteochondral injury), deformities greater than 20º (in relation to the mechanical axis), extension deficit, or a range of movement of less than 90º and individuals aged over 60 years with a low level of physical activity (an arthroplasty is better for those individuals). Obesity, smoking and patellofemoral pain are considered relative contraindications. (Ribeiro et al. 2004)

2.3.2 Post-operative management and overall complications

Mobilization starts on day 1 postoperatively, with the patient using forearm crutches with partial weight-bearing activity of 15-20 kg of body weight. Incremental weight-bearing depends on the level of pain. Generally, it is possible for the patient to begin full weight-bearing activity without crutches in the fifth postoperative week, which means that by the end of the sixth postoperative week normal weight-bearing capability should have returned. The range of motion of the knee joint does not need to be restricted, and there is no need for orthoses. In case of complaints, implant removal might be carried out 12-18 months postoperatively. (Staubli 2011)

The major complications that can occur after the high tibial osteotomy are the following: (Ribeiro et al. 2004)

- Fracture of the lateral cortical - usually occurs during the surgical act, decreasing axial resistance (47%) and rotational resistance (54%) of the osteotomy by fracture or perforation of the lateral tibial cortex. When this complication occurs its usually added a lateral fixation (screw or hook) at the apex of the opening wedge, to increase the stability of the osteotomy (Figure 9-left);
- Hypo or hypercorrection - unsatisfactory correction angle. It's very common and very prejudice for the end results of the osteotomy. Navigation system should be used as the main instrument for controlling the degree of correction of the osteotomy. Adds great accuracy and precision, despite longer surgery time;
- Intra-articular fracture - rare complication arising from an incorrectly positioned osteotomy cut;
- Pseudo-arthrosis - occurs in up to 5% of cases. It mainly occurs when no stability is added at the osteotomy site;
- Alteration in tibial slope (Sagittal plane) - causes a loss of knee extension, and also an overload in the anterior/posterior cruciate ligament, which contributes to reduction in anterior/posterior stability (Figure 9-A, B); (Lee and Byun 2012)
- Alteration in patellar height - After closing wedge osteotomy, the segment between the tibial plateau and tibial tuberosity is shortened. After opening wedge osteotomy, this segment is elongated. Relative *patella baja* or patellar ligament shortening can occur;
- Deep vein thrombosis and infection - inherent complications to any surgical procedure. (Ribeiro et al. 2004)

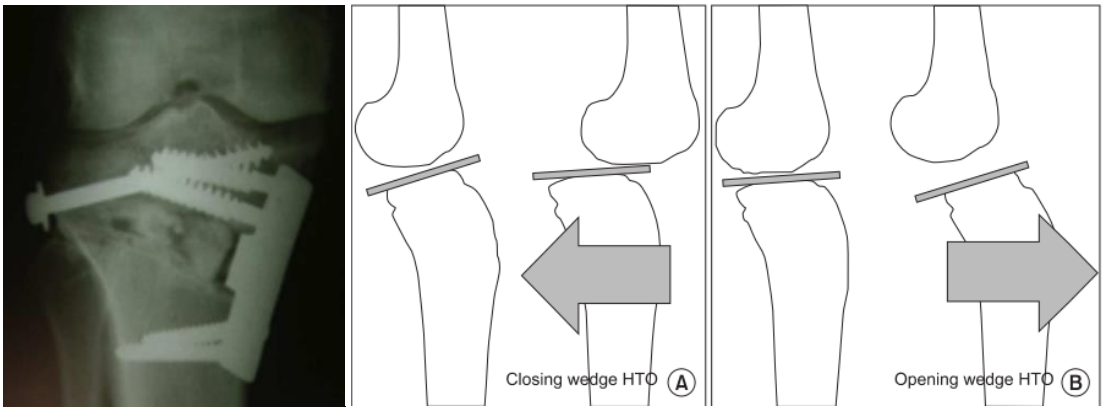

Figure 9 - Screw fixation in fracture of the lateral cortex using Puddu plate. Change of the tibial slope after high tibial osteotomy. (A) Closing wedge high tibial osteotomy (HTO) can cause no change or a decrease in posterior tibial slope, and posterior translation of the tibia can be increased. (B) Opening wedge HTO usually can be caused an increase in posterior tibial slope, and anterior translation of the tibia can be increased.(Lee and Byun 2012)(Ribeiro et al. 2004)

2.4 HTO configurations

As it was previously said, the high tibial osteotomy can be performed in many different cutting shapes and configurations, being the Closing-Wedge (CWHTO) and Opening-Wedge (OWHTO), the two most commonly described and performed variants. (Raja Izaham et al. 2012) In the present work, the OWHTO and the biplanar opening wedge (around the knee) are the variants in study.

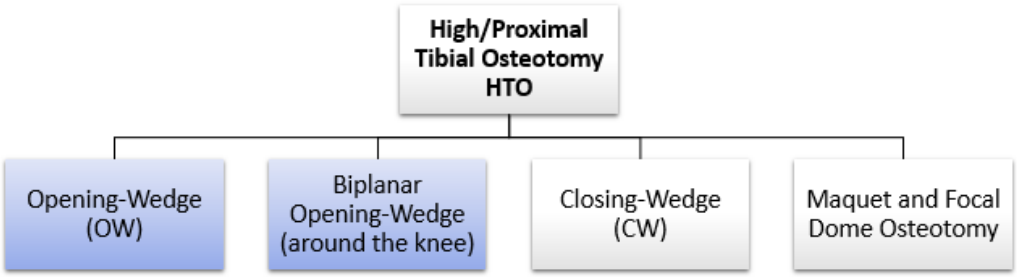

Figure 10 – Most relevant configurations used in HTO. (Paley 2005)

2.4.1 Opening-Wedge

This osteotomy has been increasingly used because is no longer exclusively used for the treatment of unicompartimental medial arthrosis associated with varus deformity (primary varus). (Brinkman et al. 2008) It is also indicated for patient with other deformities, independent of the presence of arthrosis, such as lesions of the cartilage, meniscus, and ligaments (double and triple varus). Patients with varus deformity generally have asymmetrical wear of the knee joint. This is due to the concentration of axial force in the medial compartment, which causes greater impact on the subchondral bone of this compartment, intravenous hypertension, and microfractures of the subchondral bone. Over time, this overload results in the deformity and pain that characterize arthrosis. (Ribeiro et al. 2004)

The possible indication or medical diagnosis of the varus deformation types (primary, double and triple) is represented in Table 1. For the primary varus, the Knee Osteoarthritis of the medial compartment and medial Joint Injures are the main indications for the use of the OWHTO.

Table 1- Indications of each type of varus deformity. (Brinkman et al. 2008)

Type of deformity	Indications
Primary varus	i) Osteoarthritis of the medial compartment of the knee* ii) Joint injuries affecting the medial compartment* iii) Lesions of the medial meniscus and osteochondral injury iv) Ligament instability
Double varus	Varus bone deformity + Injury of the central ligament and/or lateral collateral injury
Triple varus	Varus deformity + Central ligament insufficiency + Failure of the posterolateral corner

It is apparent from most studies that OWHTO is widely preferred, compared to the other variants, owing to the lesser likelihood of developing complications, which may include peroneal nerve injury and disruption of the proximal tibiofibular joint. (Raja Izaham et al. 2012) (Stoffel, Stachowiak, and Kuster 2004) Also, it is an operative approach without muscle detachment, with no need of fibula osteotomy, with a reduced risk of nerve damage and provides subtle corrections by continuous opening the osteotomy. Potential disadvantages may be an increased pressure on the patellofemoral joint by *Patella Baja* (patellar ligament is shortened) and prolonged bone healing process due to the bone gap (compared to the Closing wedge osteotomy). (Hankemeier et al. 2010)

Preoperative planning for HTO involves the use of simple trigonometry to determine the correction angle. In medial open wedge osteotomy, this planned correction angle can be accurately achieved by calculating the height of the open wedge, subsequently delivered during the operation.

First on a long-standing radiograph of the entire leg, the mechanical axis (also known as the Mikulicz line) is drawn (A) (Figure 12-a). Second, the Fujisawa point (B) is indicated and the planned mechanical axis (C) is drawn from the centre of the femoral head through the Fujisawa point to the planned centre of the ankle joint. The hinge point (D), which is the centre of rotation of the osteotomy, is positioned at 5-10 mm medial of the lateral cortex and at the level of the fibula tip. The osteotomy plane is also defined by linking the medial entrance spot at the proximal rim of the *pes anserinus* (conjoined tendons of three muscles) with the center of rotation. It is approximately located at 35-40 mm (Figure 11), bellow the medial knee joint line. (Arthrex®, n.d.)

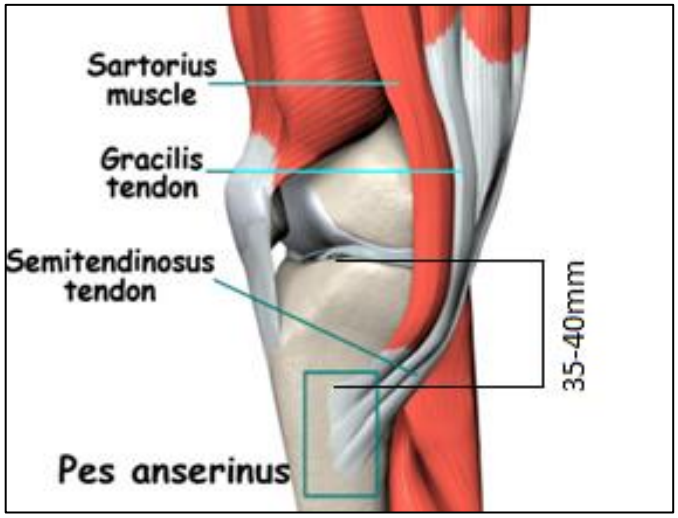

Figure 11- Proximal entrance spot of the osteotomy cutting plane, located at the proximal rim of the *Pes anserinus*.

Two lines connect the planned (E) and current (F) centre of the ankle with the hinge point. The correction angle α is the angle between these two lines (G). Finally, the mediolateral width of the osteotomy (H) is measured from the medial cortex to the hinge point. The height of the open wedge (I) is then calculated as: $I = \tan(\alpha) * H$.

- Consider a patient with a planned correction angle (α) of 8°, and a mediolateral width of the osteotomy (H) of 50 mm. To sufficiently unload the medial compartment, an open wedge with a height of $I = \tan(8) * 50 = 7\ mm$ is therefore required to shift the mechanical axis to the Fujisawa point, (Figure 12-b).

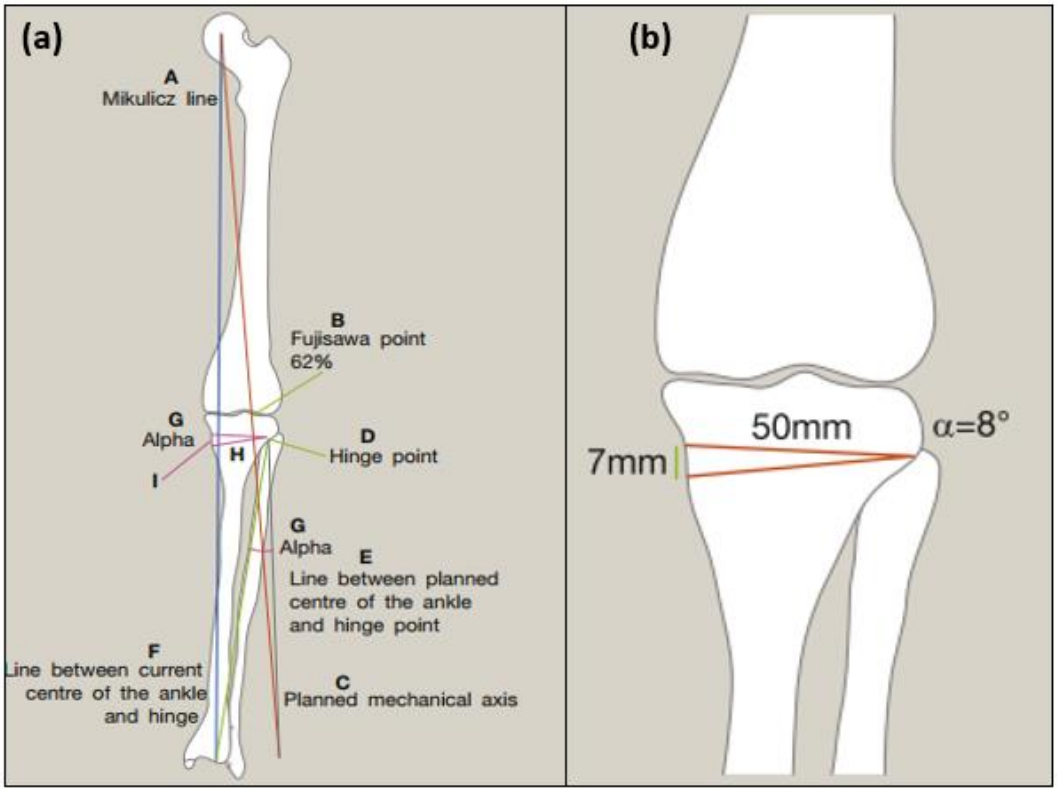

Figure 12 - Planning a medial open wedge high tibia osteotomy in a varus deformity, thereby shifting the mechanical axis from medial to lateral (a). Calculating the required height of the open wedge to shift the biomechanical axis to the Fujisawa point (b). (Monk et al. 2016)

Briefly, this technical surgery starts with the patient placed in the supine position (after incisions), on a radiolucent operating table (Figure 14). Two guide wires are inserted at 35-40 mm below the medial knee joint line and passed obliquely below the lateral articular margin of the tibia towards the tip of the fibular head (hinge point or centre of rotation for the osteotomy) (Figure 13-A). Cortical osteotomy is performed with an oscillating saw inferior to the guide wire (Figure 13-B) and, afterwards, using an osteotome (Figure 13-C). The mobility of the osteotomy site is checked and is opened with a valgus force. When the osteotomy is completed, the medial tibia is opened with a calibrated wedge, to the desired extent angle of correction. (Lee and Byun 2012)

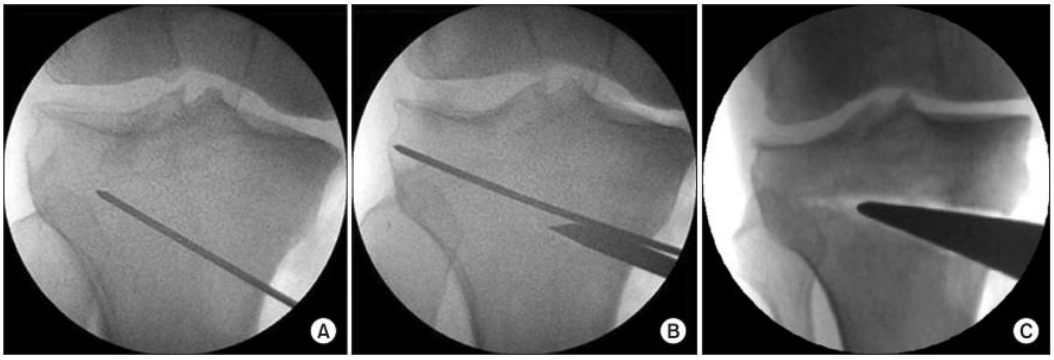

Figure 13 - Opening wedge osteotomy. General steps of varus deformity correction: (A) Insertion of guide wires. (B) Oscillating saw cut. (C) Osteotomy insertion with the desired angle of correction. (Lee and Byun 2012)

The whole procedure is nowadays supported with digital radiography (Arthroscopy or Fluoroscopy) and computer software (*mediCAD* for example) (Hankemeier et al. 2010). A long alignment rod or wire cable is centered over the hip joint and the ankle joint to ensure that it

lies at 62.5% of the width of the tibial plateau (Fujisawa point). Once the desired degree of correction is achieved, internal fixation, usually with a metal plate, is performed.

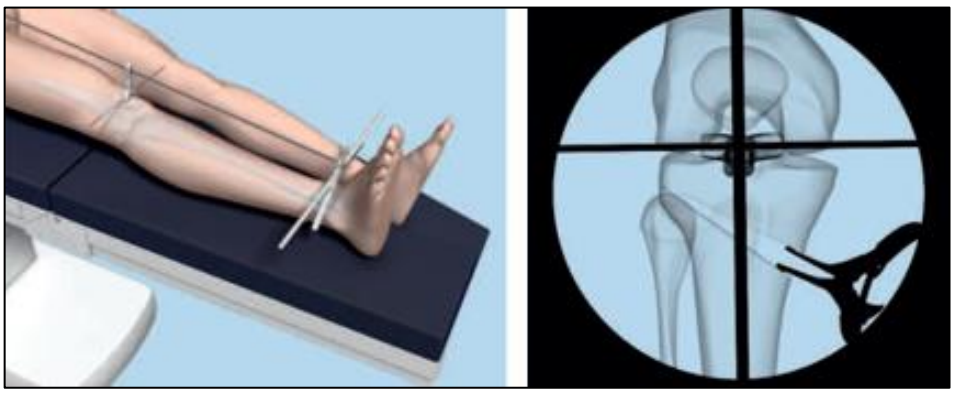

Figure 14 - Alignment rod fixed on the leg to confirm correction of the mechanical axis of the leg, with fluoroscopy support. (DePuySynthesis 2014)

2.4.2 Biplanar opening-wedge (osteotomy around the knee)

A simple modification of the opening-wedge technique has been proposed in the form of a biplanar osteotomy in which a transverse and proximally cut is combined with a second ascending cut behind the tuberosity (PTO) (Figure 15). With this technique more room is left for proximal fixation, because the cut can be performed through the tibial tuberosity, and a buttress is created which provides stability in the sagittal and transverse planes. (Brinkman et al. 2008)

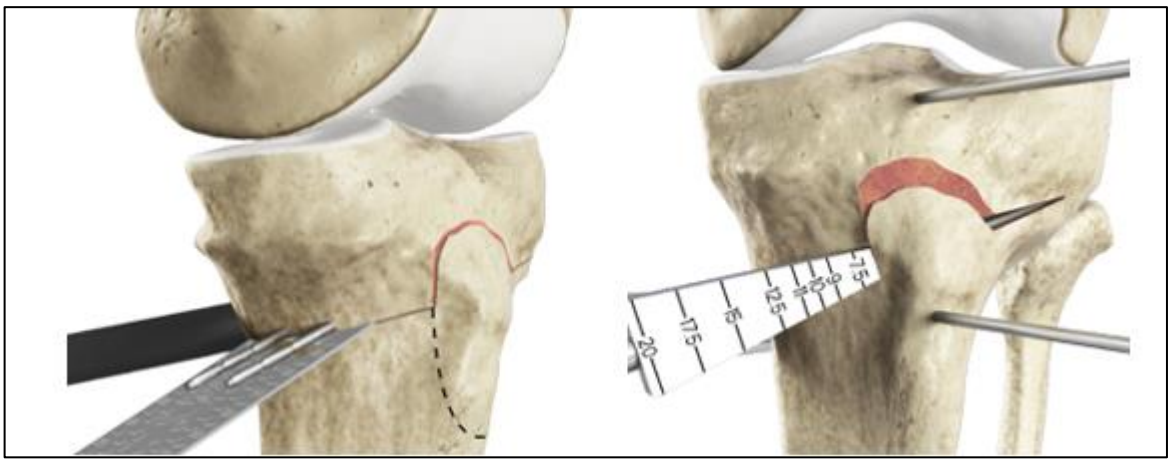

Figure 15 - Creation of a biplanar osteotomy cut (proximal tuberosity) for higher stability and faster healing. (Arthrex®, n.d.)

In large opening-wedge corrections (such as > 8° to 10°) or in cases of pre-existing low patella, the tuberosity osteotomy can be performed distally (DTO) and fixed with one screw to the tibia (Figure 16-b). A study performed by Gaasbeek et al., demonstrated that the patellar height does not change with the DTO, but decreases significantly with the previous proximal tuberosity (Figure 16-a). Distal Tuberosity Opening-Wedge Osteotomy can be a future option to prevent the common problem of lowering the patellar ligament. (Gaasbeek et al. 2004)

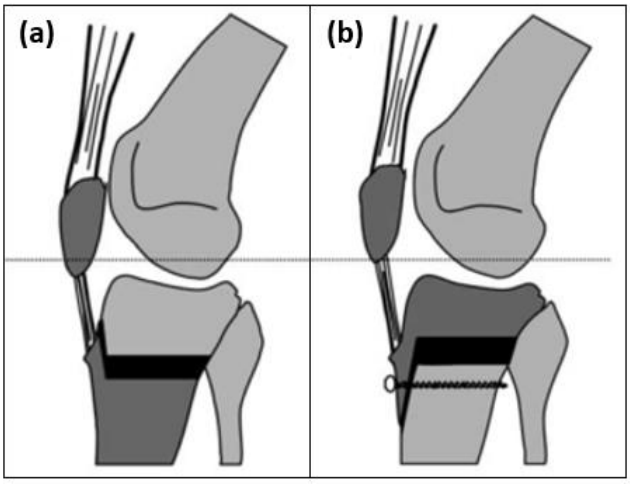

Figure 16 – Lateral view after proximal tuberosity (a) and distal tuberosity (b) opening/wedge osteotomy, with a reference line of the normal patella level. (Gaasbeek et al. 2004)

2.4.3 Closing-Wedge

The closing-wedge osteotomy of the high tibia with removal of a bone wedge is still performed today. The closed-wedge technique, which requires removal of a wedge of bone from the lateral (most common) aspect of the tibia in the metaphyseal region, necessitates cutting along 2 planes. (Staubli 2011) The main advantages of this variant are rapid bone union due to the large contact surface of cancellous bone at the osteotomy site, early weight bearing and rehabilitation, more appropriate for patients with heavy smoking, diabetes, or prolonged use of steroids that have been associated with the risk of non-union. (J. O. Smith, Wilson, and Thomas 2013) Disadvantages are the more extensive lateral approach, increased risk of peroneal nerve affection, difficulty of subtle corrections after bone resection, shortening of the lower limb and difficulty in achieving a predictable degree of correction. (J. O. Smith, Wilson, and Thomas 2013)(Hankemeier et al. 2010)

2.4.4 Maquet and focal dome osteotomy

A special type of HTO is the maquet and focal dome (cylindrical shape) osteotomy, which is a "pendular" osteotomy of the tibia (Figure 17). It is an alternative to the straight cut and it is considered technically challenging. The main advantage of this procedure is the bone-to-bone contact that barely decreases. (Staubli 2011) (Paley 2005)

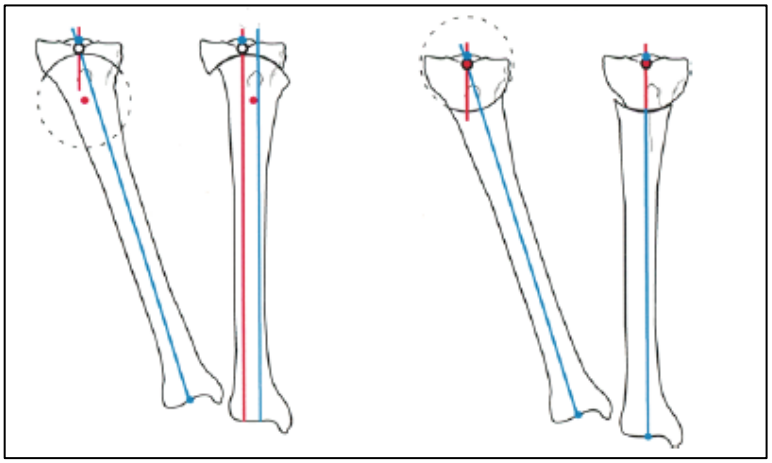

Figure 17 - Maquet (distal concavity) and focal (proximal concavity). (Paley 2005)

2.5 Internal fixation of OWHTO

Actually, there are various types of fixation plates used in OWHTO, such as Tomofix™ , Puddu and ContourLock plates. The iBalance® hardware (from Arthrex®) is a very recent and alternative option to traditional metal plates and screws (Figure 18-b). The iBalance® HTO implants and anchors, all made of non-absorbable polyetheretherketone (PEEK), are intended for permanent implantation and, in some cases, negate the need for a second surgical procedure to remove hardware due to overlying soft tissue irritation. (Arthrex 2013)

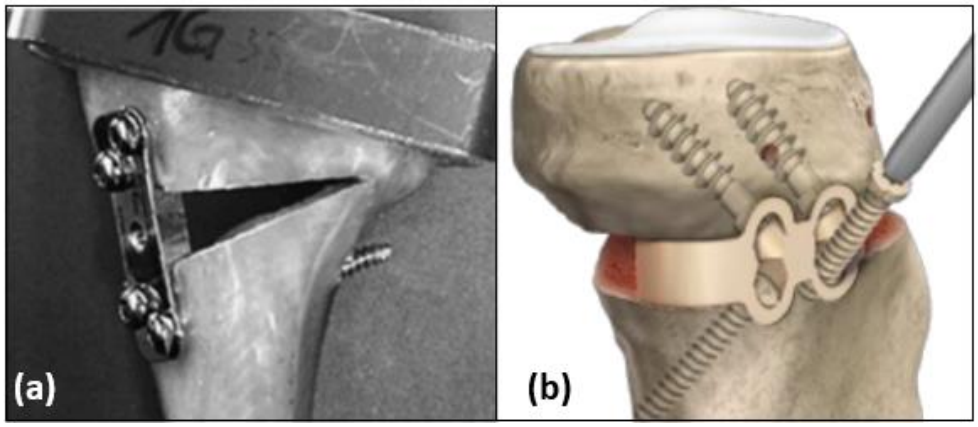

Figure 18 – (a) Puddu plate designed by Giancarlo Puddu, MD, Arthrex Inc., Naples, Florida. (b) iBalance® HTO permanent PEEK implants. (Stoffel, Stachowiak, and Kuster 2004) (Arthrex 2013)

Puddu plate (Figure 18-a) uses the dynamic compression plate (DCP) while the Tomofix™ plate (Figure 19) uses the locking compression plate concept (LCP). (Raja Izaham et al. 2012) The DCP fixation uses a metallic chock interposed in the osteotomy plane which prop the distracted *medial corticalis* and two screws in both proximal and distal plate segments, sufficient to withstand the estimated axial and torsional loads during human gait (figure 15-a). (Stoffel, Stachowiak, and Kuster 2004) The LCP fixation system relies on locked screw heads with all six degrees of freedom restrained. The screws act like bolts, perpendicularly loaded to their main axes and with no friction between the plate and the bone as it is in the Puddu plate. (Stoffel, Stachowiak, and Kuster 2004)(Raja Izaham et al. 2012)

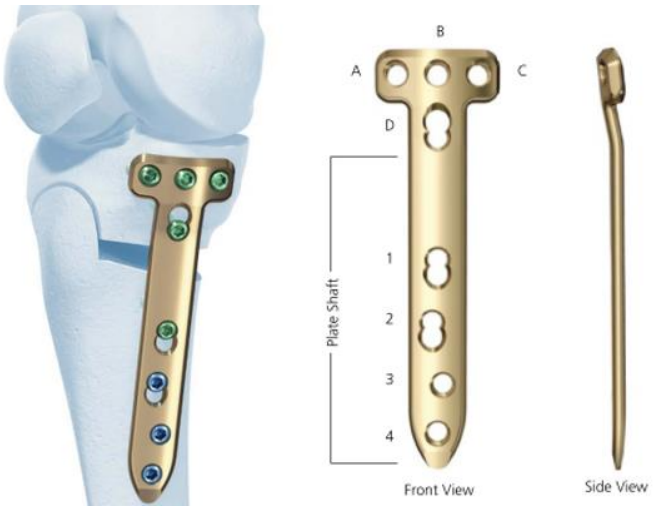

Figure 19 - Medial proximal TomofixTM plate (Mathys Inc., Bettlach, Switzerland) with a fixation through 8 screws: Three Combi-holes (1, 2 and D) provide the flexibility of axial compression and locking capability; Holes 3, 4, A, B and C accept locking screws. (DePuySynthesis 2014)

The ContourLock plate also belongs to Arthrex® and it is a titanium plate with three distinct plate variations, including a straight wedge, sloped wedge and a flat plate with no wedge. It also has a distinct locking bushing system that simplifies the plate and screws insertion process. (Arthrex 2013)

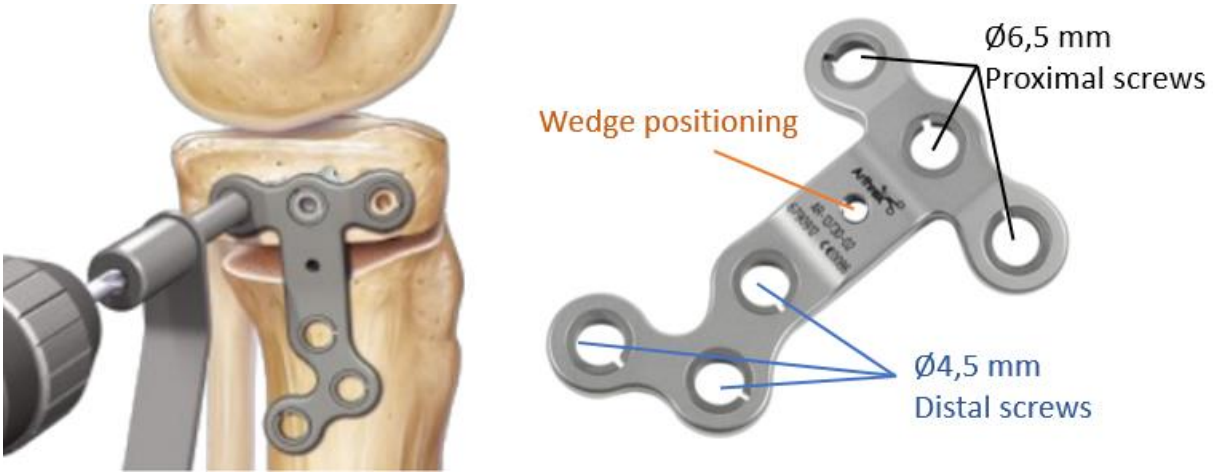

Figure 20 - ContourLock plate from Arthrex®. (Arthrex 2013)

At the proximal or at the top holes are inserted cancellous screws, with a diameter of 6,5 mm, usually form posterior to anterior. The screws will lock into the bushings when fully seated. If a wedge (straight or sloped) is required, its positioning is performed afterwards. Finally, some load is applied on the tibial plateau and the bottom or distal screws, with a diameter of 4,5 mm, are inserted (Figure 20). (Arthrex 2013)

3 Meshless Methods

3.1 Generic procedure of a meshless method

Most of the meshless methods approaches, such as the RPIM and the NNRPIM, respect the following outline: First the problem geometry is studied and the solid domain and contour is established, then the essential and natural boundary conditions are identified. Afterwards, the problem domain and boundary are numerically discretized by a nodal set following a regular or irregular distribution (Figure 21-b, c). Generally, at locations with predictable stress concentrations, such as: domain discontinuities, convex boundaries, crack tips, essential boundaries, natural boundaries etc; it is necessary to present a higher nodal density when compared with other locations in which smooth stress distributions are expected. Since the following discretization parameters influence the method performance, it is essential to choose a correct nodal density of the mesh and the best nodal distribution possible to obtain accurate results and, simultaneously, maintain the computational cost at acceptable levels. (Belinha 2014)

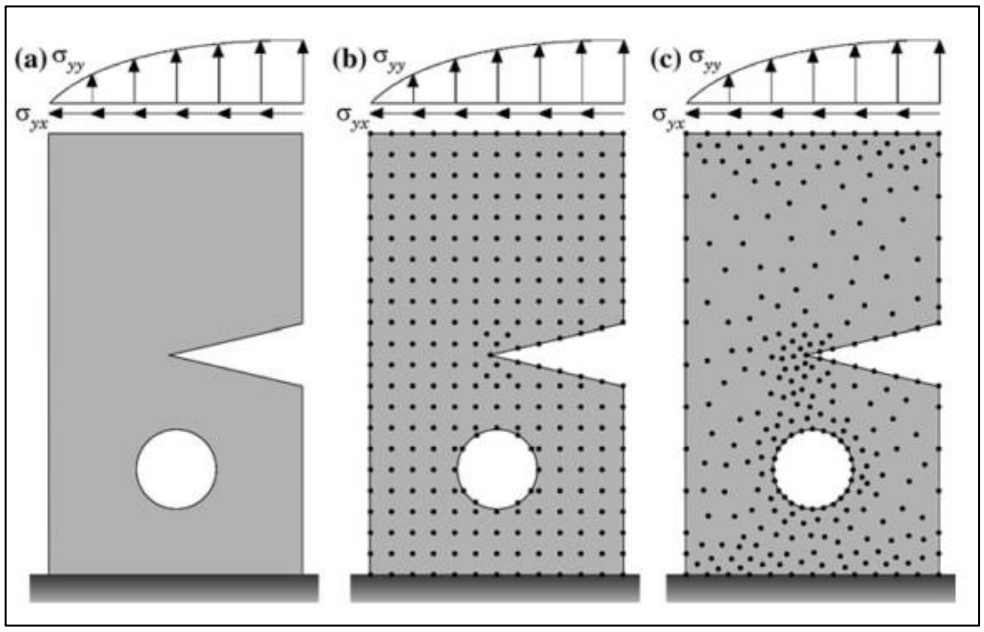

Figure 21 - Nodal discretization domain. (a) Solid domain. (b) Regular discretization. (c) Irregular discretization. (Belinha 2014)

After the nodal discretization, a background integration mesh is constructed, nodal dependent (NNRPIM) or nodal independent (RPIM). Many numerical methods require it in order to numerically integrate the weak form equations governing the physic phenomenon. A nodal independent integration mesh, in general, uses Gauss points, as in the FEM, fitted to the problem domain (Figure 22-a) or not, eliminating the Gauss points that are outside the problem domain (Figure 22-b). Another way to integrate the weak form equations is using the nodal integration by means of the concept of natural neighbours and the Voronoï diagrams. Here, the nodal mesh will also be the integration mesh (Figure 22-c). (Belinha 2014)

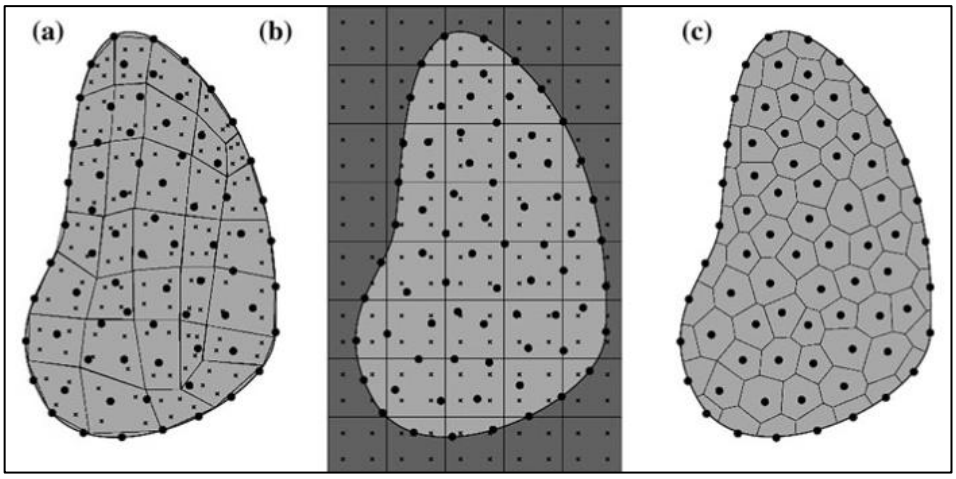

Figure 22 – (a) Fitted Gaussian integration mesh. (b) General Gaussian integration mesh. (c) Voronoï diagram for nodal integration. (Belinha 2014)

With the nodal distribution defined and the integration mesh constructed the nodal connectivity can be imposed. In the FEM, the nodal connectivity is predefined by the used of 'elements', however in the meshless methods there are no elements. Thus, for each interest point $\boldsymbol{x}_I$ of the problem domain concentric areas or volumes (2D or 3D) are defined, and the nodes inside these areas or volumes belong to the influence-domain of interest point $\boldsymbol{x}_I$. (Belinha 2014) In most of the meshless methods, the interest points are the integration points from the background integration mesh. However, there are other methods which consider the nodes as interest points and use the nodal integration scheme. (Belinha 2014)

The shape and size of the influence-domain, which depends on the relative position of the interest point, affects the quality of the results. It is recommended that all influence-domains possess approximately the same number of nodes inside, as so the size of the influence-domain should be dependent on the nodal density around the interest point. (Belinha 2014)

Afterwards the field variables can be obtained with the approximation or interpolation function. Taking for example the displacement field $\boldsymbol{u}$, which components $\boldsymbol{u}(\boldsymbol{x}_I) = (u, v, w)$ are obtained at an interest point $\boldsymbol{x}_I$ within the problem domain and were interpolated using the nodal displacement of the nodes inside the influence-domain of the correspondent interest point, $\boldsymbol{x}_I$. Thus, the following equation can the defined,

$$\boldsymbol{u}(\boldsymbol{x}_I) = \sum_{i=1}^{n} \varphi_i(\boldsymbol{x}_I)\boldsymbol{u}(\boldsymbol{x}_i) \tag{1}$$

where n is the number of nodes inside the influence-domain of the interest point $\boldsymbol{x}_I$, $\boldsymbol{u}(\boldsymbol{x}_i)$ is a vector of the displacement components of each node within the influence-domain and $\varphi_i(\boldsymbol{x}_I)$ is the approximation or interpolation function value of the *ith* node obtained using only the n nodes inside the influence-domain. (Belinha 2014)

Establishing the equation system is the next step. In meshless methods, the discrete equations can be formulated using the approximation or interpolation functions applied to the strong or weak form formulation. In the case of the meshless methods using the weak form of Galerkin, the discrete equations can be obtained applying to the differential equation governing the physic phenomenon the weighted residual method of Galerkin. The produced equations are then arranged in a local nodal matrix form and assembled into a global equation system matrix. Both RPIM and NNRPIM use interpolation functions based on the combination of multiquadric (MQ) radial basis functions (RBF) with polynomial basis functions.

In order to clarify the main differences between the finite element method and a standard meshless method, in Figure 23 it is presented a comparative flow-chart of both numerical approaches. (Belinha 2014)

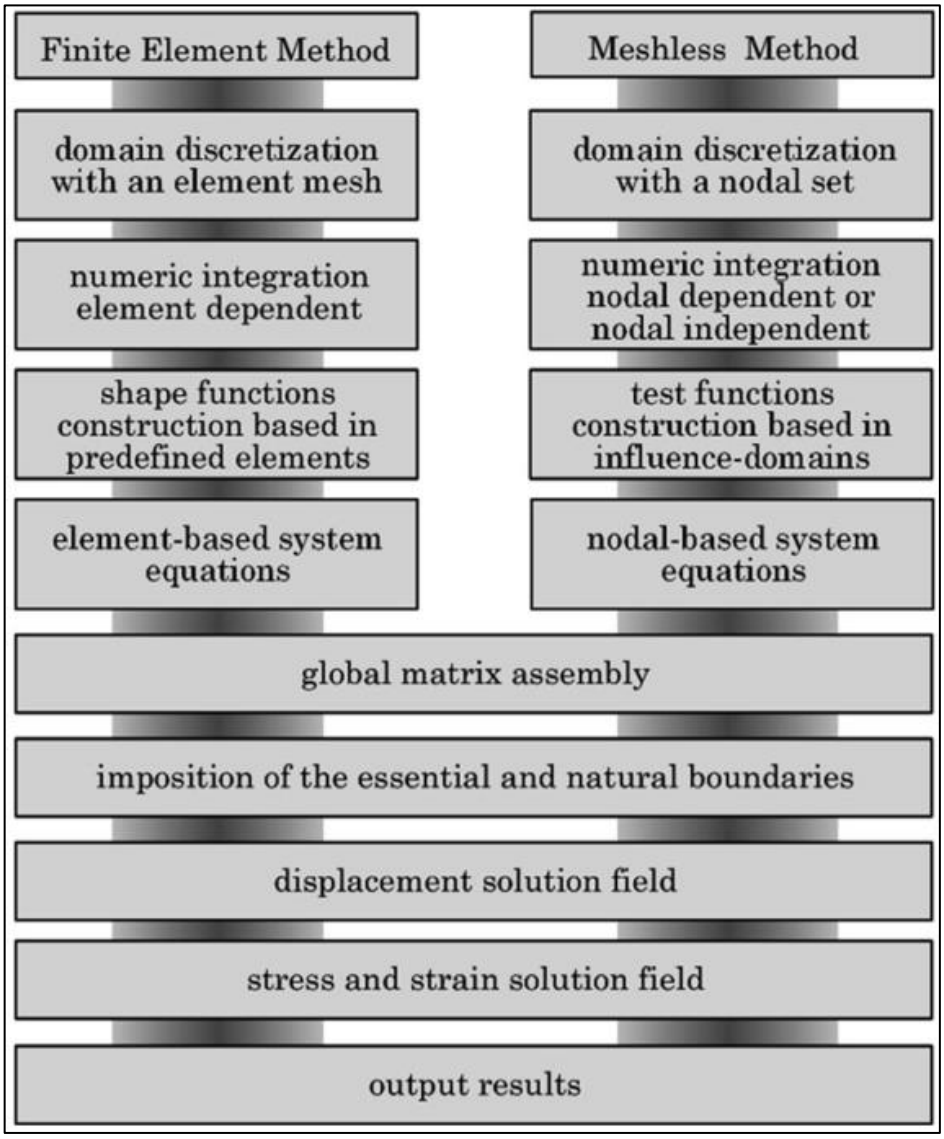

Figure 23 - Comparison between the flow-charts for a finite element method formulation and generic meshless method formulation. (Belinha 2014)

3.2 Radial Point Interpolation Method (RPIM)

3.2.1 Influence-domain and nodal connectivity

In the FEM, the nodal connectivity is assured with the predefined finite element mesh. The nodes belonging to the same element interact directly between each other and with the boundary nodes of neighbour finite elements. In meshless methods, since there is no predefined nodal interdependency, the nodal connectivity needs to be determined after the nodal distribution. This section presents the mostly used methodology to enforce the nodal connectivity in meshless methods and a recently developed flexible technique. (Belinha 2014)

Generally, in meshless methods, the nodal connectivity is obtained by the overlap of the influence-domain of each node. It is important that all the influence-domains in the problem contain approximately the same number of nodes. For a 2D space, two types of fixed size domains are suggested: the rectangular shape influence-domain and the circular shape influence-domain, (Figure 24-a, b).

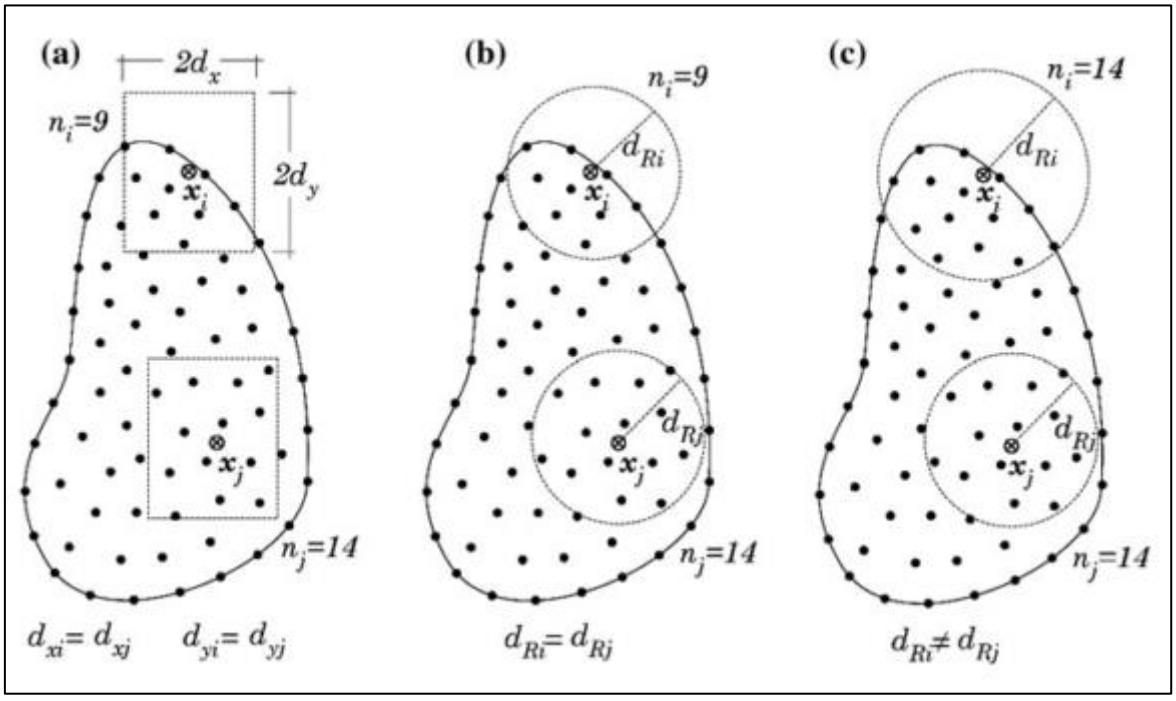

Figure 24 – (a) Fixed rectangular shaped influence-domain. (b) Fixed circular shaped influence-domain. (c) Flexible circular shaped influence-domain. (Belinha 2014)

Notice that using those processes an interest point $\boldsymbol{x}_i$ near the domain boundary possesses less nodes inside its respective influence-domains in comparison with an inner interest point $\boldsymbol{x}_j$, leading to a loss of accuracy in the numeric analysis. Therefore, in order to maintain a constant connectivity along the solid domain, variable influence-domains are a better solution (Figure 24-c). Regardless the used meshless technique, previous works suggest that each influence-domain should possess between 9 to 16 nodes. (Belinha 2014)

3.2.2 Numerical integration

In RPIM, the differential equations of the Galerkin weak form are integrated using the Gauss-Legendre quadrature. Assume the grid-cell present in Figure 25-a. The initial quadrilateral is transform in an isoparametric square, Figure 25-b, then Gauss-Legendre quadrature points are distributed inside the isoparametric square, in Figure 25-b it is used a 2 × 2 quadrature. Using

isoparametric interpolation functions the Cartesian coordinates of the quadrature points are obtained, Figure 25-c.

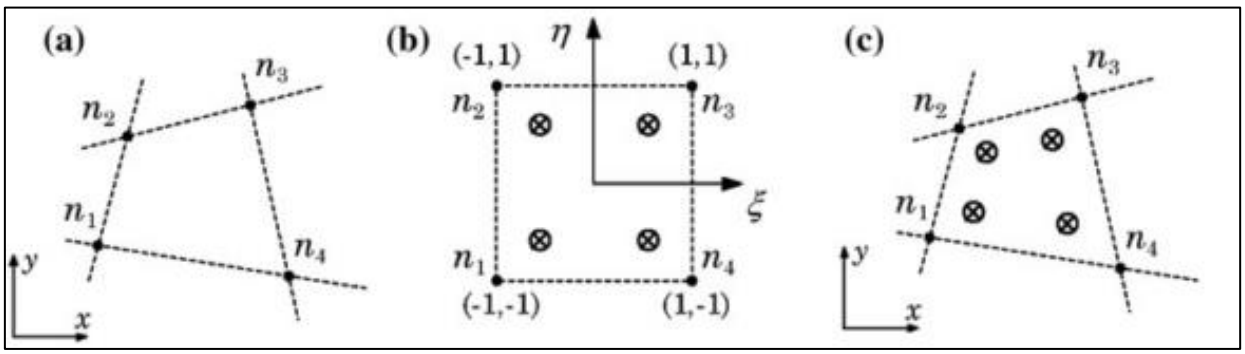

Figure 25 – (a) Initial quadrilateral from the grid-cell. (b) Transformation of the initial quadrilateral into an isoparametric square shape and application of the 2 9 2 quadrature point rule. (c) Return to the initial quadrilateral shape. (Belinha 2014)

The integration weight of the quadrature point is obtained multiplying the isoparametric weight of the quadrature point with the inverse of the Jacobian matrix determinant of the respective grid-cell. To perform the numerical integration, it's considered the function $F(\boldsymbol{x})$ defined in the domain Ω. The global integration can be expressed as a sum,

$$\int_{\Omega} \boldsymbol{F}(\boldsymbol{x})\, d\boldsymbol{\Omega} = \sum_{i=1}^{n_g} w_i \boldsymbol{F}(\boldsymbol{x}_i) \qquad (2)$$

where w_i is the weight of the integration point $\boldsymbol{x}_I$.

3.3 Natural Neighbour Radial Point Interpolation Method (NNRPIM)

3.3.1 Voronoï Diagram Concept and Natural Neighbours

While in the RPIM, the nodal connectivity is imposed by the overlap of influence-domains (fixed or variable blind influence-domains), in the NNRPIM the natural neighbour concept can be used. This approach uses mathematical concepts such as the Voronoï diagrams and the Delaunay triangulation, to determine the nodal connectivity of each node belonging to the global nodal set. Since these influence-domains are determined based on the geometric and spatial relations between the Voronoï cells obtained from the Voronoï diagram of the nodal distribution, the influence-domains are now called 'influence-cells'. (Belinha 2014)

Here, a nodal set $\boldsymbol{N} = \{n_1, n_2, \dots, n_N\}$ is considered, discretizing the space domain $\boldsymbol{\Omega} \subset \mathbb{R}^d$ with $\boldsymbol{X} = \{\boldsymbol{x}_1, \boldsymbol{x}_2, \dots, \boldsymbol{x}_N\} \in \boldsymbol{\Omega}$. The Voronoï diagram of N is the partition of the function space discretized by $\boldsymbol{X}$ in sub-regions V_i, closed and convex. Each sub-region V_i is associated to the node n_i in a way that any point in the interior of V_i is closer to n_i than any other node $n_j \in \mathrm{N} \wedge \mathrm{i} \neq \mathrm{j}$. The set of Voronoï cells $\boldsymbol{V}$ define the Voronoï diagram, $\boldsymbol{V} = \{V_1, V_2, \dots, V_N\}$. The Voronoï cell is defined by,

$$V_i \coloneqq \left\{\boldsymbol{x}_I \in \boldsymbol{\Omega} \subset \mathbb{R}^d : \|\boldsymbol{x}_I - \boldsymbol{x}_i\| < \left\|\boldsymbol{x}_I - \boldsymbol{x}_j\right\|, \ \forall \mathrm{i} \neq \mathrm{j}\right\} \tag{3}$$

being $\boldsymbol{x}_I$ an interest point of the domain and $\|\cdot\|$ the Euclidian metric norm. Thus, the Voronoï cell V_i is the geometric place where all points are closer to n_i than to any other node.

For an easier visualization, a 2D space $\boldsymbol{\Omega} \in \mathbb{R}^2$ is considered and the objective is to determine the Voronoï cell V_0 of the respective node n_0 and the nodes on Figure 26-a are chosen as potential neighbours. In Figure 26-b the node n_4 is selected and the vector is determined.

$$\boldsymbol{u}_{40} = \frac{(\boldsymbol{x}_0 - \boldsymbol{x}_4)}{\|\boldsymbol{x}_0 - \boldsymbol{x}_4\|} \tag{4}$$

Being $\boldsymbol{u}_{40} = \{u_{40}, v_{40}, w_{40}\}$. Using the normal vector $\boldsymbol{u}_{40}$ it is possible to be defined the π_{40}. After the definition of plane π_{40}, all nodes that do not respect the condition bellow are eliminated as natural neighbours of node n_0 (Figure 26-b), and the process is repeated for each one of the initial nodal set (6 in total) and the Voronoï cell V_0 is determined (Figure 26-e).

$$u_{40}x + u_{40}y + u_{40}z \geq (u_{40}x_4 + u_{40}y_4 + u_{40}z_4) \tag{5}$$

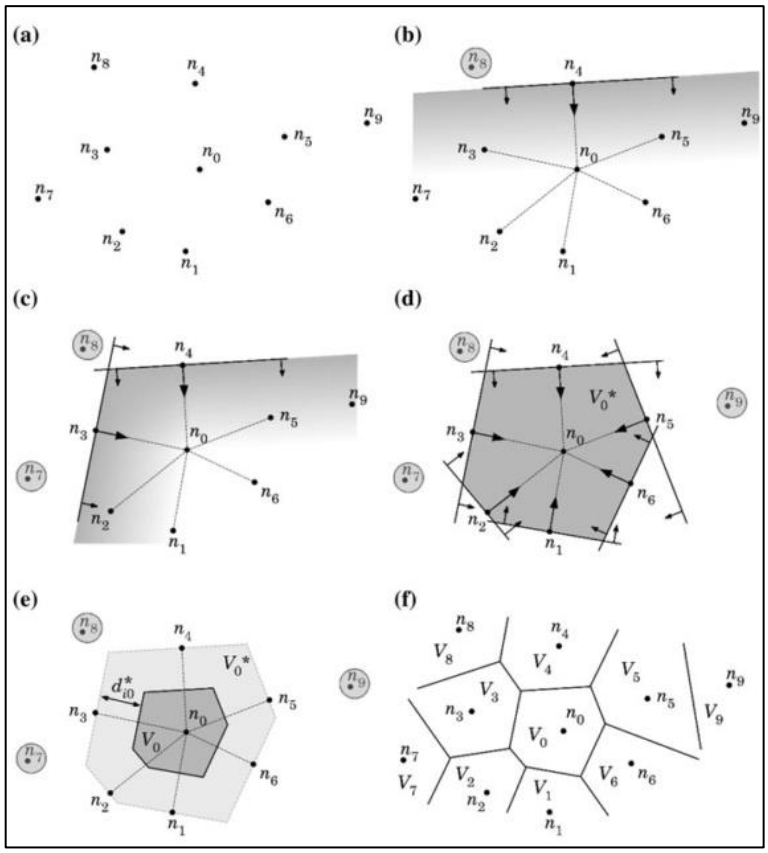

Figure 26 – (a) Initial nodal set of potential neighbour nodes of node n_0. (b) First trial plane. (c) Second trial plane. (d) Final trial cell containing just the natural neighbours of node n_0. (e) Node n_0 Voronoï cell V_0. (f) Voronoï diagram. (Belinha 2014)

3.3.2 Influence-cells and Nodal Connectivity

There are two types of influence-cells, depending on the level of the nodal connectivity. The 'first degree' (Figure 27-a), which are composed by the first natural neighbours of a certain interest point, and the 'second degree' (Figure 27-b), which are composed by the first natural neighbours of a certain interest point and the first neighbours of all the nodes that belong to the first degree influence-cell.

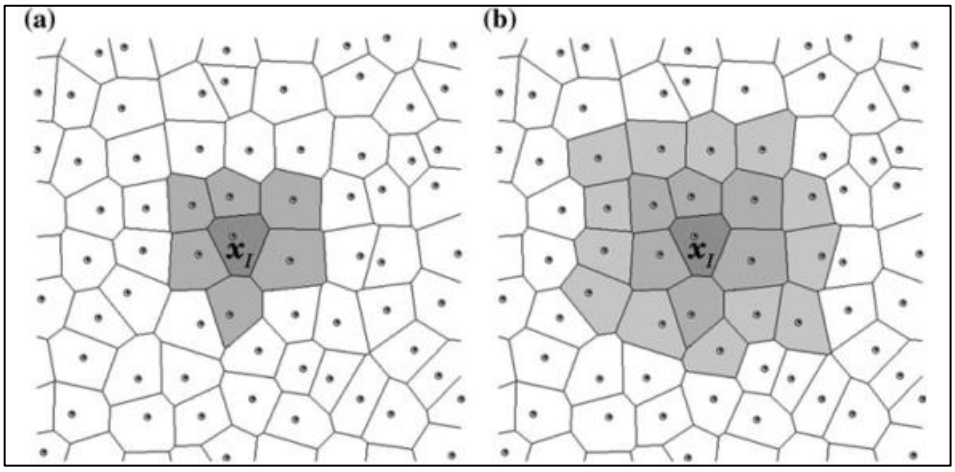

Figure 27 – (a) First degree influence-cell. (b) Second degree influence-cell. (Belinha 2014)

As it is possible to observe the first degree influence-cell is naturally smaller than the second degree influence-cell. Therefore, as expected, the use of second degree influence-cell generally leads to better numerical results. (Belinha 2014)

3.3.3 Nodal Base Integration

The numerical integration in the NNRPIM is performed using another geometric construction, the Delaunay triangulation, which is the geometrical dual of the Voronoï diagram and it is constructed by connecting the nodes of each Voronoï cell with the nodes whose Voronoï cells have common boundaries.

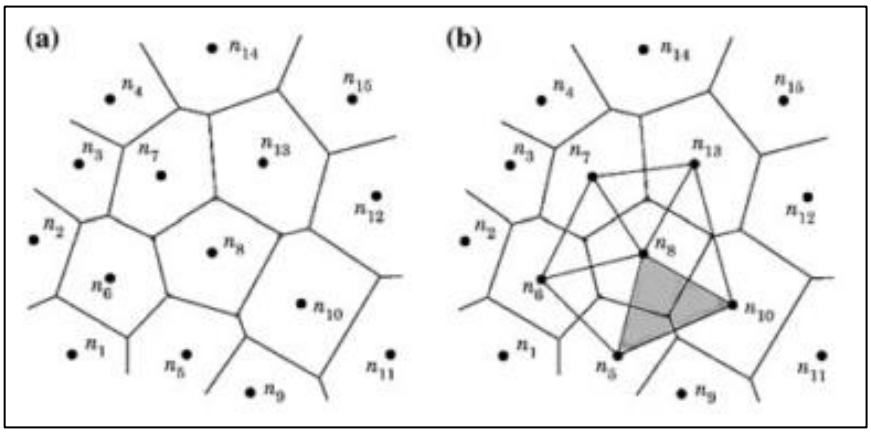

Figure 28 – (a) Initial Voronoï diagram. (b) Delaunay triangulation. (Belinha 2014)

The duality between the Voronoï diagram and the Delaunay triangulation implies that a Delaunay edge exists between two nodes in the plane if and only if their Voronoï cells share a common edge (Figure 28-a,b). In (Belinha 2014) an integration scheme based on the Voronoï diagram and the Delaunay triangulation. The 2D integration scheme is explained below.

In Figure 29, two geometric constructions are used to create quadrilaterals areas that have as vertices the intersection points of the neighbour edges of V_I, the midpoints of the Delaunay edges M_{Ii} and the interest point itself, n_I. Therefore, the Voronoï cells are divided in n quadrilateral sub-cells, S_{Ii}, being n the number of neighbour nodes of the node n_I. Additionally, the sum of the areas occupied by each region has to be equal to the area of the correspondent Voronoï cell.

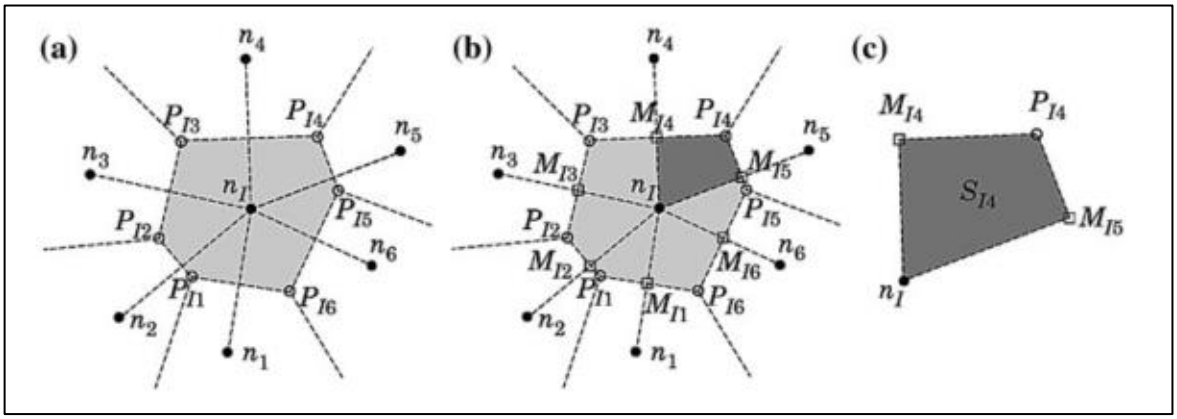

Figure 29 –(a) Voronoï cell and the respective P_{Ii} intersection points. (b) Middle points M_{Ii} and the respective generated quadrilaterals. (c) Quadrilateral $n_I M_{I4} P_{I4} M_{I5}$. (Belinha 2014)

For a regular mesh, Figure 30, the middle points M_{Ii} are coincident with the edge intersection points P_{Ii}. Then, as already mentioned, this leads to the construction of triangles instead of quadrilaterals, as is the case of the irregular mesh.

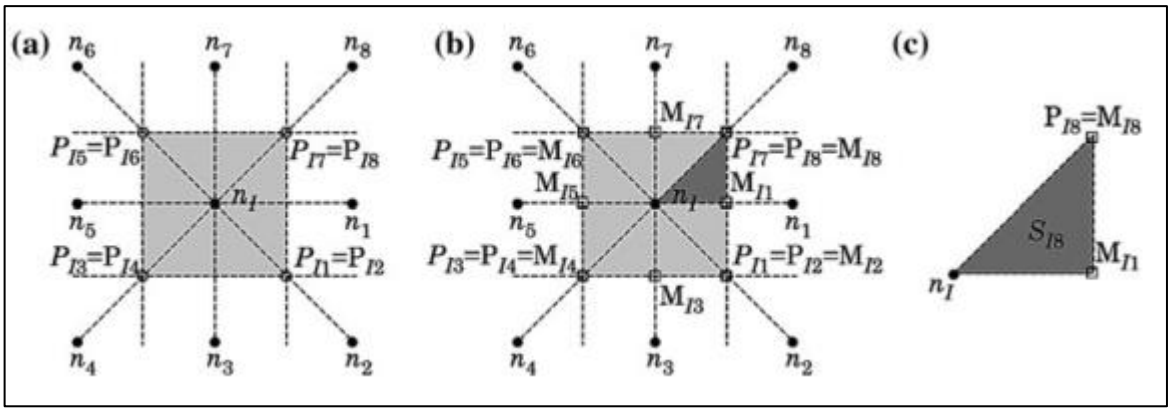

Figure 30 – (a) Voronoï cell and the respective P_{Ii} intersection points. (b) Middle points M_{Ii} and the respective generated triangles. (c) Triangle $n_I P_{I8} M_{I1}$. (Belinha 2014)

The simplest integration scheme (order 0) that can be established, using the sub-cells triangular and quadrilateral shapes, is obtained inserting a single integration point in the barycentre of the sub-cells. Therefore, spatial location of each integration point is determined on each sub-cell, as indicated in Figure 31, being the weight of each integration point the area of the respective sub-cell.

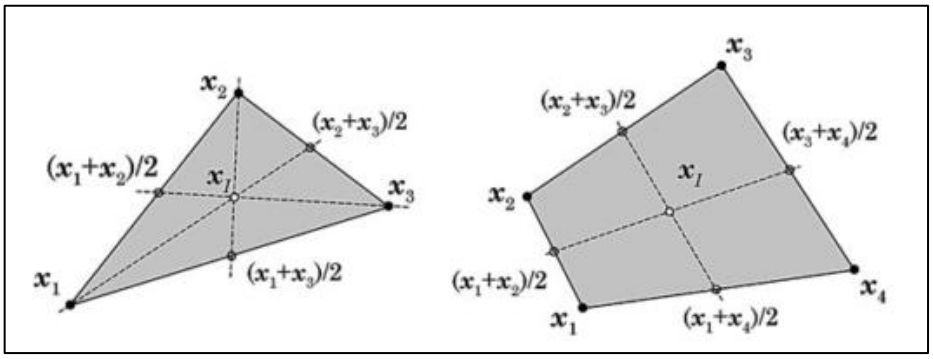

Figure 31 - Triangular shape and quadrilateral shape and the respective integration points $\boldsymbol{x}_I$. (Belinha 2014)

The area of the triangle shape sub-cell is defined by,

$$A_I^{\Delta} = \frac{1}{2}\left|det\begin{bmatrix} x_2 - x_1 & y_2 - y_1 \\ x_3 - x_1 & y_3 - y_1 \end{bmatrix}\right| \tag{6}$$

and for the quadrilateral shape the area is,

$$A_I^{\square} = \frac{1}{2}\left|det\begin{bmatrix} x_2 - x_1 & y_2 - y_1 \\ x_3 - x_1 & y_3 - y_1 \end{bmatrix} + det\begin{bmatrix} x_4 - x_1 & y_4 - y_1 \\ x_3 - x_1 & y_3 - y_1 \end{bmatrix}\right| \tag{7}$$

There are other integration schemes that divide each sub-cell into smaller quadrilateral sub-cells to add more integration points to the original sub-cells (order 1 to k). Yet, adding more integration points increases the computational cost and, at the same time, does not increase significantly the accuracy of the solution.

3.4 Interpolation functions

In terms of Interpolation Functions both the RPIM and the NNRPIM use the same methodology, combining two known methods, the moving least-square approximants (MLS) and the radial point interpolators (RPI).

Assuming a function $u(\boldsymbol{x})$ defined in the domain Ω, which is discretized by a set of n nodes. It is considered that only the nodes inside the influence-cell of the point of interest x_I have effect over $u(\boldsymbol{x}_I)$ and so the value of $u(\boldsymbol{x}_I)$ at the point of interest $\boldsymbol{x}_I$ is calculated by:

$$\begin{aligned} \boldsymbol{u}(\boldsymbol{x}_I) = & \sum_{i=1}^{n} R_i(\boldsymbol{x}_I) a_i(\boldsymbol{x}_I) + \sum_{j=1}^{m} p_j(\boldsymbol{x}_I) b_j(\boldsymbol{x}_I) = \\ = & \ \boldsymbol{R}^T(\boldsymbol{x}_I)\boldsymbol{a}(\boldsymbol{x}_I) + \boldsymbol{p}^T(\boldsymbol{x}_I)\boldsymbol{b}(\boldsymbol{x}_I) \ = \ \{\boldsymbol{R}^T(\boldsymbol{x}_I), \boldsymbol{p}^T(\boldsymbol{x}_I)\} \begin{Bmatrix} \boldsymbol{a} \\ \boldsymbol{b} \end{Bmatrix} \end{aligned} \tag{8}$$

where n is the number of nodes within the influence-domain of x_I, $\boldsymbol{R}(\boldsymbol{x}_I)$ is the Radial Basis Function (RBF), $a_i(\boldsymbol{x}_I)$ and $b_j(\boldsymbol{x}_I)$ are non-constant coefficients of $R_i(\boldsymbol{x}_I)$, and $p_j(\boldsymbol{x}_I)$ is the polynomial basis, respectively, with m being the basis monomial number. The vectors presented in the equation (8) can be represented in vector form by:

$$\boldsymbol{R}(\boldsymbol{x}_I) = \{R_1(\boldsymbol{x}_I), R_2(\boldsymbol{x}_I), \dots \ R_n(\boldsymbol{x}_I)\}^T \tag{9}$$

$$\boldsymbol{p}(\boldsymbol{x}_I) = \{p_1(\boldsymbol{x}_I), p_2(\boldsymbol{x}_I), \dots \ p_n(\boldsymbol{x}_I)\}^T \tag{10}$$

$$\boldsymbol{a}(\boldsymbol{x}_I) = \{a_1(\boldsymbol{x}_I), a_2(\boldsymbol{x}_I), \dots \ a_n(\boldsymbol{x}_I)\}^T \tag{11}$$

$$\boldsymbol{b}(\boldsymbol{x}_I) = \{b_1(\boldsymbol{x}_I), b_2(\boldsymbol{x}_I), \dots \ b_n(\boldsymbol{x}_I)\}^T \tag{12}$$

To guaranty a stable function, the number of monomials of the polynomial basis (m) should be inferior than the number of nodes present in the point of interest influence-cell (n). Although the initial purpose of the addition of a polynomial basis into the radial point interpolator function formulation was to ensure its consistency, it was afterwards found that this addition was not required. These conclusions were reached by not finding a significant change when comparing results from RPI functions with a constant polynomial basis and RPI functions without any polynomial basis function. This allows for equation (8) to be simplified to:

$$\boldsymbol{u}(\boldsymbol{x}_I) = \ \boldsymbol{R}^T(\boldsymbol{x}_I)\boldsymbol{a}(\boldsymbol{x}_I) \tag{13}$$

In 2D problems, the RBFs are dependent of the vector r_{Ii}, the Euclidian distance between the interest point $\boldsymbol{x}_I$ and a node $\boldsymbol{x}_i$ belonging to the influence-domain of $\boldsymbol{x}_I$, and have the following general form:

$$R(r_{Ii}) = \ (r_{Ii}{}^2 + c^2)^p \tag{14}$$

$$r_{Ii} = \sqrt{(x_i - x_I)^2 - (y_i - y_I)^2} \tag{15}$$

where the equation (13) is the multiquadric (MQ) RBFs, and c and p are two parameters with optimal values of 0.0001 and 1.0001 respectively. Those values make RPI possible to have the delta Kronecker property and an easier boundary condition definition.

Consequently, it is possible to write the following equation:

$$\boldsymbol{u}_S = \boldsymbol{R}_{\boldsymbol{Q}}\boldsymbol{a} \tag{16}$$

being $\boldsymbol{u}_S$ the nodal data obtained in each node inside the influence domain:

$$\boldsymbol{u}_S = \{u_1, u_2, \dots, u_n\}^T \tag{17}$$

And matrix $\boldsymbol{R}_{\boldsymbol{Q}}$ $[n \times n]$ contains RBF values between all nodes inside the influence domain, calculated with equation (14):

$$\boldsymbol{R}_{\boldsymbol{Q}} = \begin{bmatrix} R(r_{11}) & R(r_{12}) & \dots & R(r_{1n}) \\ R(r_{21}) & R(r_{22}) & \dots & R(r_{2n}) \\ \vdots & \vdots & \ddots & \vdots \\ R(r_{n1}) & R(r_{n2}) & \dots & R(r_{nn}) \end{bmatrix} \tag{18}$$

Notice that distance is not dependent on the orientation, $R_{ij} = R_{ji}$ and consequently $R(r_{ij}) = R(r_{ji})$ will also be verified. Thus, the previous matrix will be symmetrical. Then, from equation (13) it is obtained: $\boldsymbol{a} = \boldsymbol{R}_Q^{-1}\boldsymbol{u}_s$, which substitution in equation (13) leads to:

$$u(\boldsymbol{x}_I) = \boldsymbol{R}^T(\boldsymbol{x}_I)\boldsymbol{R}_Q^{-1}\boldsymbol{u}_S = \varphi(\boldsymbol{x}_I)\boldsymbol{u}_S \tag{19}$$

Finally, The value of the interpolation function on the point of interest $\varphi(\boldsymbol{x}_I)$, can then be achieved by using:

$$\varphi(\boldsymbol{x}_I) = R^T(\boldsymbol{x}_I)R_Q = \{\varphi_1(\boldsymbol{x}_I), \varphi_2(\boldsymbol{x}_I), \dots, \varphi_n(\boldsymbol{x}_I)\} \tag{20}$$

It is known that this interpolation function (20) satisfies the following equation:

$$\varphi_i(\boldsymbol{x}_j) = \delta_{ij} = \begin{cases} 1\ (i = j) \\ 0\ (i \neq j) \end{cases} i, j = 1, \dots, n \tag{21}$$

which is the delta Kronecker property.

3.5 Three-dimensional Elasticity Theory for the Numerical Analysis

In this section, some solid mechanics fundamentals, used in both Meshless Methods and Finite Element Method, are briefly presented. Afterwards, it is presented the use of the Weak Form and the consequent generated Discrete Equation System in the numeric analysis.

3.5.1 Strain field, Stress Tensor and Equilibrium Equations

Solid Mechanics deals, for a given solid and boundary condition (external forces and displacements constrains), with the relationship between stress and strain and the relationship between strain and displacements. (Belinha 2014) The stresses of a current configuration are defined by the symmetrical Cauchy Tensor $\boldsymbol{\Lambda}$. For a Three-Dimensional problem, its matrix representation is as follows:

$$\boldsymbol{\Lambda} = \begin{bmatrix} \sigma_{xx} & \tau_{xy} & \tau_{xz} \\ \tau_{yx} & \sigma_{yy} & \tau_{yz} \\ \tau_{zx} & \tau_{zy} & \sigma_{zz} \end{bmatrix} \tag{22}$$

In Voigt notation, the stress tensor $\boldsymbol{\Lambda}$ is reduced to the stress vector $\boldsymbol{\sigma}$:

$$\boldsymbol{\sigma} = \begin{Bmatrix} \sigma_{xx} & \sigma_{yy} & \sigma_{zz} & \tau_{xy} & \tau_{yz} & \tau_{zx} \end{Bmatrix}^T \tag{23}$$

and the strain vector $\boldsymbol{\varepsilon}$:

$$\boldsymbol{\varepsilon} = \begin{Bmatrix} \varepsilon_{xx} & \varepsilon_{yy} & \varepsilon_{zz} & \gamma_{xy} & \gamma_{yz} & \gamma_{zx} \end{Bmatrix}^T \tag{24}$$

The stress vector $\boldsymbol{\sigma}$ is calculated by the multiplication of the constitutive matrix, $\boldsymbol{c}$, carrying the material properties, with the strain vector $\boldsymbol{\varepsilon}$:

$$\boldsymbol{\sigma} = \boldsymbol{c}\boldsymbol{\varepsilon} \tag{25}$$

The constitutive matrix is obtained inverting the material compliance matrix $\boldsymbol{s}$, $\boldsymbol{s} = \boldsymbol{c}^{-1}$, which is defined, for a Three-Dimensional anisotropic material as:

$$\boldsymbol{s} = \begin{bmatrix} \frac{1}{E_{xx}} & -\frac{\nu_{yx}}{E_{yy}} & -\frac{\nu_{zx}}{E_{zz}} & 0 & 0 & 0 \\ -\frac{\nu_{yx}}{E_{xx}} & \frac{1}{E_{yy}} & -\frac{\nu_{zy}}{E_{zz}} & 0 & 0 & 0 \\ -\frac{\nu_{xz}}{E_{xx}} & -\frac{\nu_{yz}}{E_{yy}} & \frac{1}{E_{zz}} & 0 & 0 & 0 \\ 0 & 0 & 0 & \frac{1}{G_{xy}} & 0 & 0 \\ 0 & 0 & 0 & 0 & \frac{1}{G_{yz}} & 0 \\ 0 & 0 & 0 & 0 & 0 & \frac{1}{G_{zx}} \end{bmatrix} \tag{26}$$

The elements from (26) are experimentally obtained, where E_{ij} is the Young modulus in direction *i*, ν_{ij} is the Poisson ratio which characterizes the deformation rate in direction *j* when a force is applied in direction *i*, G_{ij} is the shear modulus which characterizes the variation angle between directions *i* and *j*.

The components of the strain vector can be calculated from the displacement field, composed by the displacements along the three directions of the Cartesian coordinate system (i.e., u, v and w, the displacements along the axis x, y and z, respectively):

$$\begin{gathered} \varepsilon_{xx} = \frac{\partial u}{\partial x} \; ; \; \varepsilon_{yy} = \frac{\partial v}{\partial y} \; ; \; \varepsilon_{zz} = \frac{\partial w}{\partial z} \\ \gamma_{xy} = \frac{\partial v}{\partial x} + \frac{\partial u}{\partial y} \; ; \; \gamma_{xz} = \frac{\partial w}{\partial x} + \frac{\partial u}{\partial z} \; ; \; \gamma_{yz} = \frac{\partial w}{\partial y} + \frac{\partial v}{\partial z} \end{gathered} \tag{27}$$

Considering an infinitesimal element, the general Three-Dimensional equilibrium equations are:

$$\begin{gathered} \frac{\partial \sigma_{xx}}{\partial x} + \frac{\partial \tau_{xy}}{\partial y} + \frac{\partial \tau_{xz}}{\partial z} + F_x = 0 \\ \frac{\partial \tau_{yx}}{\partial x} + \frac{\partial \sigma_{yy}}{\partial y} + \frac{\partial \tau_{yz}}{\partial z} + F_y = 0 \\ \frac{\partial \tau_{zx}}{\partial x} + \frac{\partial \tau_{zy}}{\partial y} + \frac{\partial \sigma_{zz}}{\partial z} + F_z = 0 \end{gathered} \tag{28}$$

where F_x, F_y and F_z are the body forces applied on the infinitesimal volume along the directions of the Cartesian axis.

3.5.2 Weak Form of Galerkin

The strong form system equations are the partial differential system equations governing the studied physic phenomenon (i.e. equations (27)). Solving these equations, especially when the object in study and its respective boundary conditions are complex, is extremely difficult. The weak form requires a weaker consistency on the adopted interpolation functions and can produce stable algebraic system equations, obtaining a discretized system of equations, which eventually leads to more accurate results.

The Galerkin weak form is a variational principle based on the energy principle: *"Of all possible displacement configurations satisfying the compatibility conditions, the essential boundary conditions (kinematical and displacement) and the initial and final time conditions, the real solution correspondent configuration is the one which minimizes the Lagrangian functional L"*,

$$L = T - U + W_f \tag{29}$$

Being T the kinetic energy, U is the strain energy and W_f is the work produced by the external forces. Considering a solid with the domain Ω bounded by Γ (Figure 32). The continuous solid

surface on which the external forces $\bar{\boldsymbol{t}}$ are applied is denoted as Γ_t (natural boundary) and the surface where the displacements are constrained is denoted as Γ_u (essential boundary).

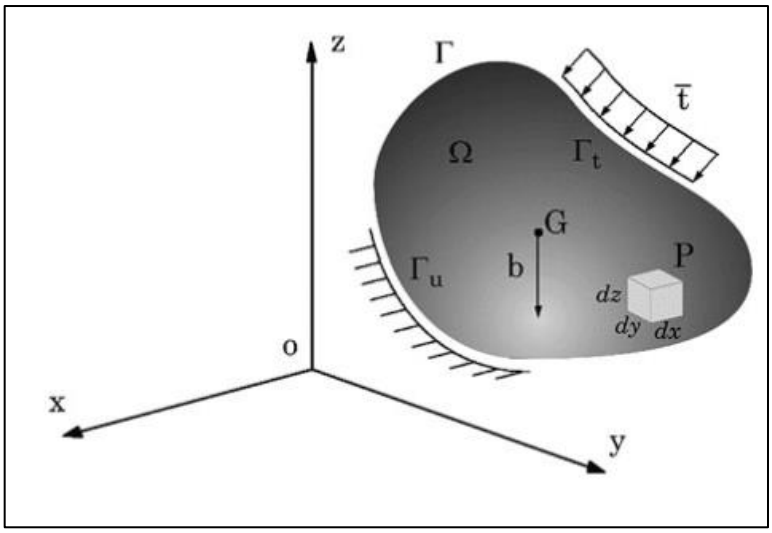

Figure 32 - Continuous solid subject to volume forces and external forces. (Belinha 2014)

The terms of equation (29) are defined as:

$$T = \frac{1}{2}\int_{\Omega} \rho \dot{\boldsymbol{u}}^T \dot{\boldsymbol{u}}\, \mathrm{d}\Omega \tag{30}$$

$$U = \frac{1}{2}\int_{\Omega} \boldsymbol{\varepsilon}^T \boldsymbol{\sigma}\, \mathrm{d}\Omega \tag{31}$$

$$W_f = \int_{\Omega} \boldsymbol{u}^T \boldsymbol{b}\, \mathrm{d}\Omega + \int_{\Gamma_t} \boldsymbol{u}^T \bar{\boldsymbol{t}}\ \mathrm{d}\Gamma \tag{32}$$

where the solid volume is defined by Ω and $\dot{\boldsymbol{u}}$ is the displacement first derivative with respect to time (i.e. the velocity). The solid mass density is defined by ρ. $\boldsymbol{\varepsilon}$ and $\boldsymbol{\sigma}$ are the strain and stress vectors respectively. Finally, $\boldsymbol{u}$ is the displacement and $\boldsymbol{b}$ the body forces.

By substitution the Lagrangian functional L can be rewritten as:

$$L = \frac{1}{2}\int_{\Omega} \rho \dot{\boldsymbol{u}}^T \dot{\boldsymbol{u}}\, \mathrm{d}\Omega - \frac{1}{2}\int_{\Omega} \boldsymbol{\varepsilon}^T \boldsymbol{\sigma}\, \mathrm{d}\Omega + \int_{\Omega} \boldsymbol{u}^T \boldsymbol{b}\, \mathrm{d}\Omega + \int_{\Gamma_t} \boldsymbol{u}^T \bar{\boldsymbol{t}}\ \mathrm{d}\Gamma \tag{33}$$

and then minimized:

$$\delta \int_{t_1}^{t_2} \left[\frac{1}{2}\int_{\Omega} \rho \dot{\boldsymbol{u}}^T \dot{\boldsymbol{u}}\, \mathrm{d}\Omega - \frac{1}{2}\int_{\Omega} \boldsymbol{\varepsilon}^T \boldsymbol{\sigma}\, \mathrm{d}\Omega + \int_{\Omega} \boldsymbol{u}^T \boldsymbol{b}\, \mathrm{d}\Omega + \int_{\Gamma_t} \boldsymbol{u}^T \bar{\boldsymbol{t}}\ \mathrm{d}\,\Gamma \right] \mathrm{d}t = 0 \tag{34}$$

Since this work only concerns to static problems, the kinetic energy T is discarded. Moving now the variation operator δ inside the integral, it is possible to obtain:

$$\int_{t_1}^{t_2} \left[-\frac{1}{2} \int_{\Omega} \delta(\boldsymbol{\varepsilon}^T \boldsymbol{\sigma}) \, \mathrm{d}\Omega + \int_{\Omega} \delta \boldsymbol{u}^T \boldsymbol{b} \, \mathrm{d}\Omega + \int_{\Gamma_t} \delta \boldsymbol{u}^T \bar{\boldsymbol{t}} \, \mathrm{d}\,\Gamma \right] \mathrm{d}t = 0 \tag{35}$$

The first term on equation (35) can be developed. The integrand function in the second integral term can be written as follows:

$$\delta(\boldsymbol{\varepsilon}^T \boldsymbol{\sigma}) = \delta \boldsymbol{\varepsilon}^T \boldsymbol{\sigma} + \boldsymbol{\varepsilon}^T \delta \boldsymbol{\sigma} \tag{36}$$

The terms in equation (36) are scalar, so they can be transposed without affecting the result:

$$\delta \boldsymbol{\varepsilon}^T \boldsymbol{\sigma} = (\delta \boldsymbol{\varepsilon}^T \boldsymbol{\sigma})^{\boldsymbol{T}} = \delta \boldsymbol{\sigma}^T \boldsymbol{\varepsilon} \tag{37}$$

Using the constitutive equation $\boldsymbol{\sigma} = \boldsymbol{c\varepsilon}$ and the symmetric property of the material matrix, $\boldsymbol{c} = \boldsymbol{c}^{\boldsymbol{T}}$, it is possible to write:

$$\delta \boldsymbol{\sigma}^T \boldsymbol{\varepsilon} = \delta(\boldsymbol{c\varepsilon})^T \boldsymbol{\varepsilon} = \delta \boldsymbol{\varepsilon}^T \boldsymbol{c}^T \boldsymbol{\varepsilon} = \delta \boldsymbol{\varepsilon}^T \boldsymbol{c\varepsilon} = \delta \boldsymbol{\varepsilon}^T \boldsymbol{\sigma} \tag{38}$$

and so, equation (38) becomes:

$$\delta(\boldsymbol{\varepsilon}^T \boldsymbol{\sigma}) = 2\delta \boldsymbol{\varepsilon}^T \boldsymbol{\sigma} \tag{39}$$

Modifying the first term of equation (35) with (39), it is obtained:

$$\int_{t_1}^{t_2} \left[-\int_{\Omega} \delta \boldsymbol{\varepsilon}^T \boldsymbol{\sigma} \, \mathrm{d}\Omega + \int_{\Omega} \delta \boldsymbol{u}^T \boldsymbol{b} \, \mathrm{d}\Omega + \int_{\Gamma_t} \delta \boldsymbol{u}^T \bar{\boldsymbol{t}} \, \mathrm{d}\,\Gamma \right] \mathrm{d}t = 0 \tag{40}$$

To satisfy equation (39) for all possible choices of the integrand of the time integration must be null, leading to the following expression:

$$-\int_{\Omega} \delta \boldsymbol{\varepsilon}^T \boldsymbol{\sigma} \, \mathrm{d}\Omega + \int_{\Omega} \delta \boldsymbol{u}^T \boldsymbol{b} \, \mathrm{d}\Omega + \int_{\Gamma_t} \delta \boldsymbol{u}^T \bar{\boldsymbol{t}} \, \mathrm{d}\,\Gamma = 0 \tag{41}$$

Finally, considering the stress-strain relation, $\boldsymbol{\sigma} = \boldsymbol{c\varepsilon}$, and the strain-displacement relation, $\boldsymbol{\varepsilon} = \boldsymbol{Lu}$, being $\boldsymbol{L}$ the differential operator, resulting from equations (27):

$$\boldsymbol{L} = \begin{bmatrix} \frac{\partial}{\partial x} & 0 & 0 \\ 0 & \frac{\partial}{\partial y} & 0 \\ 0 & 0 & \frac{\partial}{\partial z} \\ \frac{\partial}{\partial y} & \frac{\partial}{\partial x} & 0 \\ 0 & \frac{\partial}{\partial z} & \frac{\partial}{\partial y} \\ \frac{\partial}{\partial z} & 0 & \frac{\partial}{\partial x} \end{bmatrix} \tag{42}$$

The equation (40) can be rearranged in the following expression,

$$\int_{\Omega} \delta(\boldsymbol{Lu})^T \boldsymbol{c}(\boldsymbol{Lu})\, \mathrm{d}\Omega - \int_{\Omega} \delta\boldsymbol{u}^T \boldsymbol{b}\, \mathrm{d}\Omega - \int_{\Gamma_t} \delta\boldsymbol{u}^T \bar{\boldsymbol{t}}\, \mathrm{d}\,\Gamma = 0 \tag{43}$$

which is the generic Galerkin Weak form, written in terms of displacement, for a static problem.

3.5.3 Discrete System of Equations

The discrete equations for meshless methods are obtained from the principle of virtual work by using the meshless shape functions. Considering again the equation (1):

$$\boldsymbol{u}(\boldsymbol{x}_I) = \sum_{i=1}^{n} \varphi_i(\boldsymbol{x}_I)\boldsymbol{u}(\boldsymbol{x}_i)$$

Then, by the principle of the virtual work, virtual displacements of nodes within the influence-domain of an interest point $\boldsymbol{x}_I$, cause a virtual displacement in a corresponding integration point, and it can be interpolated considering the interpolation functions already presented in **section 3.4**, as the following test function:

$$\delta u(\boldsymbol{x}_I) = \sum_{i=1}^{n} \boldsymbol{\varphi}_i(\boldsymbol{x}_I)\delta u_i \tag{44}$$

Combining the equation (43) with equation (44):

$$\int_{\Omega}\left(\sum_{i=1}^{n}\varphi_i(\boldsymbol{x}_I)\delta u_i\right)^T \boldsymbol{cL}\left(\sum_{i=1}^{n}\varphi_i(\boldsymbol{x}_I)u_i\right)\mathrm{d}\Omega - \int_{\Omega}\left(\sum_{i=1}^{n}\varphi_i(\boldsymbol{x}_I)\delta u_i\right)^T \boldsymbol{b}\,\mathrm{d}\Omega - \int_{\Gamma_t}\left(\sum_{i=1}^{n}\varphi_i(\boldsymbol{x}_I)\delta u_i\right)^T \bar{\boldsymbol{t}}\;\mathrm{d}\,\Gamma = 0 \tag{45}$$

The previous equation can be rewritten as a matrix equation, eliminating the summations. To do that, the general matrix of the interpolations functions for a 3D problem is considered:

$$\boldsymbol{\varphi}(\boldsymbol{x}) = \begin{bmatrix} \varphi_1(\boldsymbol{x}) & 0 & 0 & \varphi_2(\boldsymbol{x}) & 0 & 0 & \dots & \varphi_n(\boldsymbol{x}) & 0 & 0 \\ 0 & \varphi_1(\boldsymbol{x}) & 0 & 0 & \varphi_2(\boldsymbol{x}) & 0 & \dots & 0 & \varphi_n(\boldsymbol{x}) & 0 \\ 0 & 0 & \varphi_1(\boldsymbol{x}) & 0 & 0 & \varphi_2(\boldsymbol{x}) & \dots & 0 & 0 & \varphi_n(\boldsymbol{x}) \end{bmatrix} \tag{46}$$

The equation (45) becomes the following expression:

$$\delta\boldsymbol{u}^T\int_{\Omega}[(\varphi(\boldsymbol{x}_I))^T\boldsymbol{L}^T]\boldsymbol{c}[\boldsymbol{L}\varphi(\boldsymbol{x}_I)]\,\mathrm{d}\Omega\boldsymbol{u} - \delta\boldsymbol{u}^T\int_{\Omega}(\varphi_i(\boldsymbol{x}_I))^T\boldsymbol{b}\,\mathrm{d}\Omega - \delta\boldsymbol{u}^T\int_{\Gamma_t}(\varphi_i(\boldsymbol{x}_I))^T\bar{\boldsymbol{t}}\;\mathrm{d}\Gamma = 0 \tag{47}$$

where $\boldsymbol{u}$ is the vector of the nodal displacements of the nodes inside the influence-domain, and is given by:

$$\boldsymbol{u} = \{u_1, v_1, w_1, u_2, v_2, w_2, \dots, u_n, v_n, w_n\}^{\boldsymbol{T}} \tag{48}$$

A deformation matrix is defined as the multiplication of matrixes $\boldsymbol{L}$ (41) and $\boldsymbol{\varphi}(\boldsymbol{x_I})$:

$$\boldsymbol{B}(\boldsymbol{x}_I) = \boldsymbol{L}\varphi(\boldsymbol{x}_I) = \begin{bmatrix} \frac{\partial\varphi_i(\boldsymbol{x}_I)}{\partial x} & 0 & 0 & \frac{\partial\varphi_i(\boldsymbol{x}_I)}{\partial y} & 0 & \frac{\partial\varphi_i(\boldsymbol{x}_I)}{\partial z} \\ 0 & \frac{\partial\varphi_i(\boldsymbol{x}_I)}{\partial y} & 0 & \frac{\partial\varphi_i(\boldsymbol{x}_I)}{\partial x} & \frac{\partial\varphi_i(\boldsymbol{x}_I)}{\partial z} & 0 \\ 0 & 0 & \frac{\partial\varphi_i(\boldsymbol{x}_I)}{\partial z} & 0 & \frac{\partial\varphi_i(\boldsymbol{x}_I)}{\partial y} & \frac{\partial\varphi_i(\boldsymbol{x}_I)}{\partial x} \end{bmatrix}_i^T \tag{49}$$

for $i = 1,2,\dots,n$, which is the order of the nodes inside the influence-domain.

The last step is to rearrange the equation (46), replacing $\boldsymbol{L\varphi}(\boldsymbol{x_I})$ by $\boldsymbol{B}(\boldsymbol{x_I})$:

$$\delta\boldsymbol{u}^T\left[\int_{\Omega}\boldsymbol{B}(\boldsymbol{x}_I)^T\boldsymbol{c}\boldsymbol{B}(\boldsymbol{x}_I)\,\mathrm{d}\Omega\boldsymbol{u} - \int_{\Omega}(\varphi_i(\boldsymbol{x}_I))^T\boldsymbol{b}\,\mathrm{d}\Omega - \int_{\Gamma_t}(\varphi_i(\boldsymbol{x}_I))^T\bar{\boldsymbol{t}}\;\mathrm{d}\Gamma\right] = 0 \tag{50}$$

Finally resulting into:

$$\underbrace{\int_{\Omega} \boldsymbol{B}(\boldsymbol{x_I})^T \boldsymbol{c}\boldsymbol{B}(\boldsymbol{x_I}) \mathrm{d}\Omega}_{\boldsymbol{K_I}} \boldsymbol{u} - \underbrace{\int_{\Omega} (\varphi_i(\boldsymbol{x}_I))^T \boldsymbol{b}\, \mathrm{d}\Omega}_{\boldsymbol{f_I^b}} - \underbrace{\int_{\Gamma_t} (\varphi_i(\boldsymbol{x}_I))^T \bar{\boldsymbol{t}}\ \mathrm{d}\Gamma}_{\boldsymbol{f_I^t}} = 0 \tag{51}$$

that represents the local static equilibrium at the influence-domain of the interest point $\boldsymbol{x}_I$. The first term of the equation is called the local stiffness matrix $\boldsymbol{K}_I$, and the sum of the other two terms is the local vector of the global force**,** $\boldsymbol{f}_I$.The assemblage of the local stiffness matrices and local force vectors lead to the following equation system: $\boldsymbol{K}\boldsymbol{u} = \boldsymbol{f}$.

3.5.4 Essential Boundary Conditions Imposition

If the shape functions of the meshless method possess the Kronecker delta property, then the boundary conditions can be imposed directly as in the FEM. The continuum analysis involves two types of boundary conditions, the essential boundary conditions (displacement related) and the natural boundary conditions (force related). As already mentioned, equation (51) can be rewritten into the following matrixial form:

$$\boldsymbol{K}\boldsymbol{u} = \boldsymbol{f} \tag{52}$$

This equation can be rewritten as:

$$\begin{bmatrix} \boldsymbol{K}_{cc} & \boldsymbol{K}_{cd} \\ \boldsymbol{K}_{dc} & \boldsymbol{K}_{dd} \end{bmatrix} \begin{bmatrix} \boldsymbol{u}_c \\ \boldsymbol{u}_d \end{bmatrix} = \begin{bmatrix} \boldsymbol{f}_c \\ \boldsymbol{f}_d \end{bmatrix} \tag{53}$$

where $\boldsymbol{u}_c$ are the unknown displacements and $\boldsymbol{u}_d$ the known or prescribed displacements. The vectors $\boldsymbol{f}_c$ and $\boldsymbol{f}_d$ are the known applied loads (external and body forces) and to the unknown reactions from the imposed displacement constrains. The previous equation assumes that the essential boundary conditions are axial aligned with the prescribed displacements. If the contrary occurs then a transformation of the discrete equilibrium equations to the corresponding global axis is required (Figure 33). (Belinha 2014)

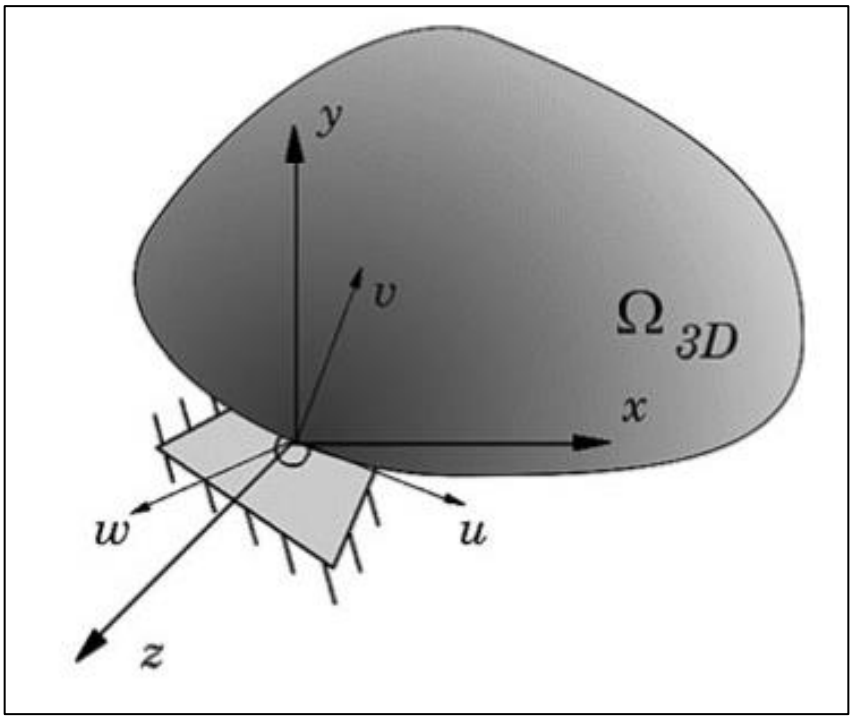

Figure 33 - Essential boundary condition nonaligned with the global axis, in a Three-Dimensional problem. (Belinha 2014)

The transformation matrix $\boldsymbol{T}$ is defined by:

$$\boldsymbol{T} = \begin{bmatrix} u_x & v_x & w_x \\ u_y & v_y & w_y \\ u_z & v_z & w_z \end{bmatrix} \tag{54}$$

Thus, the vector $\boldsymbol{u}$, the matrix $\boldsymbol{K}$ and the vector $\boldsymbol{f}$ turn into the following equations, respectively:

$$\boldsymbol{u} = \boldsymbol{T}\bar{\boldsymbol{u}} \tag{55}$$

$$\bar{\boldsymbol{K}} = \boldsymbol{T}^{\boldsymbol{T}}\boldsymbol{K}\boldsymbol{T} \tag{56}$$

$$\bar{\boldsymbol{f}} = \boldsymbol{f}^{\boldsymbol{T}}\boldsymbol{K}\boldsymbol{f} \tag{57}$$

4 Numeric Analysis

4.1 Problem formulation

The Figure 34 illustrates how, in the present work, the problem of designing a new metal implant is going to be addressed, step by step:

1. A Finite Element study will be conducted to find the forces that normally act on top of the tibial plateau for three different situations – Normal, Varus and Valgus (Geometric model);
2. The Models will be constructed from the anonymized DICOM's from MIMICS® ending up in the academic program used named FEMAS;
3. An Initial stress distribution will be obtained, for each situation, with different bone material distributions – One model considering the bone as an homogeneous material and another model, considering three materials for the bone (cortical bone, dense trabecular bone and sparse trabecular bone);
4. The OWHTO, with a biplanar cut, will be analysed for different lengths (60, 65 and 70 mm) and with the Circular Hinge option, only considering the homogeneous material model;
5. Two fixation implants will be designed and implemented in the Osteotomized tibial model, for an intraoperative analysis. There will be a total of four final models in this structural analysis;
6. The same models structurally analysed for the intraoperative situation are going to be analysed again for a postoperative situation. For steps 5 and 6, only the homogeneous material model is considered.

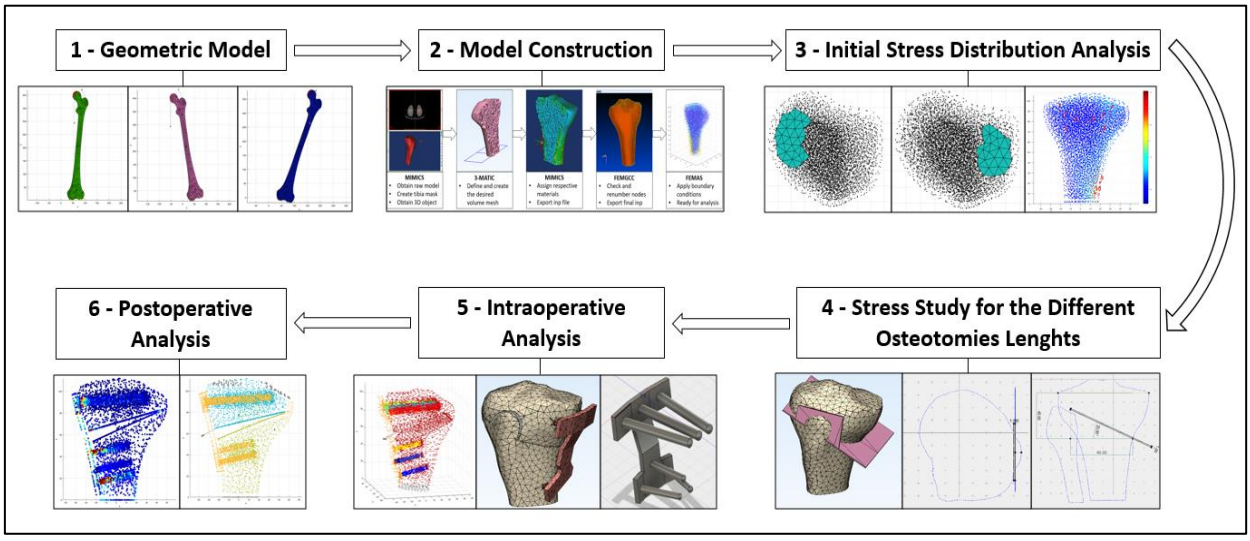

Figure 34 – Division of the Numeric Analysis, by steps.

4.2 Calculation of the tibial plateau forces

The forces applied on the femoral condyles are here considered the same as the ones applied on the tibial plateau (action-reaction pair). Considering an individual in a foot-standing position, only the forces along the frontal plane, at the tibiofemoral contact, are relevant (2D problem), all the rest, along the sagittal and transversal planes, can be excluded. The main purpose of this calculation is to obtain the medial and lateral condyle variation of the forces in the frontal plane, for equal varus and valgus deformities of the lower limb. In other words, it is assumed that a varus angle deformity, for example, occurs equally on both tibia and femur (Figure 35-b).

A left femur contour, projected on the coronal plane, was obtained from 3-MATIC® and MIMICS® software dataset (Figure 35-a). Then, the contour was obtained and an approximate geometry was constructed using FEMAS, in which was performed an Linear Elasto-Static Finite Element Analysis. FEMAS is a structural analysis software designed for students and developed by *Professor Jorge Belinha* (Thesis supervisor), running in MatLab® R2017a.

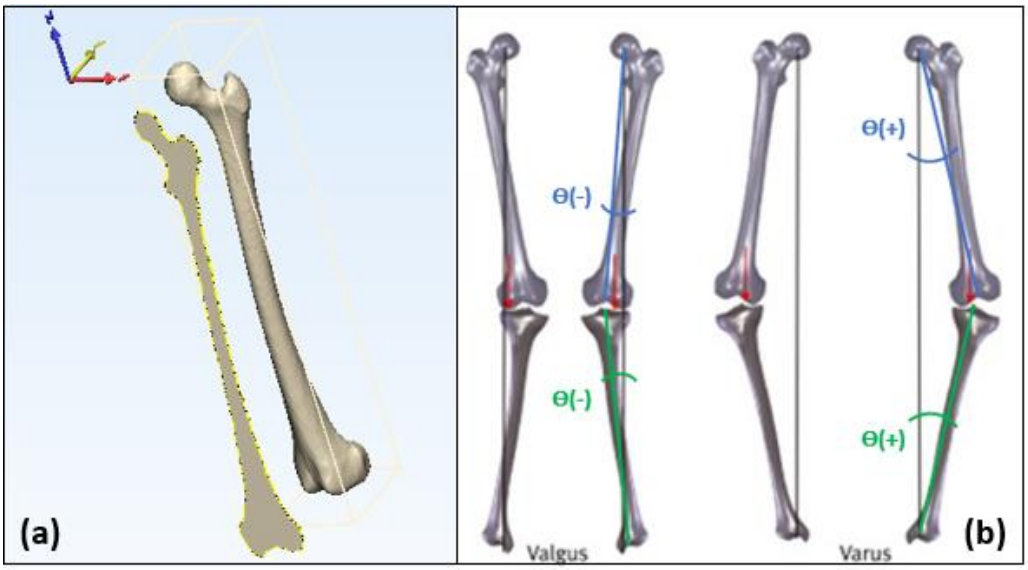

Figure 35 – Left: Projection of a femur contour in the coronal plane using 3-MATIC®. Right: Model assumption of which a tibial deformity leads to an equal deformity of the femur, being the positive angle a varus situation and negative, a valgus situation.

For this analysis, it is considered an individual with approximately 75 kg. This results in a pelvis-femoral contact force of 2317 N applied vertically on top of the femur head and another force of 703 N, with an inclination of 62° in the trochanter, which represents the tendons force that connect both femur and pelvis. The left\medial condyle and the right\lateral condyle are constrained on both *xx* and *yy* axis (two nodes each) and the femur head is also constrained in the x-axis (six nodes). (Figure 36) All boundary conditions are maintained for the different rotations: Counter clockwise rotation represents a varus deformation (positive angle), Figure 37-a, the opposite results in varus deformity (negative angle), Figure 37-b.

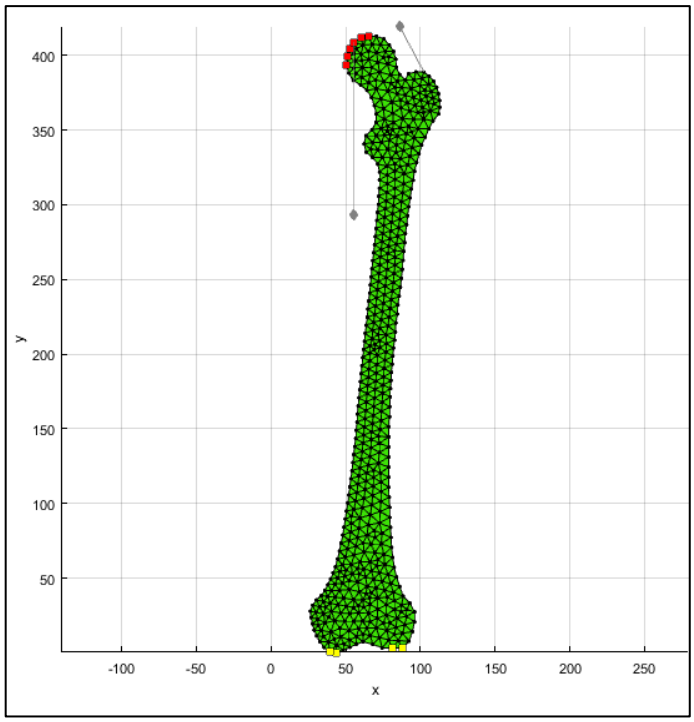

Figure 36 - Model meshed with all essential/natural boundary conditions defined, considering an individual with 75 kg on a foot-standing position.

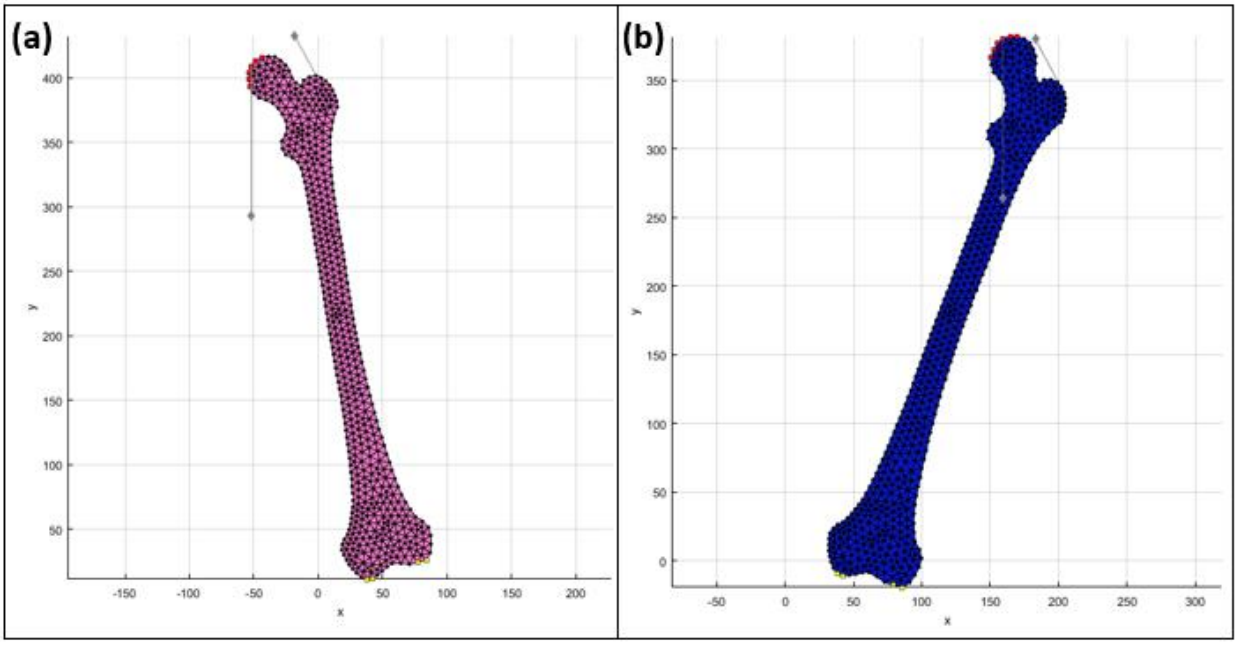

Figure 37 - (a) Varus deformity; (b) Valgus deformity; Respectively with a deformity angle of 15° and 15º .

To obtain the forces on both condyles, in FEMAS, a small programming routine, running in MatLab®, was created (**Annex A-1**) to select the constrained nodes, and sum both *xx* and *yy* values of the reaction forces. Those results together with the resultant force ($F_R = \sqrt{F_x^2 + F_y^2}$) for different valgus and varus rotations (± 5°, 10°, 15°) are written in Table 2 and represented in the following Figures Figure 38Figure 39Figure 40.

Table 2 - Results of the tibial plateau forces for the different situations.

	Lateral condyle			Medial condyle		
Situation	**Fx_dir**	**Fy_dir**	**Fr_dir**	**Fx_esq**	**Fy_esq**	**Fr_esq**
Normal	-167,62	1005,60	1019,47	209,28	690,72	721,73
Varus - 5º	-250,02	969,79	1001,50	147,79	727,11	741,98
Varus - 10º	-329,87	933,23	989,82	82,19	763,06	767,47
Varus - 15º	-408,23	897,11	985,63	11,47	799,18	799,26
Valgus - 5º	-81,39	1043,20	1046,37	267,36	653,12	705,73
Valgus - 10º	10,23	1082,90	1082,95	322,39	613,37	692,94
Valgus - 15º	109,28	1125,90	1131,19	374,36	570,34	682,23

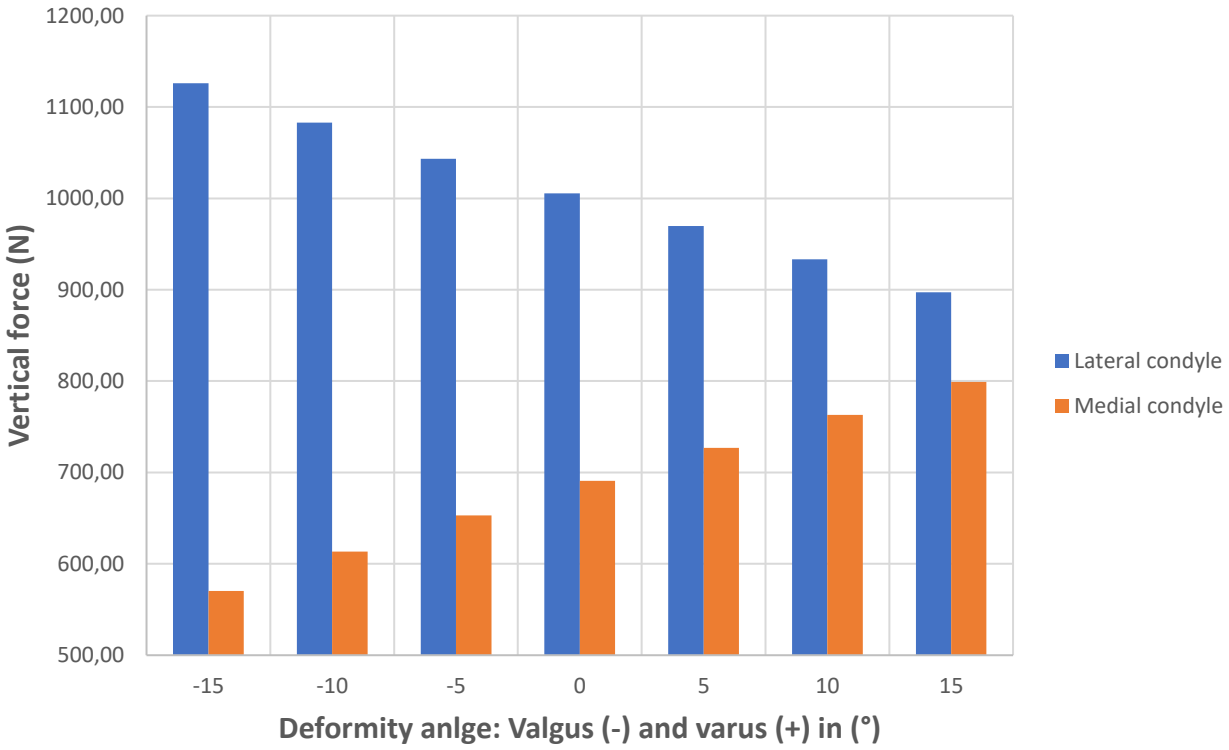

Figure 38 - Variation of the vertical force (Fyy), in the lateral and medial condyles, for the different deformity angles.

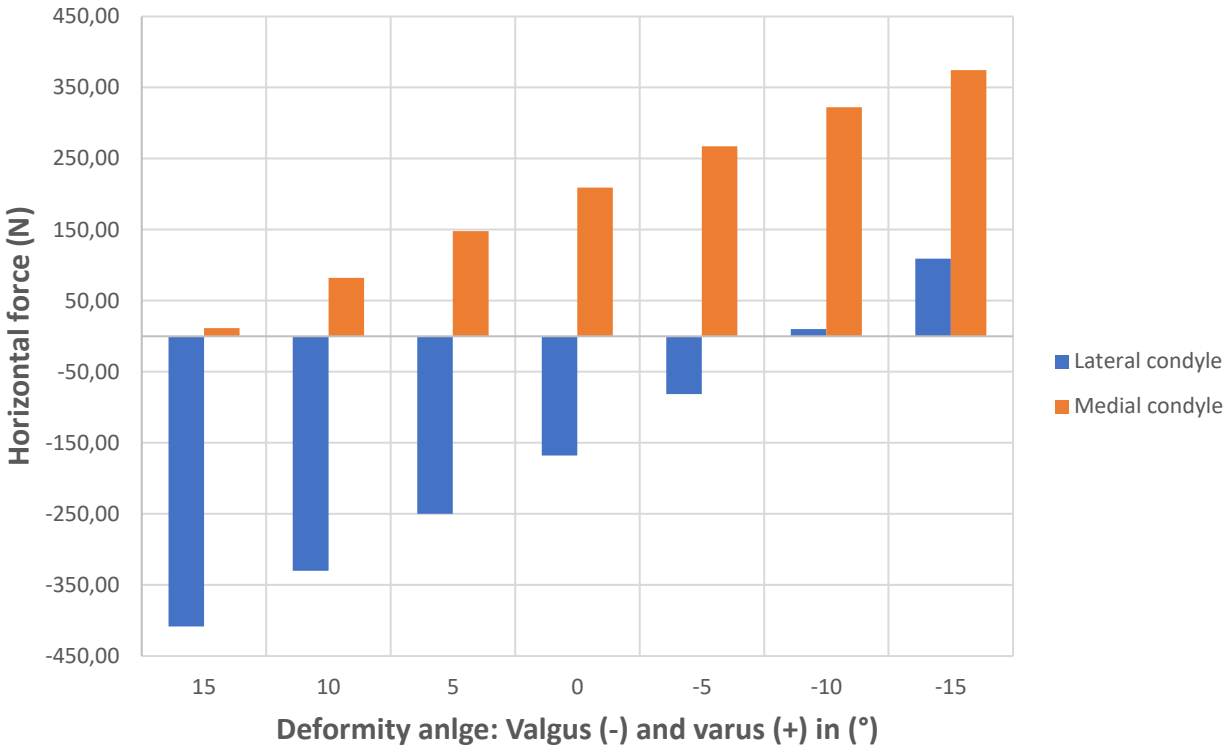

Figure 39 - Variation of the horizontal force (Fxx), in the lateral and medial condyles, for the different deformity angles.

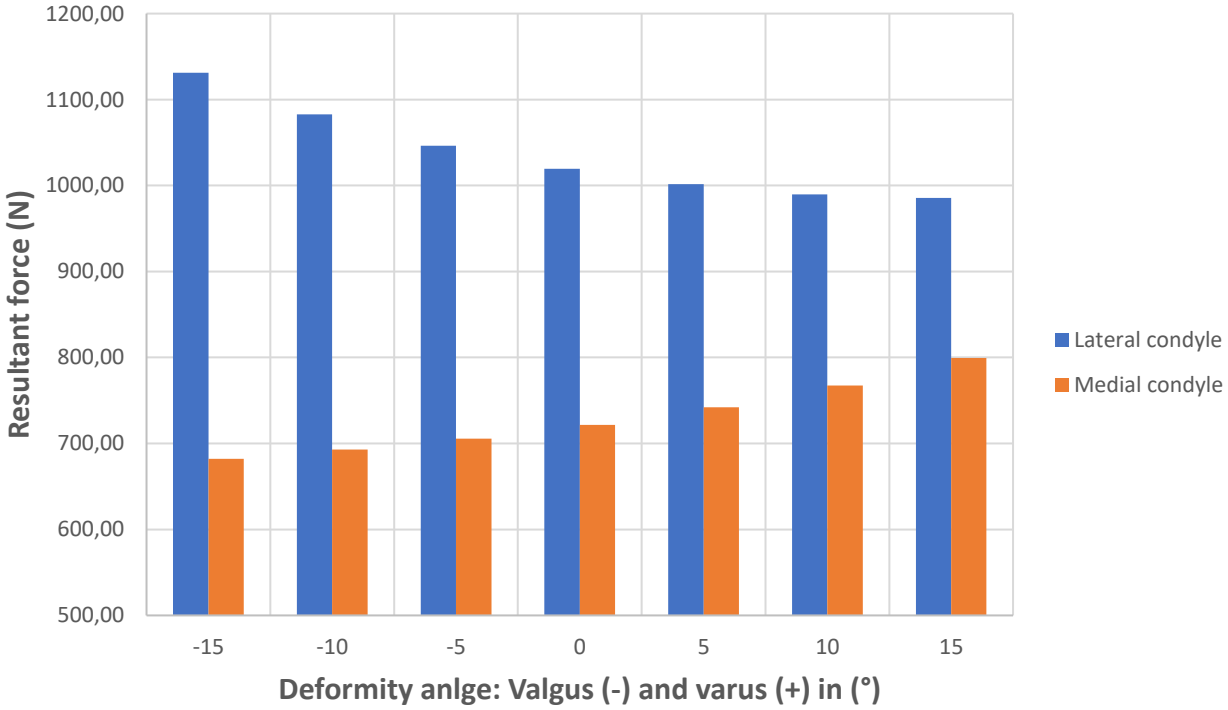

Figure 40 – Variation of the resultant force (Fr) in the lateral and medial condyles for the different deformity angles.

For the initial stress analysis, it will be considered three different situations, described in the following table.

Table 3 – Considered situations for the next simulations. Forces applied to proximal tibia.

	Lateral condyle			Medial condyle		
Situation	**Fx_dir**	**Fy_dir**	**Fr_dir**	**Fx_esq**	**Fy_esq**	**Fr_esq**
Valgus - 10°	-10,23	-1082,90	1082,95	-322,39	-613,37	692,94
Normal	167,62	-1005,60	1019,47	-209,28	-690,72	721,73
Varus + 10°	329,87	-933,23	989,82	-82,19	-763,06	767,47

Results show that the vertical force magnitude grows in the medial condyle for a crescent varus deformation (decreasing in the lateral site), and grows in the lateral condyle for a crescent valgus deformation (decreasing in the medial site).

The vertical force values are always higher in the lateral condyle of the femur, even for the maximum varus situation. This result goes against the assumption made by (Raja Izaham et al. 2012) which states that, in single limb stance with no varus or valgus deformities, the force is 60% more distributed in the medial condyle of the femur. And for the maximum varus situation, for example, the medial force should be even higher than that. This difference in results can be explained by the model assumptions (standing in two feet *vs* single limb stance), the femur contour geometry used and the simplified essential and natural boundary conditions applied.

4.3 General Model Construction

A Three-Dimensional model of the tibia was reconstructed from computed tomography images obtained from the anonymized medical images of MIMCS®. The thresholding procedure (mask creation) is performed and a 3D-object of the proximal tibia is obtained and directly copied to 3-MATIC® interface, in order to build an appropriate mesh. Then, it goes back to MIMICS® for the material assignment. Finally, an analysis file (*INP*) can be exported to a FEMGCC (Finite Element Generator Commercial Code) or directly to FEMAS, where the respective natural and essential conditions are applied in the tibia mesh. Figure 41 exemplifies the initial construction process of those models.

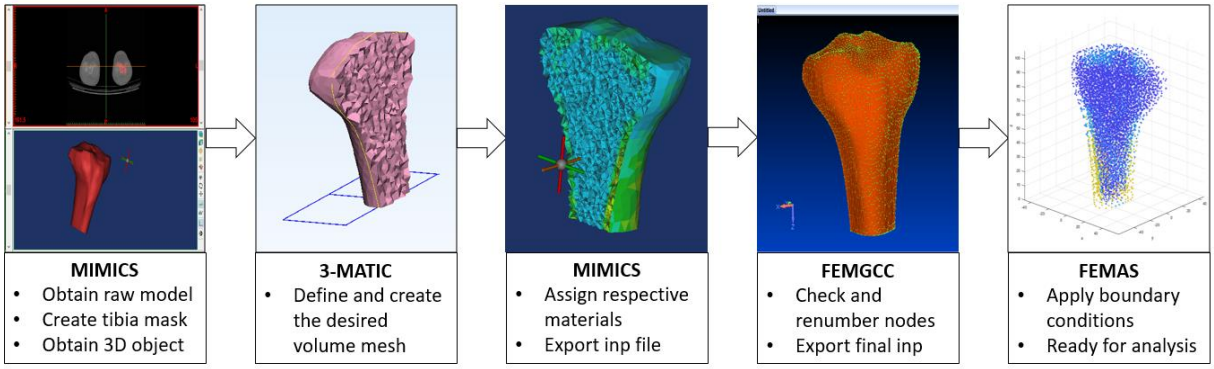

Figure 41 - General model construction process starting from the patient CT scans to FEMAS, for the FEM and RPIM analysis.

The mesh considered is divided in 3D tetrahedrons (C3D4 type) with a slightly more discretized interior, summing a total of 7082 nodes. The number of nodes had to be limited because of the academic software used (FEMAS), which is not suited for large calculus, and because of the lack of time, compromising some of the original bone shape.

4.3.1 Trabecular and Cortical Bone

Experimental studies show that the bone mechanical properties depend on the bone composition and on the bone porosity (directly related with the bone density). (Belinha 2014) So, defining the apparent density, ρ_{app}, and porosity, p, is important:

$$\rho_{app} = w_{sample}/V_{sample} \quad and \quad p = V_{holes}/V_{sample}$$
$$\rho_{app} = \rho_0 \cdot (1 - p) \tag{58}$$

where w_{sample} is the wet mineralised mass of bone of the sample tissue, V_{sample} the volume occupied by the same sample tissue, V_{holes} the volume of bone holes and ρ_0 the compact bone density which is considered to be $\rho_0 = 2.1\ (g/cm^3)$. (Belinha 2014)

The literature possesses several phenomenological laws, correlating the bone's apparent density with its mechanical properties. In this work it will be considered Lotz's material Law and Belinha's Material Law. (Belinha 2014)

Lotz's material law considers the bone orthotropic behaviour and determines the elasticity modulus and the ultimate compressive stress mathematical laws, for both cortical and trabecular bone, in the axial and transversal direction only using the apparent density as a variable:

$$E_i = a_1 \cdot (\rho_{app})^{a_2} \quad and \quad {\sigma_i}^c = a_3 \cdot (\rho_{app})^{a_4} \tag{59}$$

Being E_i the elasticity modulus and ${\sigma_i}^c$ the ultimate compression stress in direction i, both are expressed in MPa and the apparent density ρ_{app} in g/cm^3. The following table shows the coefficients a_j for the axial and transversal direction for both cortical and trabecular bone. (Belinha 2014)

Table 4 - Coefficients of Lotz Law.

Bone Tissue	Direction	a_1	a_2	a_3	a_4
Cortical	Axial	2,065E+03	3,090E+00	7,240E+00	1,880E+00
	Transversal	2,314E+03	1,570E+00	3,700E+01	1,510E+00
Trabecular	Axial	1,904E+03	1,640E+00	4,080E+01	1,890E+00
	Transversal	1,157E+03	1,780E+00	2,140E+01	1,370E+00

Belinha's Material Law is based on an experimental study and reinforces the idea that density is a salient property of bone and plays a crucial role in determining the mechanical properties of both its trabecular and cortical structural forms. (Belinha 2014) This experimentally based phenomenological law permits to differentiate the trabecular bone from the cortical bone based only in the apparent density measure. It is considered trabecular bone if $\rho_{app} \leq 1.3\ g/cm^3$, and cortical bone if: $\rho_{app} > 1.3\ g/cm^3$. The model assumes that the minimum apparent density is $\rho_{app}^{min} = 0.1\ g/cm^3$ and its maximum value is: $\rho_{app}^{max} = 2.1\ g/cm^3$. Thus, the bone elasticity modulus and the ultimate compression stress for the axial and transversal directions are calculated with the following,

$$E_{axial} \begin{cases} \sum_{j=0}^{3} a_j \cdot (\rho_{app})^j \ if \ \ \rho_{app} \leq 1.3\ g/cm^3 \\ \sum_{j=0}^{3} b_j \cdot (\rho_{app})^j \ if \ \ \rho_{app} > 1.3\ g/cm^3 \end{cases} \tag{60}$$

$$E_{trans} = \sum_{j=0}^{3} c_j \cdot (\rho_{app})^j \ , \qquad \sigma_{axial}^c = \sum_{j=0}^{3} d_j \cdot (\rho_{app})^j \ , \qquad \sigma_{trans}^c = \sum_{j=0}^{3} e_j \cdot (\rho_{app})^j \tag{61}$$

Where coefficients a_j, b_j, c_j, d_j and e_j are presented in the following table.

Table 5 - Coefficients of the propose bone tissue phenomenological model Coefficient.

Coefficient	*j=0*	*j=1*	*j=2*	*j=3*
a_j	0,000E+00	7,216E+02	8,059E+02	0,000E+00
b_j	-1,770E+05	3,861E+05	-2,798E+05	6,836E+04
c_j	0,000E+00	0,000E+00	2,004E+03	-1,442E+02
d_j	0,000E+00	0,000E+00	2,680E+01	2,035E+01
e_j	0,000E+00	0,000E+00	2,501E+01	1,247E+00

The ultimate tension stress of the bone tissue is usually defined as a proportion of the ultimate compression stress, $\sigma_i^t = \propto \cdot \sigma_i^c, with \propto \epsilon [0.33; 1]$. The shear ultimate stress (τ) varies between 49 MPa and 69 MPa. (Belinha 2014)

The following Figure 42, Figure 43, Figure 44 and Figure 45, are the graphic representation of the bone mechanical properties for each of the previous Material Laws, in function of the apparent density.

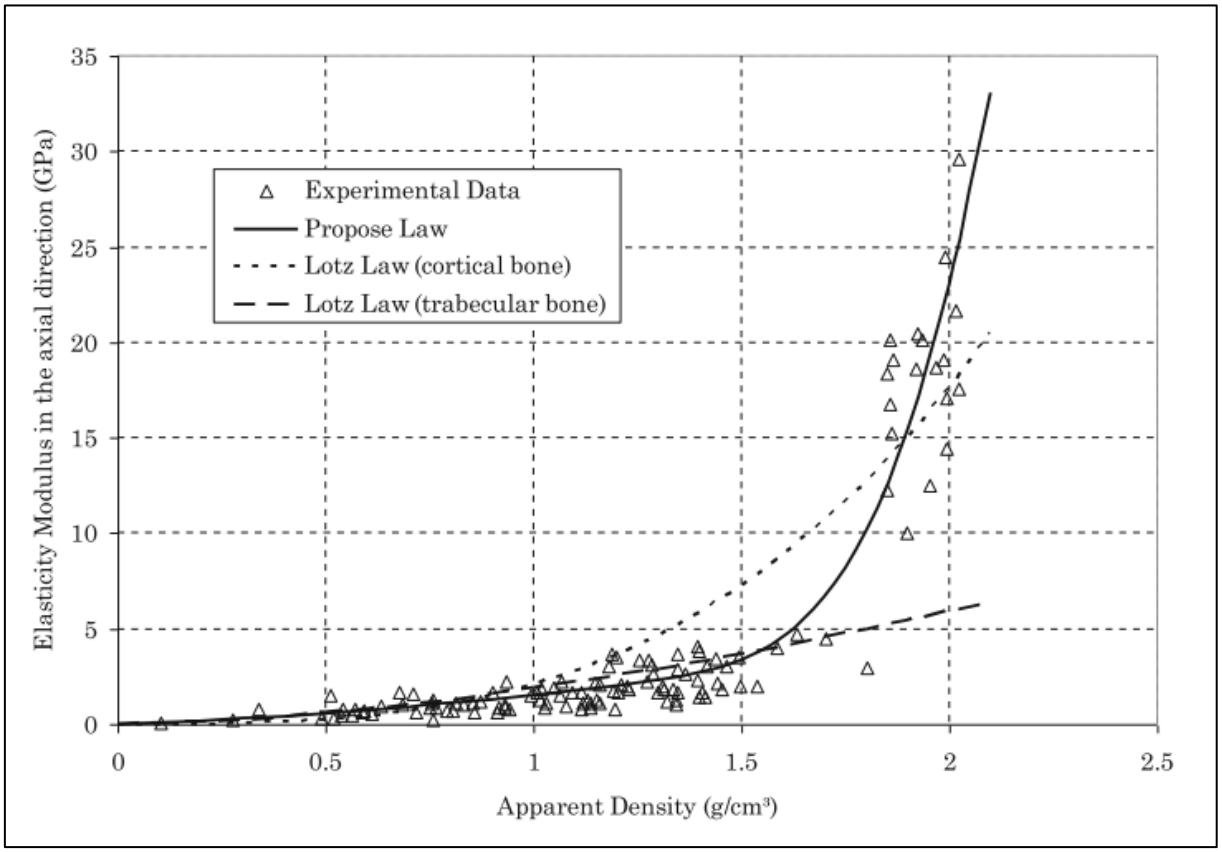

Figure 42 - Elasticity modulus in the axial direction. Experimental data obtain in Zioupos work compared with Lotz law for cortical and trabecular bone and with the mathematical model proposed by Professor Belinha. (Belinha 2014)

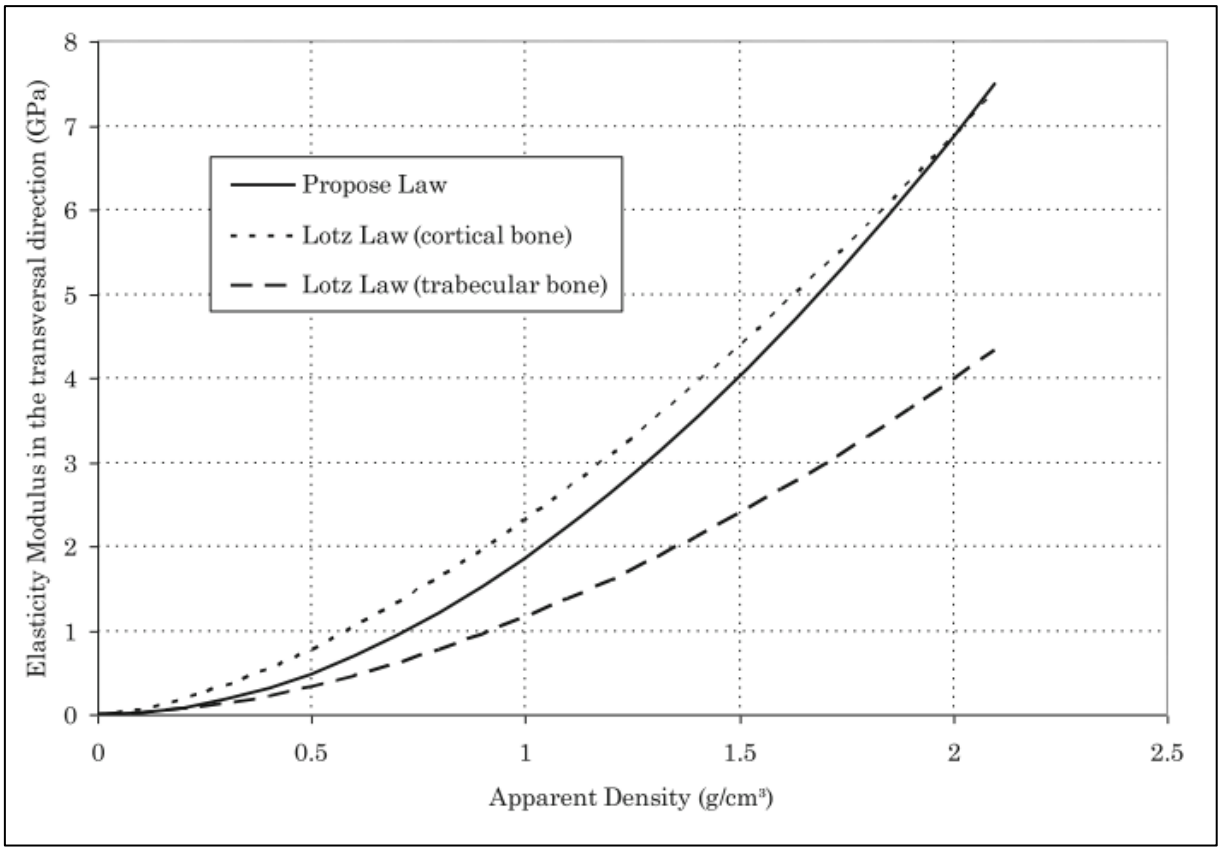

Figure 43 - Elasticity modulus in the transversal direction. Lotz law for cortical and trabecular bone compared with the mathematical model proposed by Professor Belinha. (Belinha 2014)

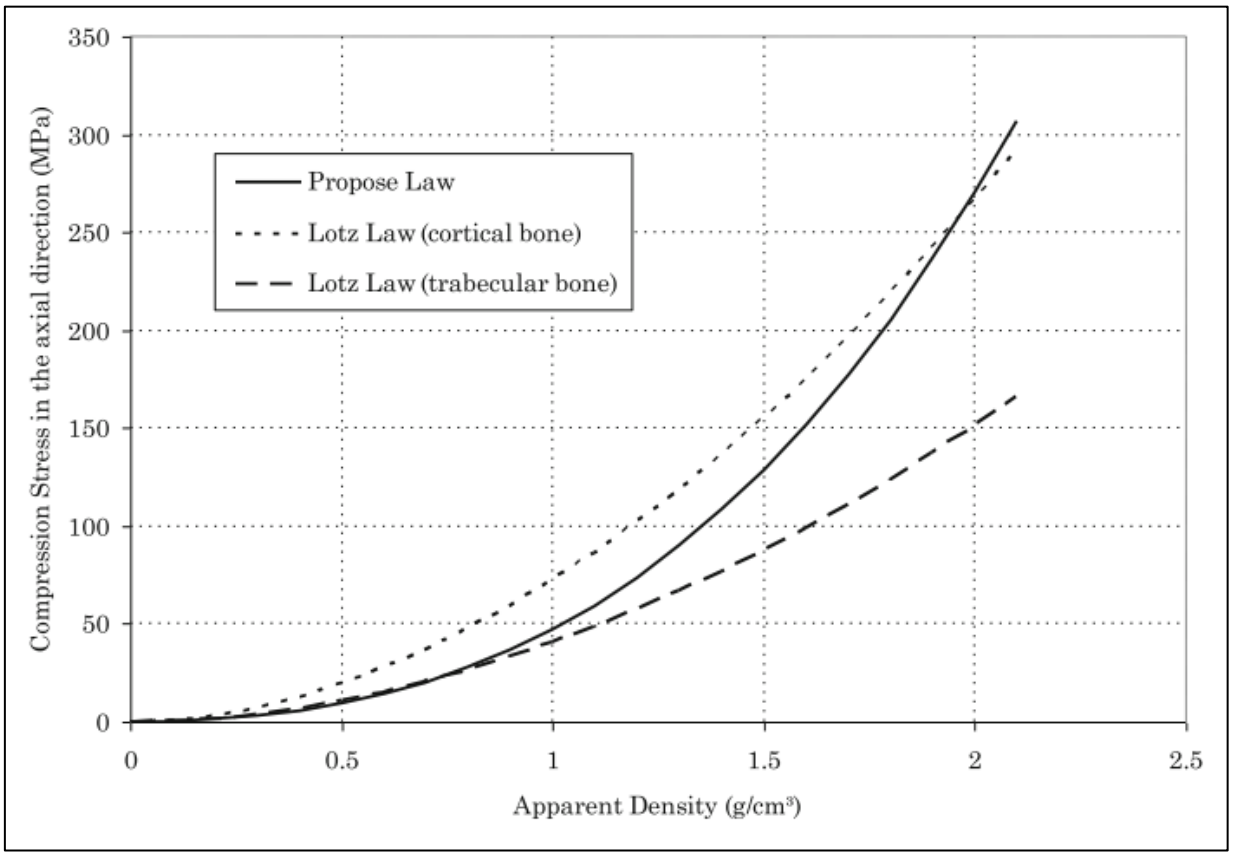

Figure 44 - Compression stress in the axial direction. Lotz law for cortical and trabecular bone compared with the mathematical model proposed by Professor Belinha. (Belinha 2014)

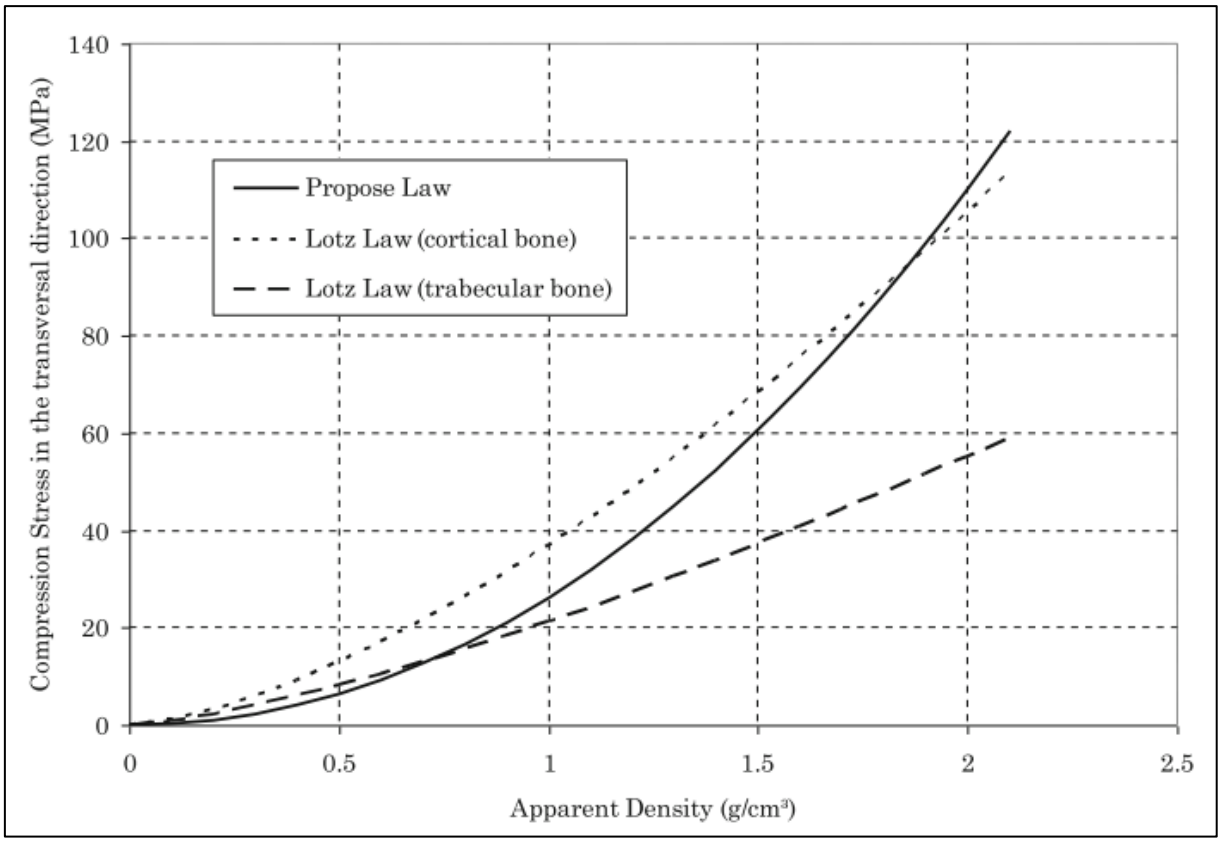

Figure 45 -Compression stress in the transversal direction. Lotz law for cortical and trabecular bone compared with the mathematical model proposed by Professor Belinha. (Belinha 2014)

4.3.2 Material Assignment

For the initial stress distribution analysis (**section 4.4**) there will be considered two distinct models, both obtained with MIMICS®: One model considering the bone as an homogeneous material and another model, considering three materials for the bone (cortical bone, dense trabecular bone and sparse trabecular bone. The material identification in MIMICS® is shown in Figure 46. Posteriorly, in the Numeric Analysis Chapter (**sections 4.5, 4.8, 4.9**), only the homogeneous case will be studied.

To obtain the different material densities, the following linear expression is considered:

$$\rho_i = \frac{(\rho_{máx} - \rho_{min}) * (HU_i - HU_{min})}{(HU_{máx} - HU_{min})} \tag{62}$$

Where the tibial threshold in a Hounsfield scale (HU) from -188 to 1588, and $\rho_{min} = 0{,}05\ g/cm^3$ and $\rho_{máx} = 2{,}1\ g/cm^3$. From 100 to 300 HU, the bone is trabecular and from 300 to 2000 HU, the bone is cortical.

The tibial model used possesses a HU range from -188 to 1588 HU. For higher simplicity, it will be considered Lotz Law for Cortical Bone: $E = 2065 * \rho^{3,09}$. This assumption has some error because there is some trabecular bone in the model (from -188 to 300 HU), but the majority is cortical (around 73%) and the approximation is reasonable. Other considerations could have been used, such as the Belinha's law, contemplating, with very high correlation, both cortical and trabecular bone properties, or even both Lotz expressions. The Poisson modulus is defined as 0,3. (Belinha 2014)

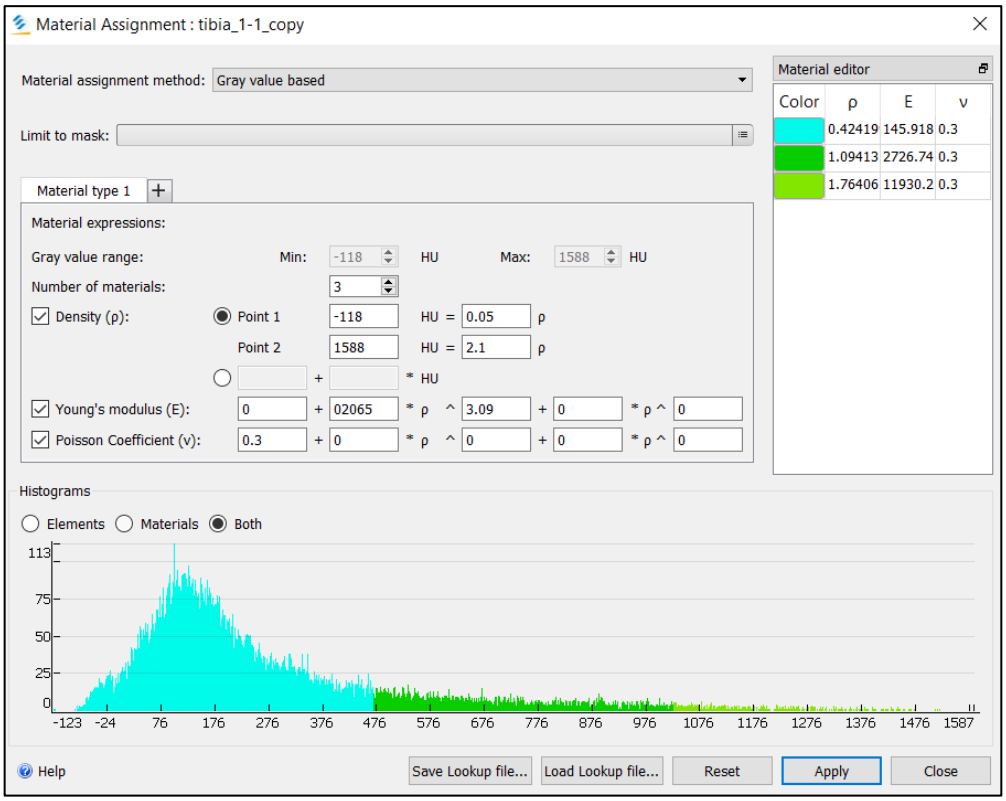

Figure 46 – Exemplification of the material assignment for the Three Materials tibia model, performed in MIMICS®.

The obtained mechanical properties with Lotz Law for cortical bone, are presented in the following table:

Table 6 – Material properties assignment for the Homogeneous and Three-material models.

Model	Density ρ (g/cm^3)	Young Elasticity Modulus [MPa]	Poisson Ratio (v)
Homogeneous	1,07461	2579,23	0.3
Three-Materials	0,42419	145,92	0.3
	1,09413	2726,74	
	1,76406	11930,20	

4.3.3 Fixation Implants

Nowadays, the most used material for making all kinds of prosthetics is Titanium (Ti), Cobalt Chromium alloy (Co-Cr) and Stainless Steel. In the present work, only the Titanium will be considered in the structural analysis. It's worth mentioning the use of composite PEEK by Arthrex® on their newly developed PEEKPower® plate for the OWHTO fixation.

Table 7 – Mechanical properties of the most commonly used materials of the fixation implants. ("CESEdupack" 2017)

Implant Material	Young Elasticity Modulus [GPa]	Poisson Ratio (ν)	Ultimate Compression Tension σ_c [MPa]
Pure Titanium (Ti)	110	0.3	275-290
Cobalt Chromium (Co-Cr)	220-230	0.3	440-460
Stainless Steel	200	0.3	190-220

4.4 Initial stress distribution analysis

This step has the objective of studying the initial stress for one (homogeneous) and for three assigned materials, considering the normal, varus and valgus situations (both with 10°). It's mainly important to evaluate the differences between the principal and the effective (von Mises) stress. Additionally, the results from FEM and RPIM are compared. To apply the medial and lateral forces (natural boundary conditions), an area of approximately the size of the meniscus is selected. The medial area selected was 731,2158 mm^3 and the lateral area was 613,3753 mm^3 (Figure 47).

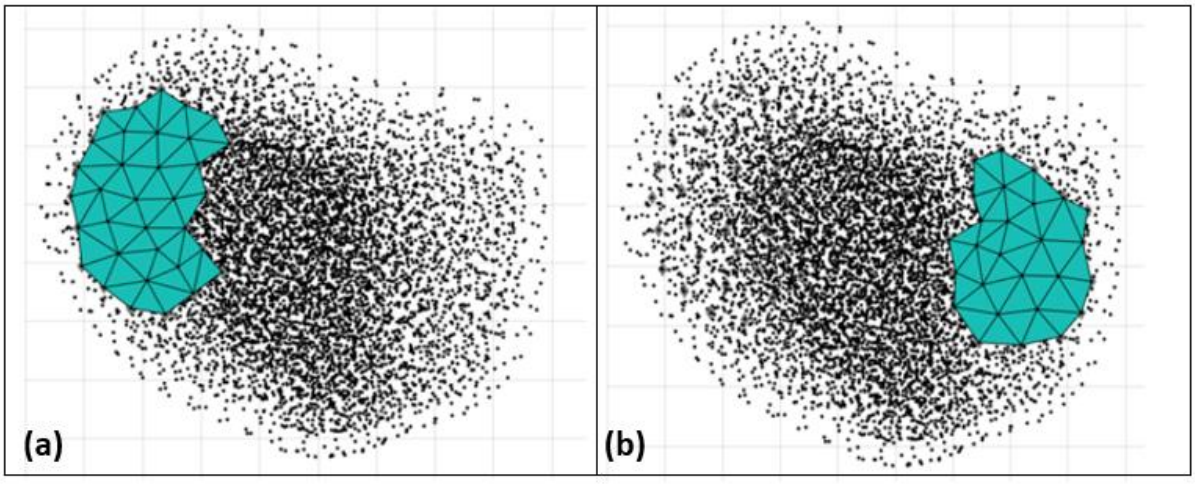

Figure 47 – (a) Medial area. (b) Lateral area, where the forces acting are distributed.

As essential boundary conditions, all bottom points of the tibia are fixed (displacement is null in every direction). The model is now ready for the Linear-Elasto-Static analysis using the two numeric methods.

Ten points, located inside the model and distributed in both medial and lateral sides, and at the medial bottom side of the tibia, are chosen for a stress evaluation. Their positions are represented in Figure 48 and are obtained, in Matlab® R2017a, using a programming routine (**Annex A-2**) that creates a cycle through all integration or Gauss points, and calculates the distance between them. The closest integration points, to the desired points coordinates, are selected by calculating the minimum value of the x-y planar distance between both.

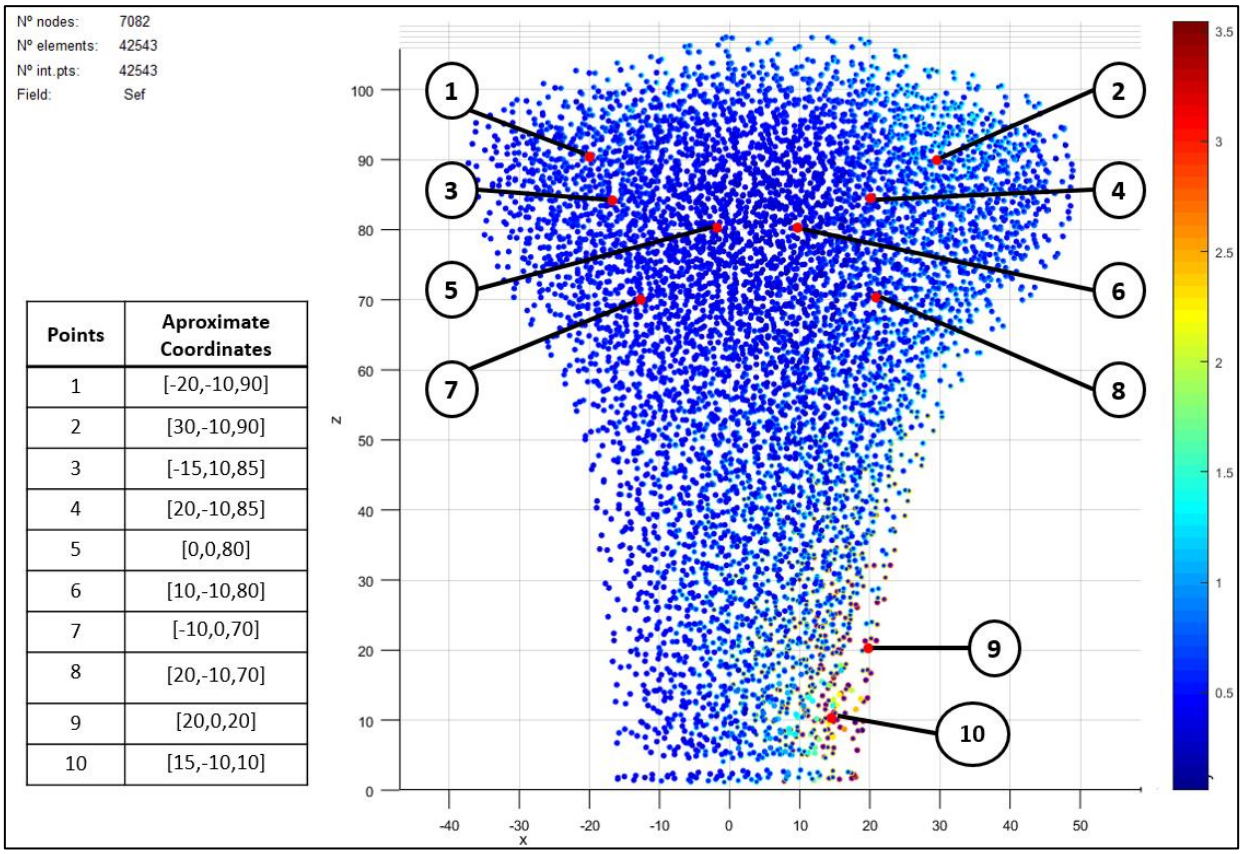

Points	Aproximate Coordinates
1	[-20,-10,90]
2	[30,-10,90]
3	[-15,10,85]
4	[20,-10,85]
5	[0,0,80]
6	[10,-10,80]
7	[-10,0,70]
8	[20,-10,70]
9	[20,0,20]
10	[15,-10,10]

Figure 48 - Tibia model with the points assigned for the stress analysis.

In Figure 49 the predefined RPIM parameters already implemented in FEMAS are declared. It was fixed the following parameters: each influence-domain is composed by a total of 27 nodes, and the *c* and *p* parameters used in the Interpolation Function (RBF) are equal to 1,42 and 1,03, respectively, and a linear polynomial basis is assumed. Concerning the integration, it was assumed one integration point inside each tetrahedral integration cell.

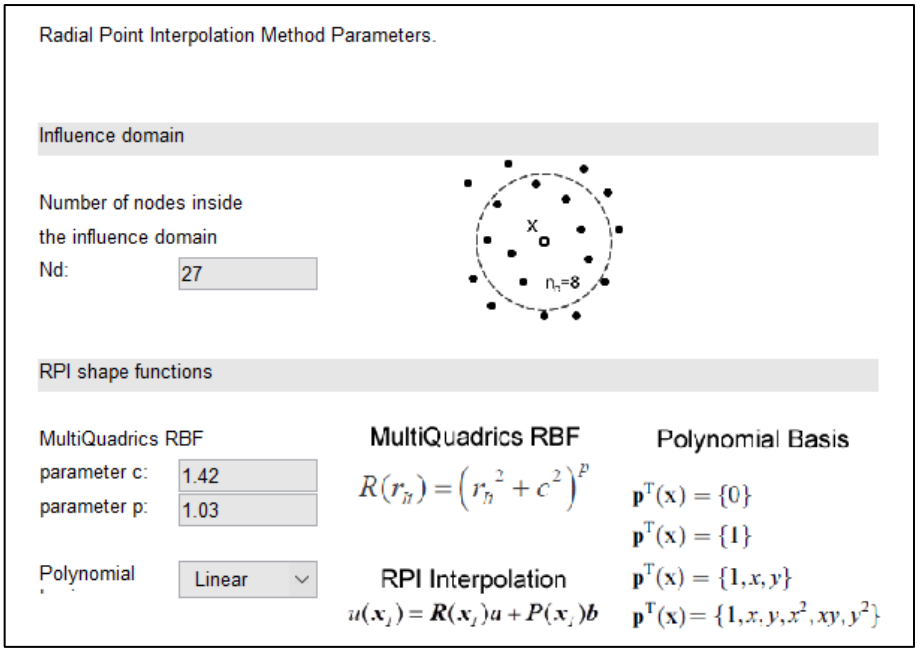

Figure 49 – FEMAS Interface with the predefined RPIM parameters.

The stress results, obtained from the FEM and the RPIM, are presented in the following tables in *MPa*.

Table 8 – Stress components in the tibial model (homogeneous material), for the normal situation, obtained with FEM [MPa].

Points	1	2	3	4	5	6	7	8	9	10
σ_{xx}	-0,118	0,340	0,140	-0,232	0,051	-0,042	-0,064	-0,232	-0,069	0,003
σ_{yy}	0,058	-0,249	0,044	-0,026	0,102	0,012	-0,041	-0,026	-0,041	0,059
σ_{zz}	-0,353	-1,373	-0,516	-1,138	-0,409	-1,679	-0,636	-1,138	-2,162	-0,614
τ_{xy}	0,004	-0,006	-0,010	0,001	-0,007	-0,015	0,022	0,001	0,059	-0,024
τ_{yz}	-0,050	0,025	0,029	0,091	0,059	0,040	-0,080	0,091	0,097	0,098
τ_{zx}	0,206	-0,088	0,191	-0,325	0,118	0,014	0,138	-0,325	-0,434	-0,124
σ_{ef}	0,512	1,515	0,699	1,180	0,538	1,667	0,648	1,180	2,246	0,704
σ_1	0,068	0,345	0,192	-0,014	0,110	0,017	-0,027	-0,014	0,038	0,096
σ_2	-0,006	-0,249	0,046	-0,134	0,078	-0,045	-0,035	-0,134	-0,057	0,001
σ_3	-0,476	-1,378	-0,569	-1,249	-0,444	-1,680	-0,679	-1,249	-2,254	-0,650

Table 9 - Stress components in the tibial model (homogeneous material), for the normal situation, obtained with RPIM [MPa].

Points	1	2	3	4	5	6	7	8	9	10
σ_{xx}	-0,208	-0,004	0,183	-0,348	0,001	-0,097	-0,071	-0,348	-0,199	-0,016
σ_{yy}	0,006	-0,448	0,059	-0,063	0,057	-0,033	0,007	-0,063	-0,165	0,042
σ_{zz}	-0,394	-1,866	-0,457	-1,275	-0,471	-1,819	-0,562	-1,275	-2,368	-0,680
τ_{xy}	0,024	0,039	-0,010	-0,041	-0,024	0,027	0,002	-0,041	0,097	-0,022
τ_{yz}	-0,078	-0,345	-0,002	0,039	0,044	0,113	-0,067	0,039	0,132	0,087
τ_{zx}	0,259	-0,026	0,177	-0,395	0,129	-0,109	0,182	-0,395	-0,620	-0,111
σ_{ef}	0,584	1,790	0,663	1,297	0,557	1,777	0,631	1,297	2,452	0,737
σ_1	0,027	0,001	0,229	-0,046	0,066	-0,020	0,024	-0,046	-0,010	0,069
σ_2	-0,038	-0,373	0,059	-0,220	0,029	-0,095	-0,022	-0,220	-0,179	-0,016
σ_3	-0,587	-1,946	-0,503	-1,421	-0,508	-1,833	-0,629	-1,421	-2,543	-0,707

Table 10 - Stress components in the tibial model (heterogeneous distribution with three materials: cortical bone, dense and sparse trabecular bone), for the normal situation, obtained with FEM [MPa].

Points	**1**	**2**	**3**	**4**	**5**	**6**	**7**	**8**	**9**	**10**
σ_{xx}	0,060	0,442	-0,076	-0,014	-0,030	-0,014	-0,039	-0,014	-0,001	-0,037
σ_{yy}	-0,016	-0,064	-0,151	0,012	0,039	0,004	-0,002	0,012	-0,007	0,024
σ_{zz}	-0,499	-0,666	-2,270	-0,225	-0,244	-0,075	-0,101	-0,225	-0,084	-0,246
τ_{xy}	0,072	-0,012	-0,090	0,014	-0,003	0,000	0,004	0,014	0,003	-0,012
τ_{yz}	-0,127	-0,007	-0,490	0,035	0,040	-0,002	0,015	0,035	0,052	0,027
τ_{zx}	-0,012	-0,095	-0,278	-0,001	0,054	0,005	-0,033	-0,001	-0,006	-0,046
σ_{ef}	0,583	0,975	2,374	0,234	0,281	0,072	0,107	0,234	0,121	0,263
σ_1	0,114	0,451	-0,013	0,023	0,045	0,004	0,000	0,023	0,020	0,031
σ_2	-0,039	-0,064	-0,069	-0,020	-0,018	-0,014	-0,025	-0,020	-0,001	-0,032
σ_3	-0,530	-0,674	-2,414	-0,230	-0,262	-0,076	-0,117	-0,230	-0,110	-0,257

Table 11 - Stress components in the tibial model (heterogeneous distribution with three materials: cortical bone, dense and sparse trabecular bone), for the normal situation, obtained with RPIM [MPa].

Points	**1**	**2**	**3**	**4**	**5**	**6**	**7**	**8**	**9**	**10**
σ_{xx}	-0,067	0,180	0,006	-0,106	-0,063	-0,041	-0,026	-0,106	-0,095	-0,045
σ_{yy}	-0,148	-0,269	-0,012	-0,073	0,036	0,006	-0,004	-0,073	-0,114	0,027
σ_{zz}	-0,567	-1,361	-0,409	-0,570	-0,330	-0,150	-0,118	-0,570	-0,417	-0,461
τ_{xy}	0,082	-0,027	0,026	-0,037	-0,011	-0,014	-0,012	-0,037	-0,013	-0,022
τ_{yz}	-0,135	-0,355	-0,095	0,031	0,051	-0,013	0,018	0,031	0,053	0,044
τ_{zx}	0,081	-0,233	0,124	-0,041	0,098	-0,011	0,006	-0,041	-0,089	-0,047
σ_{ef}	0,557	1,558	0,606	0,494	0,380	0,143	0,111	0,494	0,361	0,471
σ_1	-0,016	0,216	0,100	-0,044	0,043	0,010	0,003	-0,044	-0,059	0,039
σ_2	-0,140	-0,168	0,030	-0,130	-0,031	-0,043	-0,030	-0,130	-0,120	-0,049
σ_3	-0,625	-1,498	-0,538	-0,575	-0,368	-0,152	-0,121	-0,575	-0,447	-0,470

Table 12 - Stress components in the tibial model (homogeneous material), for the 10° varus situation, obtained with FEM [MPa].

Points	1	2	3	4	5	6	7	8	9	10
σ_{xx}	-0,122	0,559	0,120	-0,201	0,040	-0,029	0,032	-0,201	0,045	0,054
σ_{yy}	0,058	-0,162	0,045	-0,037	0,088	-0,011	0,098	-0,037	-0,009	0,055
σ_{zz}	-0,152	-1,269	-0,531	-1,533	-0,414	-2,591	0,269	-1,533	-3,333	-0,667
τ_{xy}	0,002	-0,020	-0,018	-0,012	-0,006	-0,065	-0,011	-0,012	0,053	-0,025
τ_{yz}	-0,046	0,034	0,065	0,094	0,063	0,051	0,053	0,094	-0,010	0,110
τ_{zx}	0,197	0,029	0,274	-0,276	0,282	0,441	0,247	-0,276	-0,472	0,017
σ_{ef}	0,402	1,597	0,787	1,509	0,693	2,685	0,486	1,509	3,451	0,748
σ_1	0,091	0,560	0,220	-0,024	0,180	0,079	0,429	-0,024	0,131	0,087
σ_2	0,031	-0,162	0,052	-0,154	0,088	-0,044	0,099	-0,154	-0,030	0,039
σ_3	-0,338	-1,271	-0,637	-1,593	-0,554	-2,666	-0,130	-1,593	-3,398	-0,684

Table 13 - Stress components in the tibial model (homogeneous material), for the 10° varus situation, obtained with RPIM [MPa].

Points	1	2	3	4	5	6	7	8	9	10
σ_{xx}	0,011	0,225	0,166	-0,327	-0,005	-0,086	-0,161	-0,327	-0,163	0,021
σ_{yy}	0,071	-0,351	0,060	-0,094	0,055	-0,073	-0,022	-0,094	-0,176	0,028
σ_{zz}	-0,471	-1,753	-0,481	-1,721	-0,469	-2,844	0,119	-1,721	-3,631	-0,753
τ_{xy}	0,001	0,102	-0,013	-0,058	-0,022	0,027	-0,008	-0,058	0,106	-0,021
τ_{yz}	0,009	-0,317	0,026	0,025	0,058	0,190	0,077	0,025	0,037	0,096
τ_{zx}	0,270	0,113	0,256	-0,353	0,316	0,158	0,359	-0,353	-0,792	0,031
σ_{ef}	0,695	1,864	0,749	1,645	0,746	2,798	0,681	1,645	3,729	0,798
σ_1	0,132	0,245	0,255	-0,072	0,155	-0,030	0,374	-0,072	0,049	0,051
σ_2	0,070	-0,294	0,061	-0,266	0,060	-0,107	-0,024	-0,266	-0,216	0,012
σ_3	-0,592	-1,830	-0,572	-1,805	-0,634	-2,865	-0,413	-1,805	-3,805	-0,766

Table 14 - Stress components in the tibial model (heterogeneous distribution with three materials: cortical bone, dense and sparse trabecular bone), for the 10° varus situation, obtained with FEM [MPa].

Points	**1**	**2**	**3**	**4**	**5**	**6**	**7**	**8**	**9**	**10**
σ_{xx}	0,036	0,729	0,039	0,001	-0,040	-0,034	-0,131	0,001	0,016	-0,030
σ_{yy}	-0,059	-0,033	0,021	0,018	0,032	-0,004	0,148	0,018	0,017	0,026
σ_{zz}	-0,217	-1,026	-0,551	-0,482	-0,306	-0,199	-0,997	-0,482	-0,257	-0,431
τ_{xy}	0,053	-0,022	-0,043	0,023	-0,014	-0,017	-0,218	0,023	-0,011	-0,029
τ_{yz}	-0,100	-0,003	0,126	0,078	0,071	0,010	0,605	0,078	0,099	0,060
τ_{zx}	0,075	-0,080	0,203	0,068	0,209	0,086	1,375	0,068	0,012	0,044
σ_{ef}	0,323	1,531	0,717	0,525	0,493	0,237	2,825	0,525	0,324	0,454
σ_1	0,064	0,733	0,103	0,054	0,086	0,011	0,928	0,054	0,050	0,042
σ_2	-0,013	-0,034	0,047	-0,015	0,032	-0,012	0,262	-0,015	0,015	-0,033
σ_3	-0,291	-1,030	-0,641	-0,502	-0,432	-0,237	-2,170	-0,502	-0,289	-0,445

Table 15 - Stress components in the tibial model (heterogeneous distribution with three materials: cortical bone, dense and sparse trabecular bone), for the 10° varus situation, obtained with RPIM [MPa].

Points	**1**	**2**	**3**	**4**	**5**	**6**	**7**	**8**	**9**	**10**
σ_{xx}	-0,077	0,445	0,063	-0,103	-0,061	-0,039	-0,022	-0,103	-0,115	-0,031
σ_{yy}	-0,193	-0,130	0,013	-0,104	0,028	0,010	-0,033	-0,104	-0,131	0,023
σ_{zz}	-0,277	-1,252	-0,532	-0,710	-0,349	-0,204	-0,081	-0,710	-0,601	-0,484
τ_{xy}	0,077	0,023	-0,029	-0,049	-0,022	-0,027	-0,040	-0,049	-0,033	-0,028
τ_{yz}	-0,125	-0,319	0,093	0,052	0,067	-0,001	0,080	0,052	0,052	0,060
τ_{zx}	0,125	-0,150	0,198	0,014	0,241	0,029	0,104	0,014	-0,105	0,048
σ_{ef}	0,376	1,615	0,688	0,620	0,552	0,206	0,244	0,620	0,523	0,502
σ_1	-0,015	0,463	0,123	-0,053	0,080	0,023	0,061	-0,053	-0,065	0,038
σ_2	-0,105	-0,053	0,028	-0,149	0,032	-0,047	0,008	-0,149	-0,156	-0,033
σ_3	-0,428	-1,347	-0,607	-0,715	-0,494	-0,209	-0,205	-0,715	-0,627	-0,496

Table 16 - Stress components in the tibial model (homogeneous material), for the 10° valgus situation, obtained with FEM [MPa].

Points	1	2	3	4	5	6	7	8	9	10
σ_{xx}	-0,112	0,097	0,155	-0,262	0,056	-0,056	-0,157	-0,262	-0,183	-0,050
σ_{yy}	0,057	-0,341	0,044	-0,015	0,116	0,034	-0,177	-0,015	-0,073	0,065
σ_{zz}	-0,545	-1,485	-0,498	-0,749	-0,406	-0,774	-1,531	-0,749	-1,000	-0,566
τ_{xy}	0,006	0,010	-0,003	0,014	-0,007	0,036	0,054	0,014	0,064	-0,023
τ_{yz}	-0,052	0,015	-0,007	0,086	0,055	0,026	-0,209	0,086	0,199	0,084
τ_{zx}	0,210	-0,214	0,109	-0,373	-0,045	-0,415	0,027	-0,373	-0,395	-0,265
σ_{ef}	0,656	1,463	0,633	0,926	0,510	1,053	1,416	0,926	1,170	0,756
σ_1	0,063	0,125	0,173	0,005	0,124	0,139	-0,101	0,005	-0,012	0,120
σ_2	-0,029	-0,341	0,044	-0,073	0,058	0,031	-0,201	-0,073	-0,045	0,013
σ_3	-0,634	-1,514	-0,515	-0,958	-0,416	-0,964	-1,564	-0,958	-1,198	-0,684

Table 17 - Stress components in the tibial model (homogeneous material), for the 10° valgus situation, obtained with RPIM [MPa].

Points	1	2	3	4	5	6	7	8	9	10
σ_{xx}	-0,218	-0,256	0,195	-0,367	0,003	-0,107	0,019	-0,367	-0,233	-0,053
σ_{yy}	-0,003	-0,548	0,059	-0,032	0,061	0,008	0,035	-0,032	-0,151	0,057
σ_{zz}	-0,642	-1,988	-0,431	-0,835	-0,475	-0,800	-1,236	-0,835	-1,112	-0,612
τ_{xy}	0,028	-0,028	-0,007	-0,024	-0,024	0,028	0,011	-0,024	0,086	-0,022
τ_{yz}	-0,082	-0,376	-0,028	0,050	0,030	0,031	-0,207	0,050	0,222	0,076
τ_{zx}	0,285	-0,175	0,098	-0,436	-0,057	-0,378	0,004	-0,436	-0,448	-0,252
σ_{ef}	0,764	1,760	0,597	1,033	0,523	1,003	1,313	1,033	1,274	0,771
σ_1	0,008	-0,239	0,210	-0,009	0,074	0,062	0,070	-0,009	-0,045	0,101
σ_2	-0,077	-0,457	0,060	-0,128	-0,002	0,006	0,017	-0,128	-0,105	0,005
σ_3	-0,795	-2,097	-0,447	-1,097	-0,483	-0,968	-1,269	-1,097	-1,347	-0,714

Table 18 - Stress components in the tibial model (heterogeneous distribution with three materials: cortical bone, dense and sparse trabecular bone), for the 10° valgus situation, obtained with FEM [MPa].

Points	**1**	**2**	**3**	**4**	**5**	**6**	**7**	**8**	**9**	**10**
σ_{xx}	0,053	0,234	0,052	-0,019	-0,049	-0,019	-0,082	-0,019	-0,007	-0,064
σ_{yy}	0,012	-0,229	0,031	0,020	0,059	0,013	0,014	0,020	-0,022	0,036
σ_{zz}	-0,538	-1,263	-0,543	-0,309	-0,274	-0,072	-0,138	-0,309	-0,094	-0,411
τ_{xy}	0,073	0,020	-0,011	0,022	0,013	0,004	0,016	0,022	0,010	-0,018
τ_{yz}	-0,132	-0,014	0,066	0,032	0,050	-0,015	0,007	0,032	0,068	0,024
τ_{zx}	-0,041	-0,250	0,033	-0,042	-0,039	-0,038	-0,079	-0,042	-0,018	-0,147
σ_{ef}	0,632	1,397	0,599	0,327	0,315	0,102	0,193	0,327	0,147	0,482
σ_1	0,127	0,276	0,057	0,030	0,067	0,020	0,017	0,030	0,018	0,048
σ_2	-0,032	-0,230	0,036	-0,020	-0,042	-0,005	-0,028	-0,020	-0,004	-0,021
σ_3	-0,569	-1,304	-0,552	-0,319	-0,288	-0,092	-0,195	-0,319	-0,138	-0,465

Table 19 - Stress components in the tibial model (heterogeneous distribution with three materials: cortical bone, dense and sparse trabecular bone), for the 10° valgus situation, obtained with RPIM [MPa].

Points	**1**	**2**	**3**	**4**	**5**	**6**	**7**	**8**	**9**	**10**
σ_{xx}	-0,056	-0,113	0,088	-0,109	-0,068	-0,043	-0,029	-0,109	-0,074	-0,059
σ_{yy}	-0,098	-0,415	0,030	-0,042	0,044	0,001	0,024	-0,042	-0,096	0,031
σ_{zz}	-0,845	-1,480	-0,480	-0,432	-0,313	-0,096	-0,154	-0,432	-0,234	-0,443
τ_{xy}	0,085	-0,082	-0,010	-0,025	0,001	0,000	0,016	-0,025	0,006	-0,016
τ_{yz}	-0,142	-0,393	0,044	0,009	0,035	-0,025	-0,045	0,009	0,052	0,027
τ_{zx}	0,035	-0,320	0,034	-0,096	-0,045	-0,050	-0,092	-0,096	-0,073	-0,143
σ_{ef}	0,823	1,529	0,550	0,400	0,332	0,129	0,239	0,400	0,216	0,504
σ_1	0,016	-0,041	0,091	-0,029	0,048	0,012	0,059	-0,029	-0,042	0,042
σ_2	-0,140	-0,287	0,033	-0,096	-0,060	-0,020	-0,011	-0,096	-0,086	-0,022
σ_3	-0,875	-1,679	-0,486	-0,458	-0,324	-0,130	-0,207	-0,458	-0,276	-0,491

The obtained Effective and Principal Stress components are picked for a comparison between FEM and RPIM. Only the values from the normal situation are here considered, in *MPa*.

Table 20 – Effective Stress obtained with FEM and RPIM for both models (homogeneous material distribution and heterogeneous material distributing) [MPa].

		1	2	3	4	5	6	7	8	9	10
σ_{ef}	**RPIM 1 mat**	0,584	1,790	0,663	1,297	0,557	1,777	0,631	1,297	2,452	0,737
	FEM 1 mat	0,512	1,515	0,699	1,180	0,538	1,667	0,648	1,180	2,246	0,704
	RPIM 3 mat	0,557	1,558	0,606	0,494	0,380	0,143	0,111	0,494	0,361	0,471
	FEM 3 mat	0,583	0,975	2,374	0,234	0,281	0,072	0,107	0,234	0,121	0,263

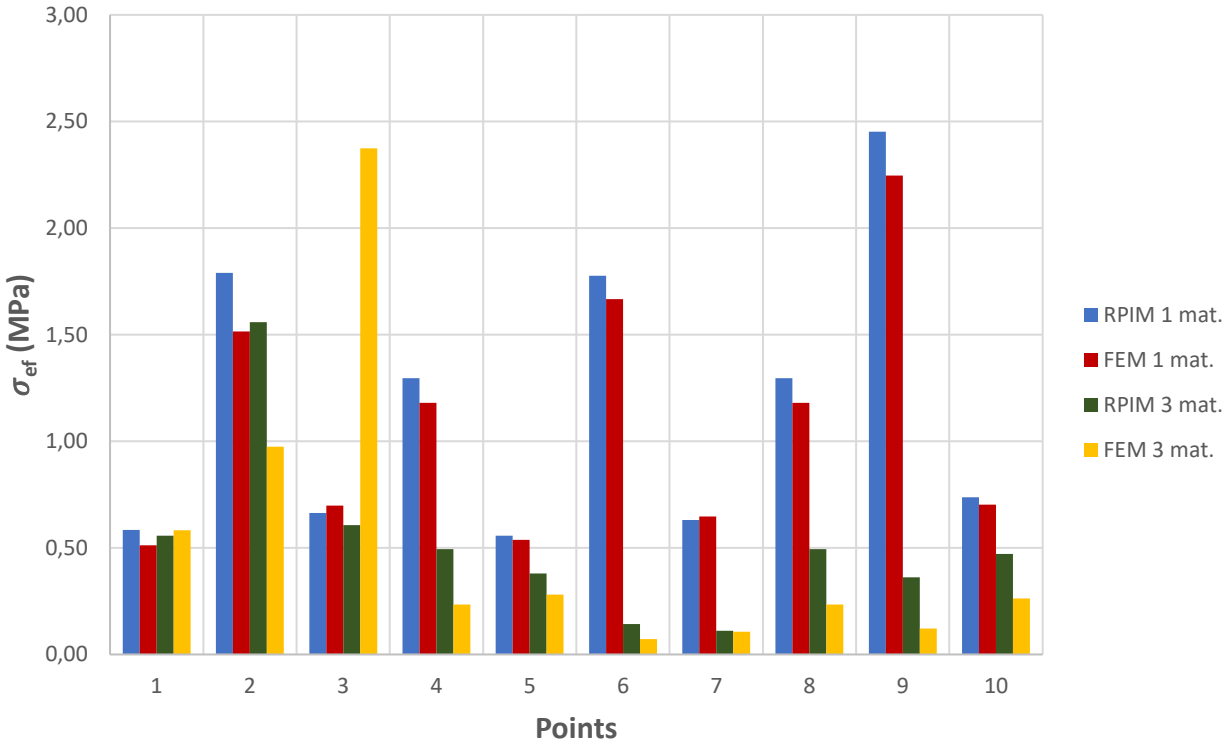

Figure 50 – Effective Stress comparison between FEM and RPIM, for both models (homogeneous material distribution and heterogeneous material distributing) [MPa].

Table 21 – Principal Stress component σ_{11} obtained with FEM and RPIM for both models (homogeneous material distribution and heterogeneous material distributing) [MPa].

		1	2	3	4	5	6	7	8	9	10
σ_{11}	**RPIM 1 mat**	0,027	0,001	0,229	-0,046	0,066	-0,020	0,024	-0,046	-0,010	0,069
	FEM 1 mat	0,068	0,345	0,192	-0,014	0,110	0,017	-0,027	-0,014	0,038	0,096
	RPIM 3 mat	-0,016	0,216	0,100	-0,044	0,043	0,010	0,003	-0,044	-0,059	0,039
	FEM 3 mat	0,114	0,451	-0,013	0,023	0,045	0,004	0,000	0,023	0,020	0,031

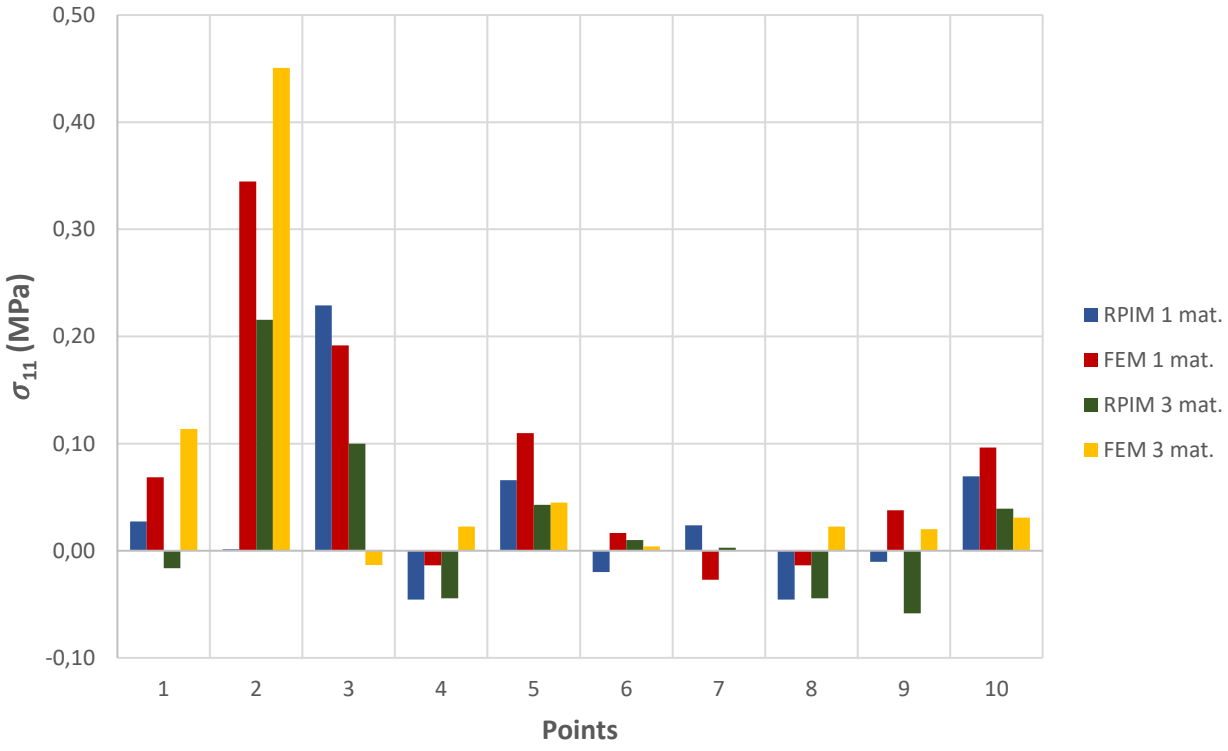

Figure 51 – Principal Stress σ_{11} comparison between FEM and RPIM, for both models (homogeneous material distribution and heterogeneous material distributing) [MPa].

Table 22 - Principal Stress component σ_{22} obtained with FEM and RPIM for both models (homogeneous material distribution and heterogeneous material distributing) [MPa].

		1	2	3	4	5	6	7	8	9	10
σ_{22}	**RPIM 1 mat**	-0,038	-0,373	0,059	-0,220	0,029	-0,095	-0,022	-0,220	-0,179	-0,016
	FEM 1 mat	-0,006	-0,249	0,046	-0,134	0,078	-0,045	-0,035	-0,134	-0,057	0,001
	RPIM 3 mat	-0,140	-0,168	0,030	-0,130	-0,031	-0,043	-0,030	-0,130	-0,120	-0,049
	FEM 3 mat	-0,039	-0,064	-0,069	-0,020	-0,018	-0,014	-0,025	-0,020	-0,001	-0,032

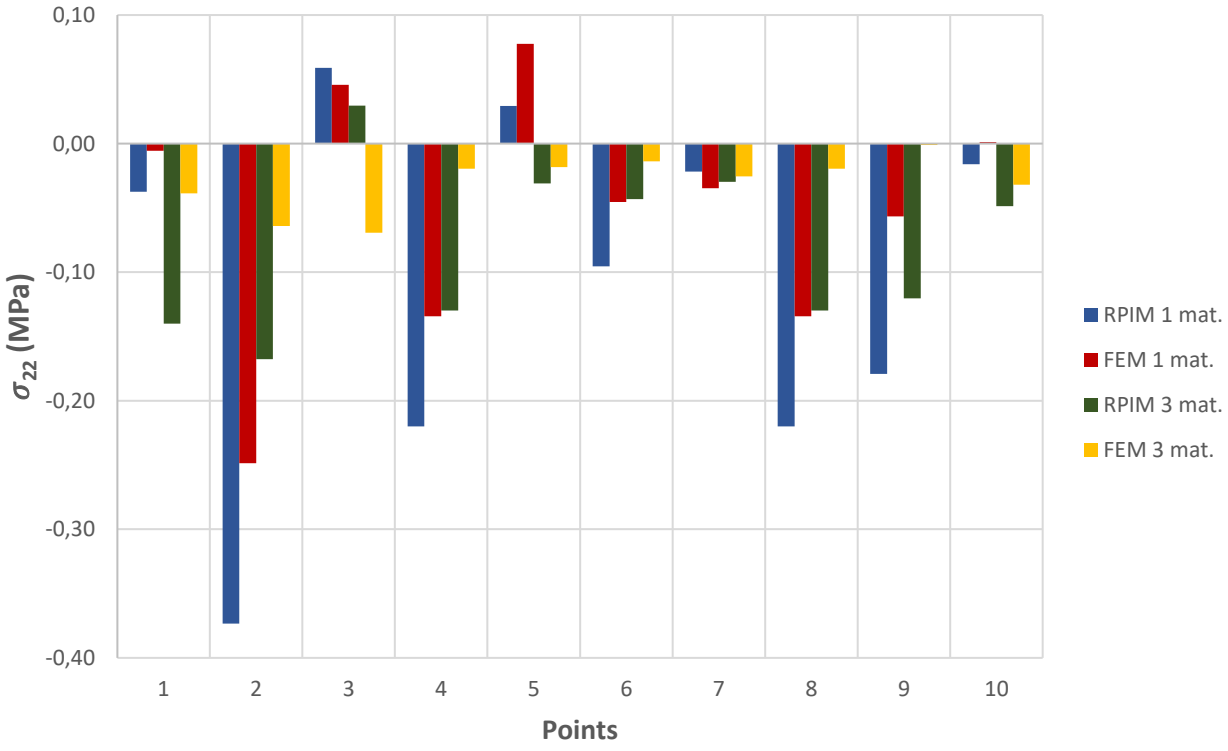

Figure 52 - Principal Stress σ_{22} comparison between FEM and RPIM, for both models (homogeneous material distribution and heterogeneous material distributing) [MPa].

Table 23 - Principal Stress component σ_{33} obtained with FEM and RPIM for both models (homogeneous material distribution and heterogeneous material distributing) [MPa].

		1	2	3	4	5	6	7	8	9	10
σ_{33}	**RPIM 1 mat**	-0,587	-1,946	-0,503	-1,421	-0,508	-1,833	-0,629	-1,421	-2,543	-0,707
	FEM 1 mat	-0,476	-1,378	-0,569	-1,249	-0,444	-1,680	-0,679	-1,249	-2,254	-0,650
	RPIM 3 mat	-0,625	-1,498	-0,538	-0,575	-0,368	-0,152	-0,121	-0,575	-0,447	-0,470
	FEM 3 mat	-0,530	-0,674	-2,414	-0,230	-0,262	-0,076	-0,117	-0,230	-0,110	-0,257

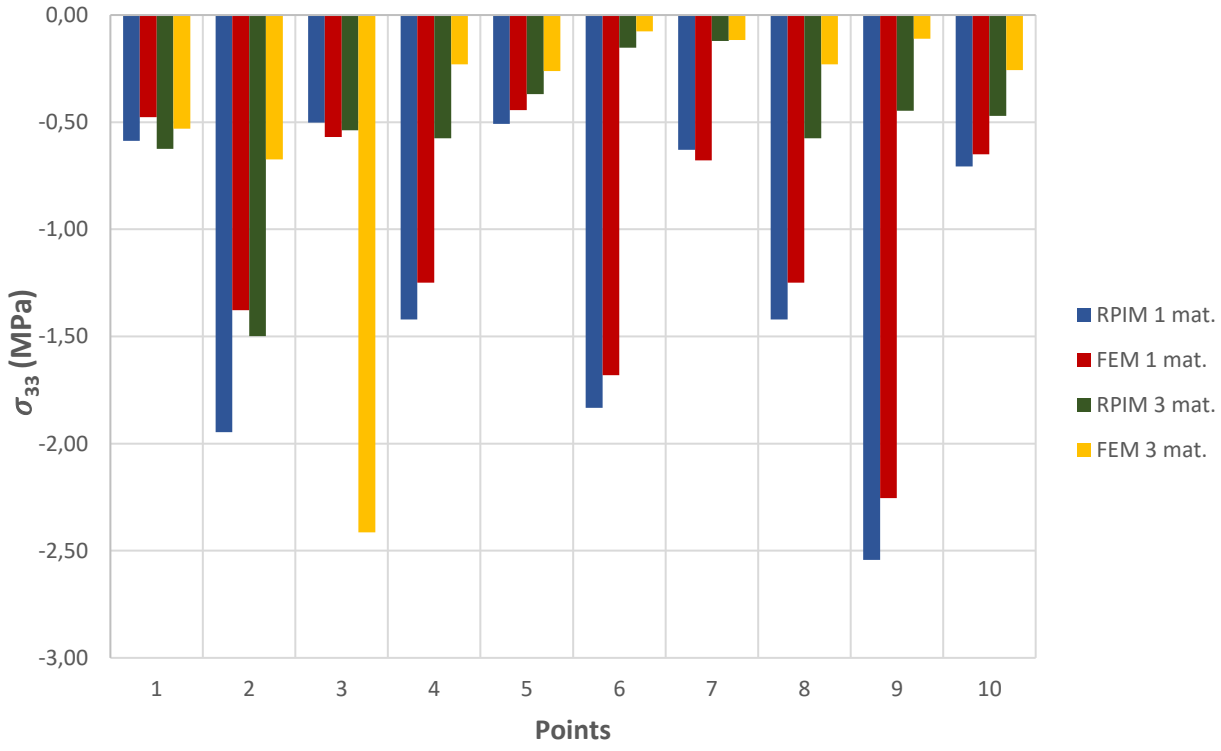

Figure 53 - Principal Stress σ_{33} comparison between FEM and RPIM, for both models (homogeneous material distribution and heterogeneous material distributing) [MPa].

From the graphics observation and considering the both models, some differences between FEM and RPIM results were found. The most significant difference was verified in Point 3, for the 3-material model, where the Effective Stress (or the principal stress component σ_{33}), obtained with FEM, is four times higher than the RPIM.

4.5 Osteotomy Cutting Lengths

As it was previously mentioned in **section 5.1**, a Linear-Elasto-Static analysis, evaluating the osteotomy itself, is conducted. The OWHTO geometry chosen is used to correct varus deformity of the knee, which is the most common problem in patients, and has the biplanar proximal cut of the tuberosity (in surgery, this cut is firstly performed). The osteotomy cutting itself starts at 40 mm from the tibial plateau and its pointed to the tip of the fibula which, in this case, corresponds to an approximate inclination of 23° (Figure 54-a). The other cut, is performed at 5 mm from the tuberosity limit. It is considered a thickness of 1mm, in the whole cut, with horizontal depths of 60, 65 and 70 mm.

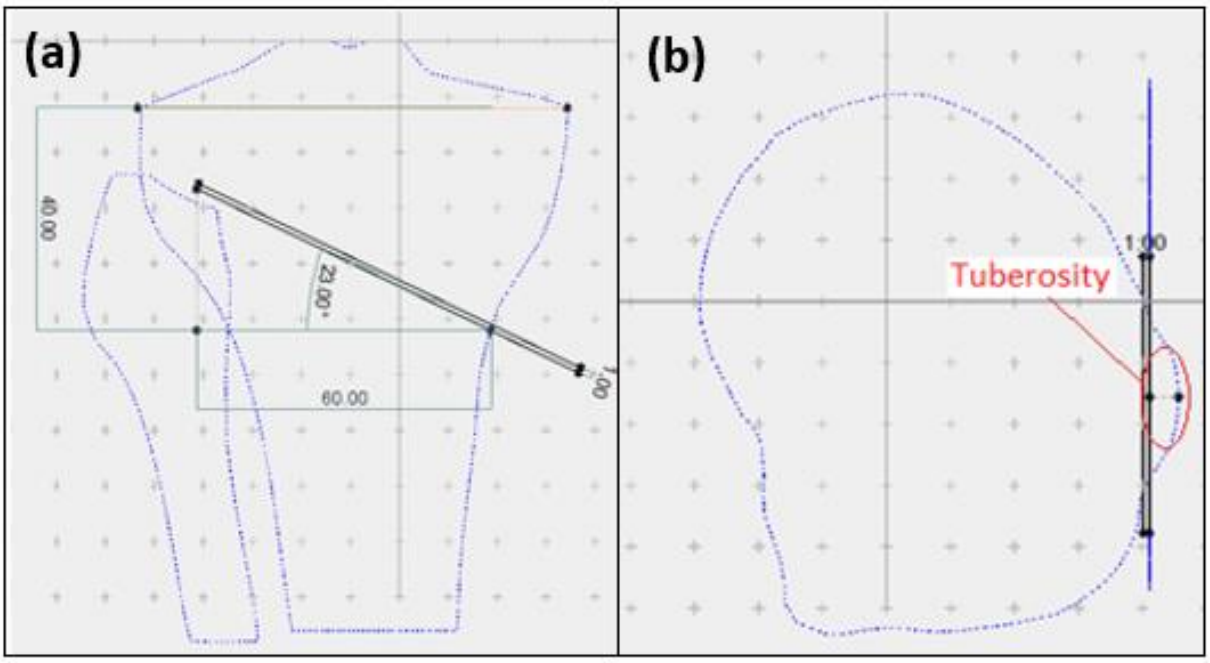

Figure 54 – Frontal (a) and transverse (b) sketches of the biplanar cutting geometry, used to create the osteotomy shape part.

The model with the osteotomy was performed in 3-MATIC®, subtracting the part with the desired cutting shape (with a constant thickness of 1 mm) and the previous meshed tibia (Figure 55-a, b). Then, the surface of the whole interior cut is remeshed, and the volume mesh is created with a total of 6739-6695 nodes (depending on the cutting length). Finally, the material assignment is performed and only the homogeneous option is considered, with the objective of having less computational effort.

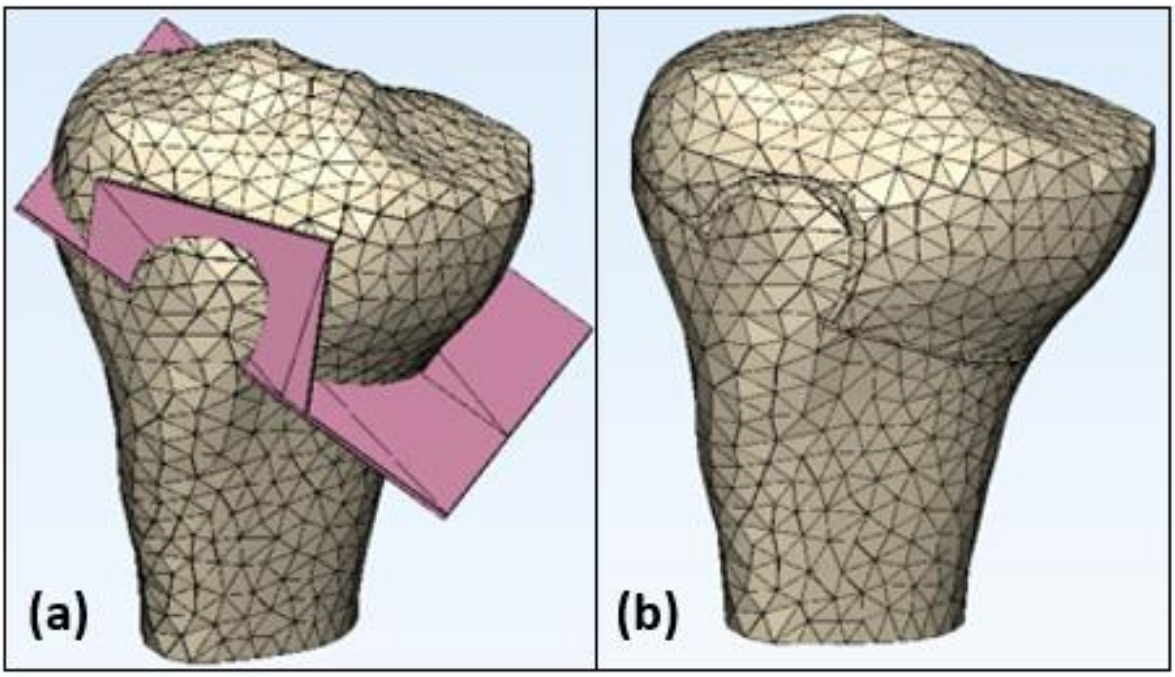

Figure 55 – (a) Tibial model with the cutting geometry object. (b) Tibial model after the subtraction between both parts.

The main objective of this model is to compare, again, the FEM and RPIM results of the Effective and Principal Stress components for the different osteotomy lengths. Another objective is to evaluate the obtained Stress values, comparing the influence when applying different displacements, 10 and 15mm (**section 4.5.1**). Finally, the osteotomy with a circular hinge will also be evaluated, in terms of stress (**section 4.5.2**).

Three integration points were picked: two belonging to elements at the hinge – **points 1** and **2**, and another point outside, but near, the hinge – **point 3**. As essential boundary condition, displacements of 10 and 15 mm are applied at four entrance points of the osteotomy, corresponding to the real tibial opening, during surgery, with the Osteotome (opening tool). All the bottom "base" points of the tibia are fixed (null displacement in every direction).

For the RPIM numeric simulation, an extra step is required. Since the osteotomy cut is really narrow (1 mm thickness), if a Boolean operation is not considered, the meshless formulation will consider (by definition) the nodes on the top of the cut plane and the nodes of the bottom part of the cut plane as part of the same domain, considering it as "continuous material". Thus, the meshless formulation will naturally disregard the cut.

Thus, a programming routine was created to solve this problem (**Annex A-3**), dividing the tibial model in 3 different groups. The plane is defined using points A, B and C. Point A is located at the hinge and points B and C are located at the beginning of the cut (Figure 56). From their coordinates, vectors $\vec{v}_{AB}$ and $\vec{v}_{AC}$ are determined (difference between coordinates), and both define a plane $\propto$. The normal of this plane is calculated with the cross product between both vectors and its corresponding unit norm (equation (63)), and the scalar equation of the cutting plane is written (64):

$$\boldsymbol{n} = \boldsymbol{v_{AB}} \times \boldsymbol{v_{Ac}} \quad ; \quad \boldsymbol{u}_n = \frac{1}{\|\boldsymbol{n}\|} \cdot \boldsymbol{n} \tag{63}$$

$$\text{Scalar equation of } Plane \propto: \; u_n^x \cdot x + u_n^y \cdot y + u_n^z \cdot z = D_\propto \tag{64}$$

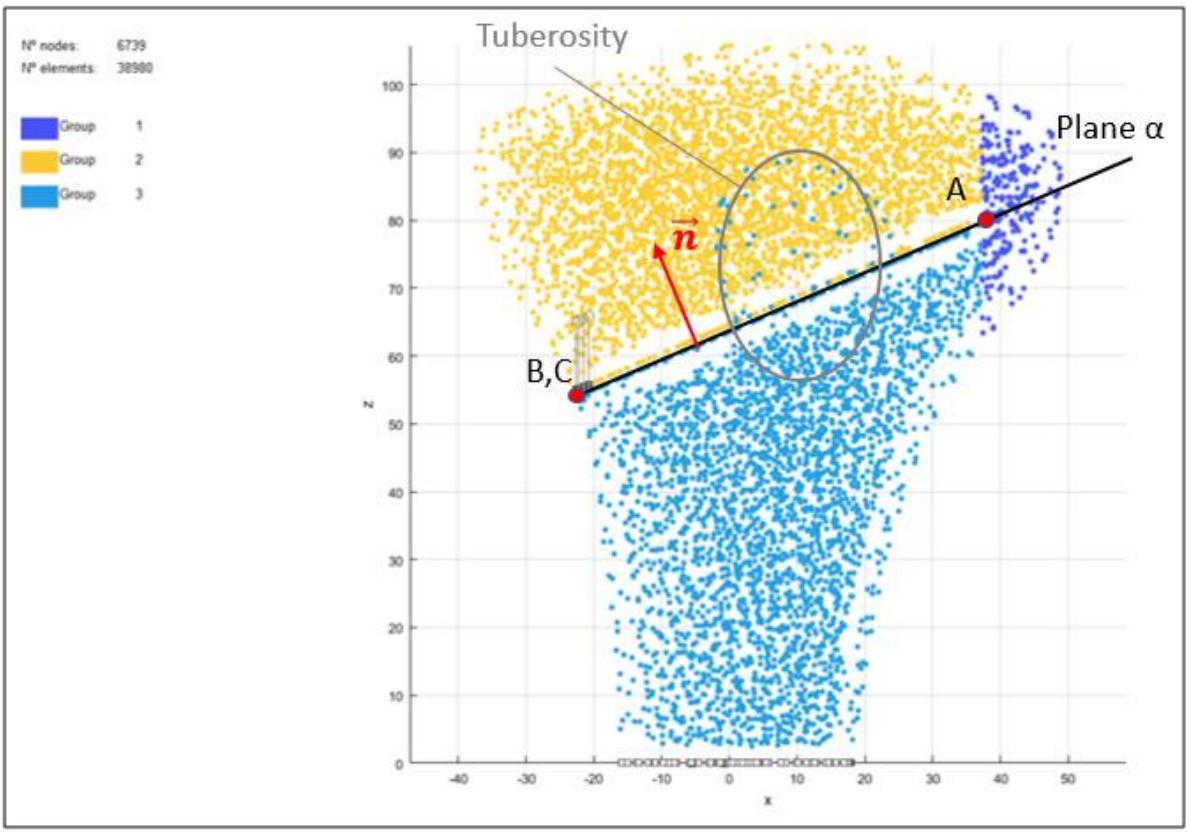

Figure 56 - Group assignment utilized for RPIM.

The first group selecting condition (Figure 57), separates the whole model in Group 2 and 3, above and below the cut respectively, by calculating the planar constant D, for every node, and comparing its value with the value of $D_{\propto}$. There is a condition to place the tuberosity at group 3, because, when the osteotomy is performed, the tuberosity still needs to remain at the initial position (not causing major differences in the patellar ligament length). Finally, the nodes at the right of the hinge are placed in group 1 using the *xx* coordinate of point A.

The Boolean conditions states that:

- nodes belonging to Group 1 can only interact with nodes belonging to Group 1, 2 and 3.

- nodes belonging to Group 2 can only interact with nodes belonging to Group 1 and 2.

- nodes belonging to Group 3 can only interact with nodes belonging to Group 1 and 3.

Thus, nodes belonging to Group 2 will not interact with nodes belonging to Group 3, which will allow to separate the nodes on the top of the cut plane from the nodes of the bottom part of the cut plane. Therefore, for example, an interest point belonging to Group 2 will have inside its influence domain only nodes belonging to Group 1 or Group 2, inducing the intended material discontinuity.

```
% Conditions plane alfa
if D_ii < D_alf
    x_val(2,ii) = 2; % group 2
else
    x_val(2,ii) = 3; % group 3
end

% conditon of the tuberosity
if y_ii < E(2,1)
    x_val(2,ii) = 3; % group 3
end

% right side
if x_ii > A(1,1)
    x_val(2,ii) = 1; % group 1
end
```

Figure 57 – Programming routine section (Annex A-3), with all group selection conditions.

4.5.1 Osteotomy with a 10mm displacement

First, it is analysed the effects of enforcing a 10mm opening for distinct cutting lengths. The results obtained from FEM and RPIM, for the different cutting lengths, are presented in the following tables and figures.

Table 24 – Effective and main stress components, from the homogeneous tibial model with a 10mm opening and a 60mm cutting length, obtained with FEM. Also, there's the mean effective model stress [MPa].

Points	**1**	**2**	**3**	**Mean σ_{ef}**
[x; y; z]	[37,71; -32,87; 80,02]	[37,56; -9,16; 80,10]	[44,42; 3,22; 73,87]	
σ_{ef}	345,04	185,66	68,97	11,96
σ_1	468,34	230,77	22,13	
σ_2	161,04	70,50	-6,84	
σ_3	95,09	27,33	-56,61	

Table 25 - Effective and main stress components, from the homogeneous tibial model with a 10mm opening and a 60mm cutting length, obtained with RPIM. Also, there's the mean effective model stress [MPa].

Points	**1**	**2**	**3**	**Mean σ_{ef}**
[x; y; z]	[37,71; -32,87; 80,02]	[37,56; -9,16; 80,10]	[44,42; 3,22; 73,87]	
σ_{ef}	49,33	27,18	52,52	10,11
σ_1	21,47	42,04	-1,41	
σ_2	-14,08	17,63	-7,34	
σ_3	-34,84	12,75	-56,64	

Table 26 - Effective and main stress components, from the homogeneous tibial model with a 10mm opening and a 65mm cutting length, obtained with FEM. Also, there's the mean effective model stress [MPa].

Points	**1**	**2**	**3**	**Mean σ_{ef}**
[x; y; z]	[42,32; -28,72; 81,56]	[42,81; -9,58; 82,06]	[44,42; 3,22; 73,87]	
σ_{ef}	496,60	84,40	56,14	10,40
σ_1	572,49	152,77	4,37	
σ_2	177,29	74,97	-12,12	
σ_3	15,07	63,04	-58,16	

Table 27 - Effective and main stress components, from the homogeneous tibial model with a 10mm opening and a 65mm cutting length, obtained with RPIM. Also, there's the mean effective model stress [MPa].

Points	**1**	**2**	**3**	**Mean σ_{ef}**
[x; y; z]	[42,32; -28,72; 81,56]	[42,81; -9,58; 82,06]	[44,42; 3,22; 73,87]	
σ_{ef}	49,42	51,27	52,32	9,15
σ_1	51,44	66,06	-9,38	
σ_2	10,24	16,98	-19,97	
σ_3	-3,35	12,86	-66,19	

Table 28 - Effective and main stress components, from the homogeneous tibial model with a 10mm opening and a 70mm cutting length, obtained with FEM. Also, there's the mean effective model stress [MPa].

Points	**1**	**2**	**3**	**Mean σ_{ef}**
[x; y; z]	[47,37; -16,70; 83,61]	[47,42; -9,92; 84,21]	[44,42; 3,22; 73,87]	
σ_{ef}	4003,10	306,48	24,70	9,58
σ_1	4968,80	381,70	-9,08	
σ_2	1656,80	127,86	-13,56	
σ_3	520,30	41,23	-35,71	

Table 29 - Effective and main stress components, from the homogeneous tibial model with a 10mm opening and a 70mm cutting length, obtained with RPIM. Also, there's the mean effective model stress [MPa].

Points	**1**	**2**	**3**	**Mean σ_{ef}**
[x; y; z]	[47,37; -16,70; 83,61]	[47,42; -9,92; 84,21]	[44,42; 3,22; 73,87]	
σ_{ef}	137.36	37,49	26,20	7,97
σ_1	135.96	-3,72	8,10	
σ_2	18.49	-15,59	2,59	
σ_3	-15.08	-45,70	-20,42	

The point 1 revealed to be a very unstable hinge point since its stress values were very high, becoming a very unpredictable point, for the present evaluation. Points 2, inside hinge, and 3, outside hinge, were evaluated and both numeric methods were graphically compared in the following Figures 58, 59, 60 and 61.

The Principal and the Effective Stress values in point 2 are very different when differing the numeric method. This can be explained by the fact that this point is a hinge point, and an unstable one. In the contrary, in point 3, no relevant difference between both methods was revealed.

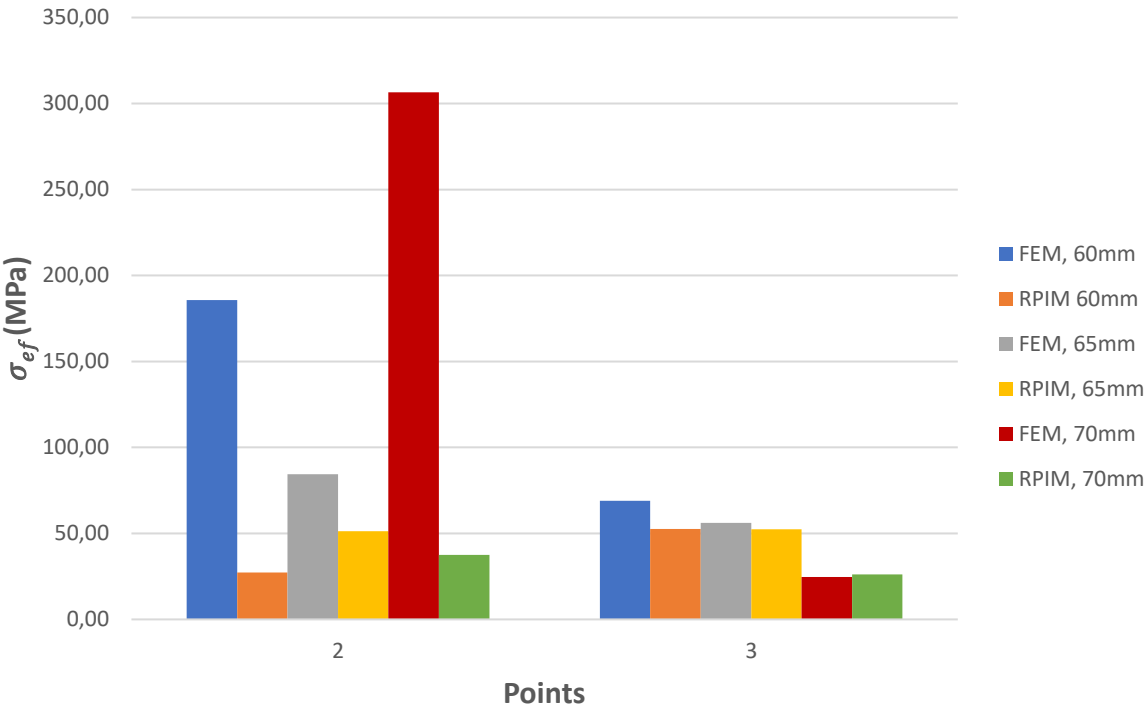

Figure 58 - Effective Stress comparison between FEM and RPIM, for the different cutting lengths.

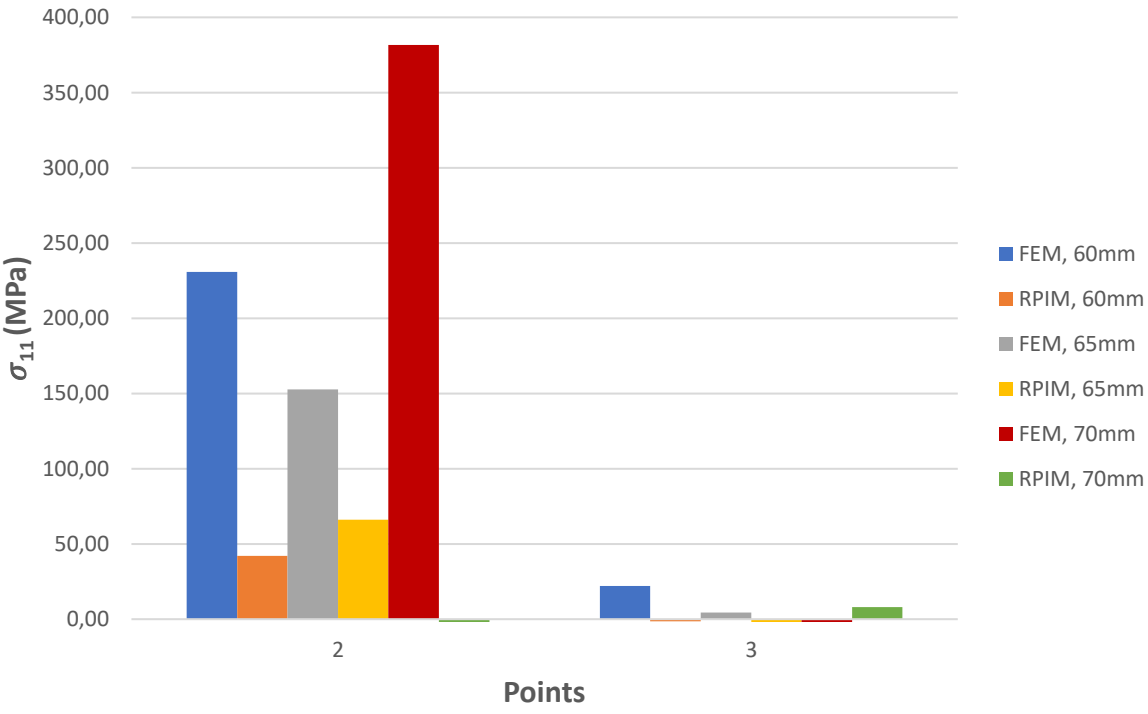

Figure 59 - Main Stress - σ_{11} comparison between FEM and RPIM, for the different cutting lengths.

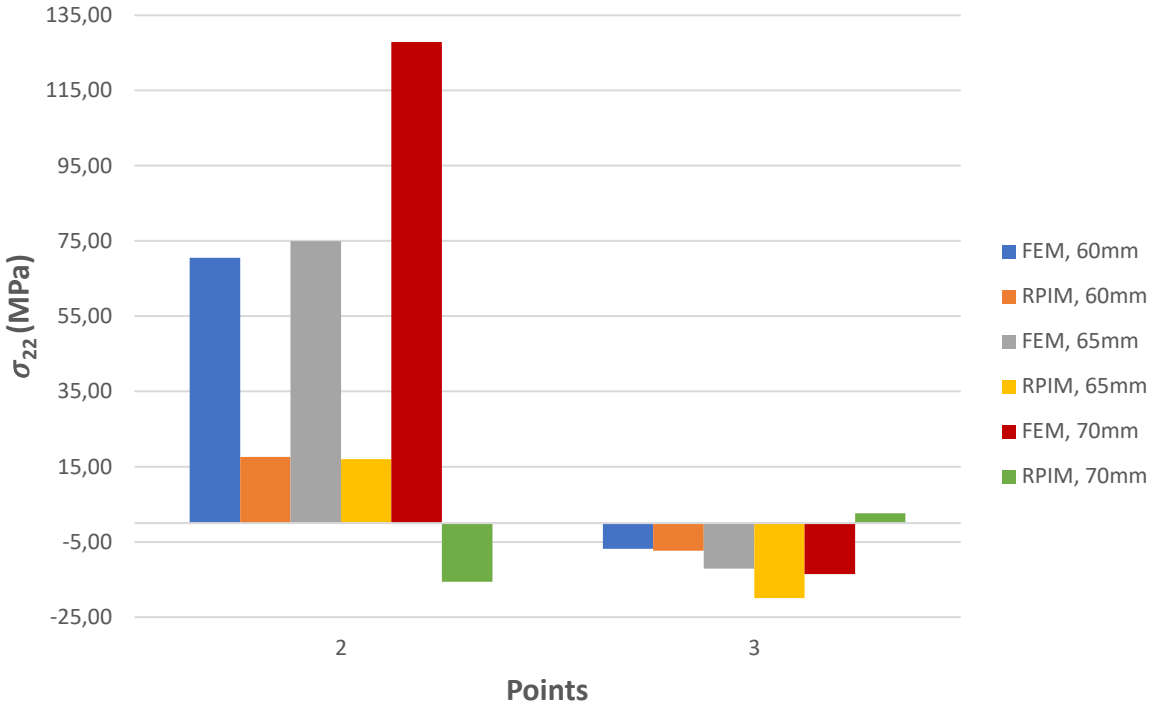

Figure 60 - Main Stress - σ_{22} comparison between FEM and RPIM, for the different cutting lengths.

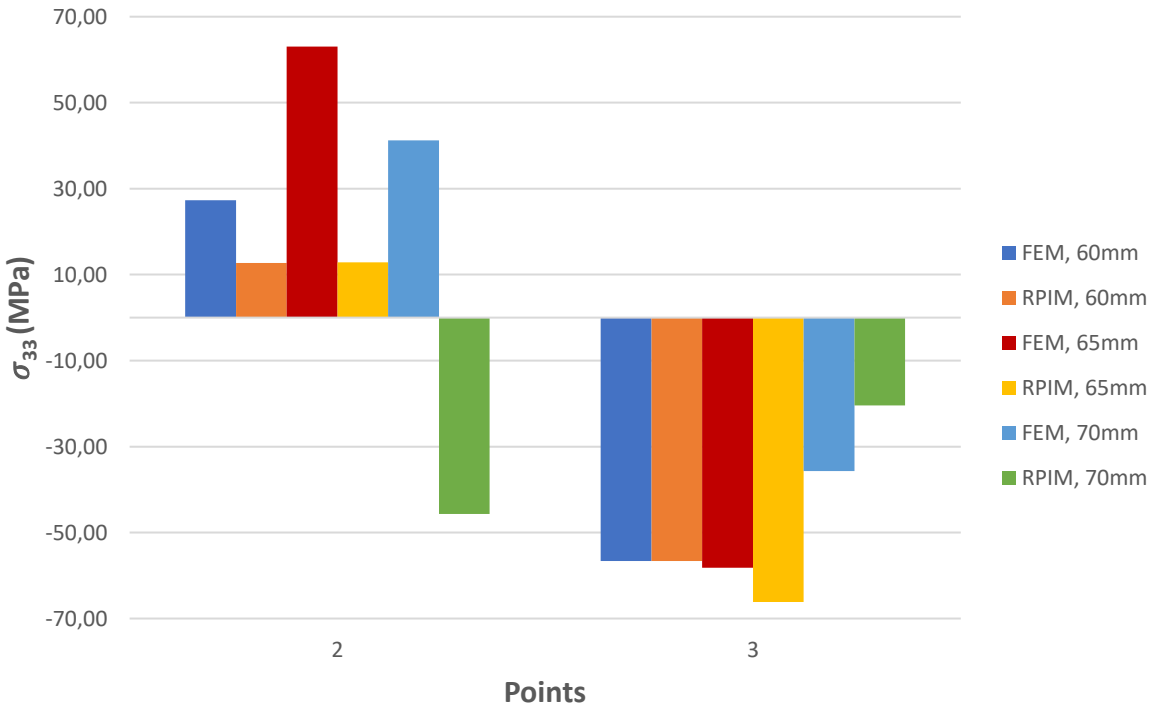

Figure 61 - Main Stress - σ_{33} comparison between FEM and RPIM, for the different cutting lengths.

4.5.2. Osteotomy with a 15mm displacement

In this section, it is only pretended a comparison between two different displacements, varying the cutting length, only using FEM. From 10 to 15 mm, the mean effective stress grows

approximately 5.36 MPa (mean value for the different cutting lengths). This value was expected because a higher opening of the osteotomy leads to a higher level of the overall model stress.

Concerning the three-points evaluation, there are lower values of effective stress on point 3 (outside the hinge) comparing to the 10mm displacement model at the same point. In the contrary, in points 1 and 2, their stress values become higher, meaning that the stress gets more concentrated at the hinge, leaving the points outside the hinge with lower stress values. Only points 2 and 3 are graphically represented because point 1 is an unstable hinge point, reaching exaggerated maximum stress values.

Table 30 - Effective and main stress components, from the homogeneous tibial model with a 15mm opening and a 60mm cutting length, obtained with FEM. Also, there's the mean effective model stress [MPa].

Points	**1**	**2**	**3**	**Mean σ_{ef}**
[x; y; z]	[37,71; -32,87; 80,02]	[37,56; -9,16; 80,10]	[44,42; 3,22; 73,87]	
σ_{ef}	517,56	196,7228	17,55	
σ_1	702,51	304,21	2,38	17,94
σ_2	-32,87	120,43	-0,83	
σ_3	80,02	96,69	-16,55	

Table 31 - Effective and main stress components, from the homogeneous tibial model with a 15mm opening and a 65mm cutting length, obtained with FEM. Also, there's the mean effective model stress [MPa].

Points	**1**	**2**	**3**	**Mean σ_{ef}**
[x; y; z]	[42,32; -28,72; 81,56]	[42,81; -9,58; 82,06]	[44,42; 3,22; 73,87]	
σ_{ef}	744,89	126,60	21,13	
σ_1	858,73	229,15	19,30	15,56
σ_2	265,93	112,45	-0,46	
σ_3	22,61	94,56	-2,98	

Table 32 - Effective and main stress components, from the homogeneous tibial model with a 15mm opening and a 70mm cutting length, obtained with FEM. Also, there's the mean effective model stress [MPa].

Points	**1**	**2**	**3**	**Mean σ_{ef}**
[x; y; z]	[47,37; -16,70; 83,61]	[47,42; -9,92; 84,21]	[44,42; 3,22; 73,87]	
σ_{ef}	6004,60	459,72	2,60	
σ_1	7453,10	572,55	2,01	14,51
σ_2	2485,20	191,80	-0,19	
σ_3	780,40	61,84	-0,85	

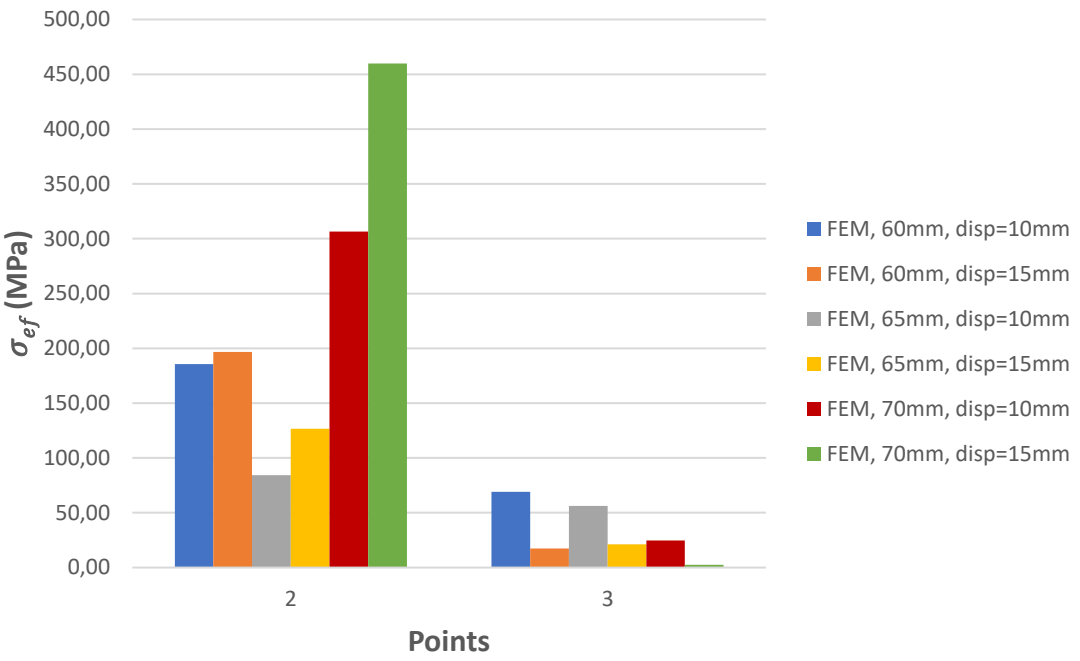

Figure 62 - Effective Stress comparison, for the different cutting lengths and for different displacements (10mm and 15mm), using FEM.

4.5.3. Osteotomy with circular hinge

HTO is performed by a partial cutting with a bone saw from medial to lateral, leaving the lateral cortex intact serving as a bone bridge and a hinge point during osteotomy opening. So, the intra-operative prevention of contralateral cortex fracture during the procedure is essential to avoid an unstable postoperative situation with lack of primary stability. (Arthrex 2016)

The *Arthrex Department of Research* conducted experimental tests and a finite element analysis comparing the stress behaviour of having a sharp cutting edge versus a drill hole (circular hinge) at the end of the same planar cut. It was proven that the hinge pin technique allows more 60.5% gap opening level (until fracture) and a maximum effective stress reduction of 43% for a 10mm opening gap. This technique reduces drastically the risk of lateral cortex fracture by stress homogenization in the area of the drill hole, avoiding earlier crack initiation and possible fracture. (Arthrex 2016)

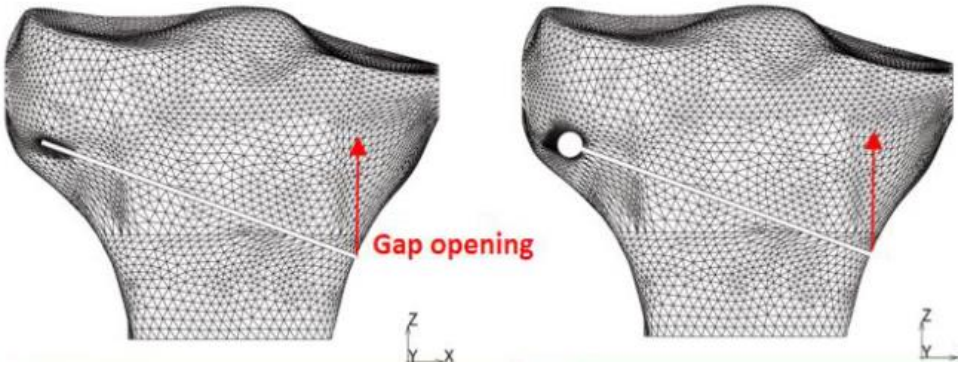

Figure 63 - Arthrex FEA implementation with a translation vector applied along the z-axis on the medial cortex and leaving 10 mm bone bridge intact. (Arthrex 2016)

To prove the same idea from Arthrex, a similar model was created with a cutting length of 60 mm and a hinge pin hole with 6 mm of diameter (Figure 64-a) and a Linear-Elasto-Static

analysis, using FEM, was made (Figure 64-b). The results are compared with the previous model, for the same cutting length.

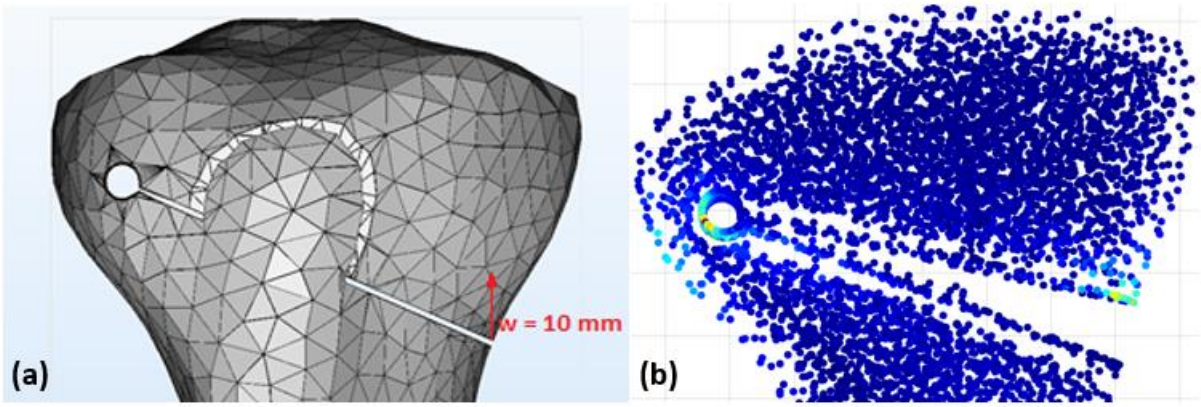

Figure 64 – (a) Model build, in FEMAS, with 6 mm hinge pin hole in 3-MATIC® and with a 10mm vertical displacement (zz axis direction) applied. (b) Plot with the effective stress results, showing all the deformed points, obtained with FEM.

The maximum effective stress value in the circular hinge is 240.87 MPa (point 1), which corresponds to a 30.2% stress reduction (previous maximum effective stress value was 345.04 MPa). For the point located outside the hinge (same as the previous 60 mm model), the value decreased from 68.87 to 45.11 MPa, equivalent to a 34.5% reduction. The mean effective stress of the model also decreased from 11.96 to 10.77 MPa.

The maximum point stress reduction was not as high as the value obtained from Arthrex (30% instead of 43%) but it validates their conclusion, that this technique decreases significantly the maximum effective stress values by homogenization of the area around the hinge pin hole, preventing crack initiation and lateral cortex fracture. The effective stress reduction between the previous hinge and the circular hinge is evident in Figure 65.

The results obtained for the effective and main stresses are written in the following table:

Table 33 - Results obtained with FEM for the 6mm hinge pin hole tibial model [MPa].

Points	**1**	**2**	**3**	**Mean**
[x; y; z]	[40,47; -31,52;79,17]	[37,56; -21,71; 85,36]	[44,42; 3,22; 73,87]	
σ_{ef}	240,87	52,86	45,113	
σ_1	49,44	4,56	48,5732	10,77
σ_2	-57,73	-18,08	7,4606	
σ_3	-226,41	-55,85	0,3131	

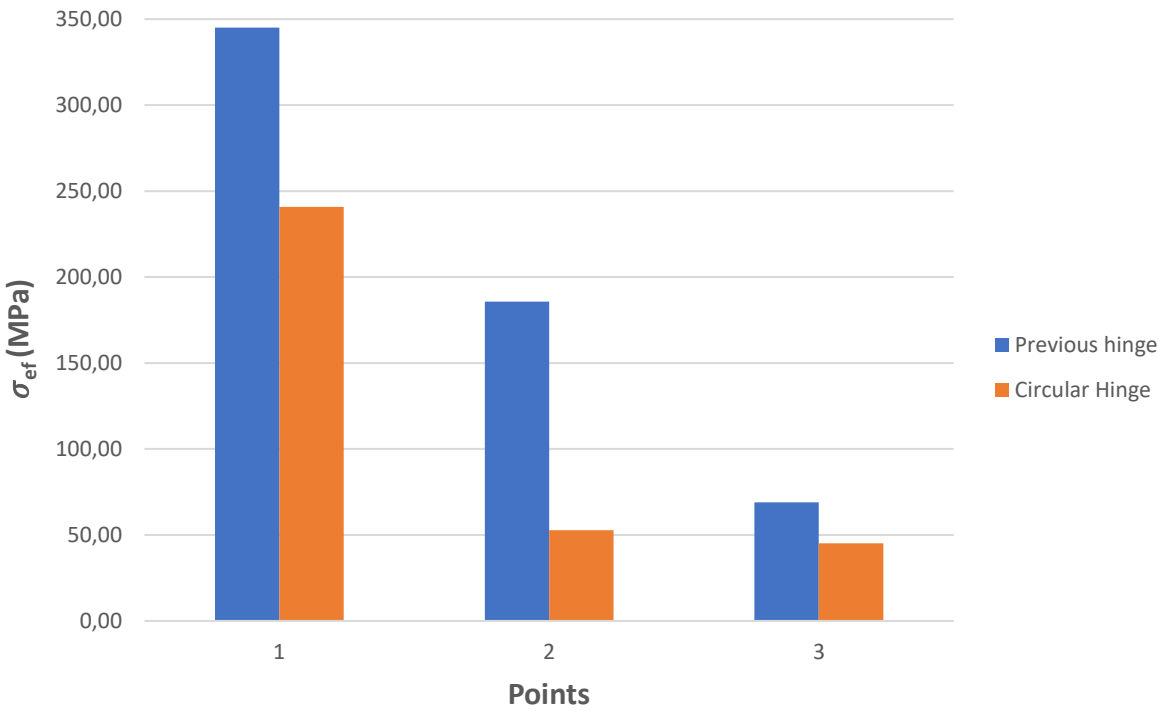

Figure 65 – Effective stress comparison between the previous hinge with the circular hinge hole, at the three points.

4.6 Prosthesis comparison and design choice

In (Raja Izaham et al. 2012) a comparison between TomoFix™ and Puddu (the two most commonly used plates) was made using a Finite Element Analysis. It was demonstrated that the TomoFix™ plate underwent higher amount of Equivalent von Mises stress (maximum σ_{ef} =262.47 MPa) which is explained by the fact that this plate uses a locking fixation, providing better anchorage and a more rigid angular stability than Puddu's plate, thereby displacing the stresses transmitted by the body weight. In clinical application, this may be a disadvantage as the stress shielding effect may cause severe osteoporosis in the long term. For the Puddu plate, the micromotion was greater (14 μm higher) and it was expected to be much higher during normal physiological cyclic loading. Excessive displacement of the bone, such as bending and torsion of the bone fragment relative to the distal bone, may result in failure or loosening of the implant. In conclusion, the higher rigidity and stability of the TomoFix™ implant in this study appears to be compensated with the loss of micromotion (which may also lead to the possibility of non-union and failure of fracture fixation when the micromotion becomes greater).

In (Stoffel, Stachowiak, and Kuster 2004) an experimental study evaluated the axial compression stiffness and the torsional rigidity of the Puddu and TomoFix™ plates showing that both plates were able to maintain the correction for a load of more than 2500 N (2537 and 2904 N for Puddu and TomoFix™ respectively), which is close to the axial compressive load in the knee of a normal adult during single limb of fast walking. After the osteotomy and fixation with the Puddu Plate a 76% reduction in axial stiffness, and 41% in torsional rigidity was observed compared to the intact bone. For the TomoFix™ Plate the reduction was 69% and 28%. The relevant advantage of the TomoFix™ plate over the Puddu plate happens if the lateral cortex is injured (fractured or displaced), which provides higher stability in both compression and torsion.

Another relevant variant of the titanium TomoFix™ plate was the PEEKPower HTO-Plate® from Arthrex®, made of a Carbon-fibre and PEEK composite. The following has several advantages for valgus-producing open-wedge HTO, such as angle-stable multidirectional fixation, radiolucency, and a less bulky design. However, the first-generation PEEKPower® plate provided a higher rate of implant-related complications (inflammation or tissue necrosis) compared to the TomoFix™ plate at a minimum follow-up of 24 months after surgery. Also, because of its locking concept, abrasion of the material commonly occurred during fixation. Therefore, it is not recommended to use the first-generation PEEKPower HTO-Plate® in the clinical practice. (Cotic et al. 2014)

For the previously mentioned literature, TomoFix™ is the currently gold standard. (Cotic et al. 2014)(Raja Izaham et al. 2012)(Stoffel, Stachowiak, and Kuster 2004) Not only provides great overall rigidity and stability, but also combines biomechanical properties that are held accountable for fast bone healing: (1) high primary fixation stability; (2) a compliant bone-implant system which allows some residual micromotion within the osteotomy gap to promote a "*callus massage*". (Diffo Kaze et al. 2015)

However, in (Diffo Kaze et al. 2015), static compression load-to-failure and load-controlled cyclic fatigue-to-failure tests were performed, comparing the biomechanical properties of the recent iBalance®, PEEKPower® and Contour Lock from Arthrex®, with the golden standard and small sized TomoFix™ plates.

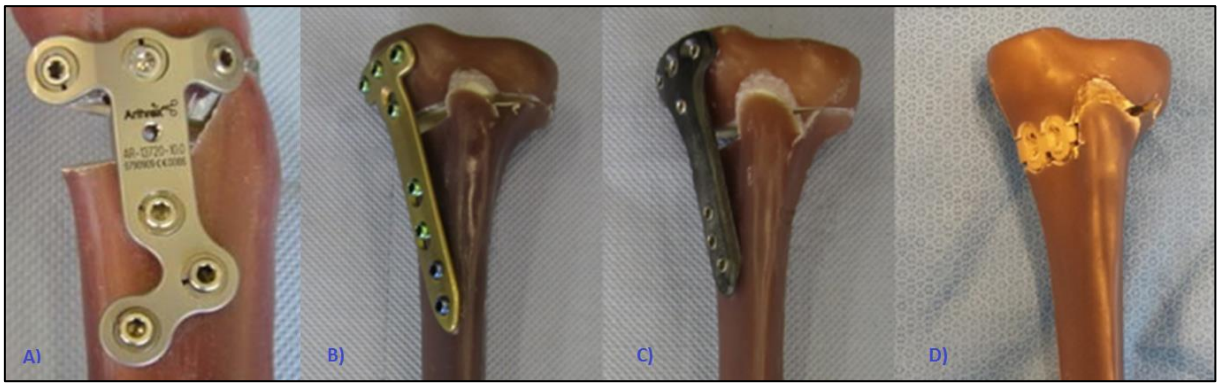

Figure 66 - A) ContourLock®; B) TomoFixTM Std; C) PEEKPower®; D) iBalance®.(Diffo Kaze et al. 2015)

The key findings of the present study were the following: (1) The stiffest bone-implant system was found to be the iBalance® followed by the ContourLock® plate. (2) The ContourLock® plate provided highest fatigue strength under cyclic loading conditions. (3) Static loading until failure tests revealed superior strength for the iBalance® implant followed by the TomoFix™ standard, the PEEKPower®, the ContourLock® and the small sized TomoFix™. (4) All implants withstood the maximal physiological vertical tibiofemoral contact force while slow-walking, which is three times the body weight (e.g. 2400 N for 80 kg).

So, there are great and more viable solutions (ContourLock® and iBalance), than the golden standard TomoFix™ plate. (Diffo Kaze et al. 2015) The tibial model that was available for this work, from MIMICS®, was not adequate, in terms of length, to be used with the TomoFix™ plate, otherwise its evaluation and comparison would have been very pertinent due to the fact that its static loading strength is said to be superior to all other implants (figure 34).

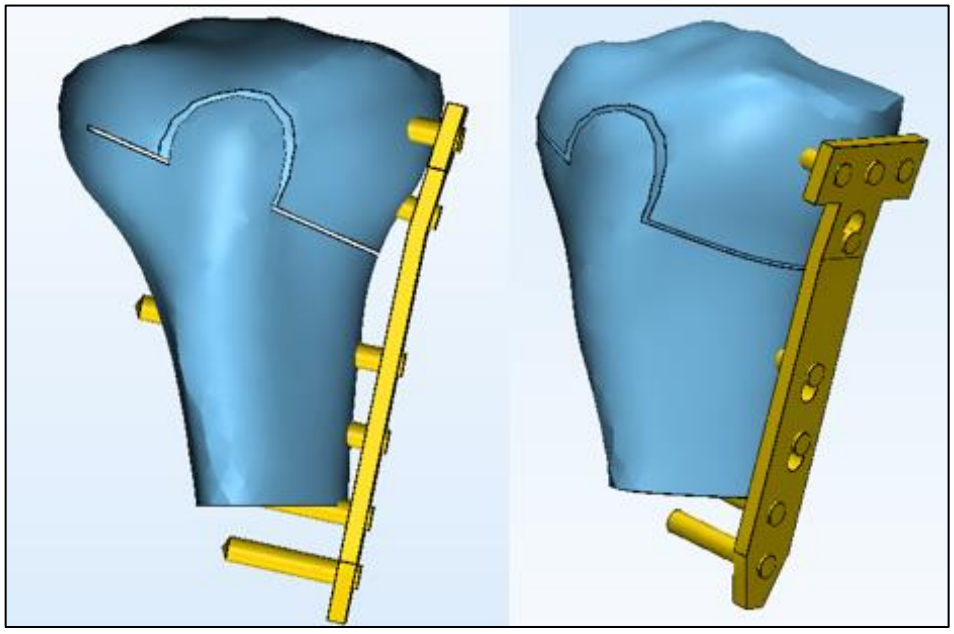

Figure 67 – Current tibial model with the standard TomoFix™ implant positioned.

Based in all the arguments above, the present work solution of creating a new fixation implant will follow some of the ContourLock® design which is, so far, the best metallic plate in terms of bone-implant system stiffness and fatigue strength, differentiating the number of the fixation holes. Also, another design, with a reduced volume of required material and a different hole configuration, will be explored in the next section.

4.7 Bone-Implant model construction

A study conducted by Weng et al. utilizing the TomoFix™ plate, revealed that a pre-contoured plate is recommended in the case that the proximal tibia is highly concave (like the one used in this work) and the distraction angle or opening height is insufficient to stretch the tibial profile. The preoperative estimation of the gap between plate and bone becomes essential in order to avoid the risk of lateral cortex fracturing and gap changes in the distracted wedge. (Weng et al. 2017)

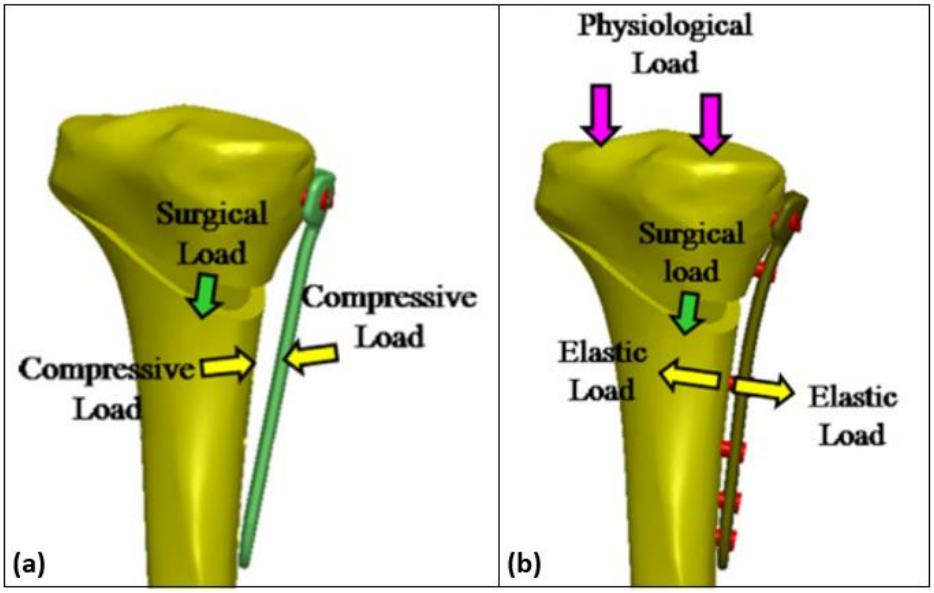

Figure 68 – Studied scenarios by Weng et al with a TomoFix™ plate: (a) Intraoperative scenario: The compressive load causes the quasi-straight plate to fit the proximal tibia; (b) Postoperative scenario: The elastic load is applied to the contoured plate to simulate the plate spring back. (Weng et al. 2017)

Following the previous conclusion, all the implants will be designed with a slight pre-contoured shape for better adaptation to the tibial shape, becoming a more anatomical plate and reducing the bone-plate gap, important for the intraoperative (Figure 68-a) and postoperative (Figure 68-b) scenarios. This way, the spring and compressive forces, usually caused by a straight implant, can be ignored in the definition of the natural boundary conditions.

A total of four models will be constructed for the structural analysis.

4.7.1 Final Models

Model 1 (Figure 69**Erro! A origem da referência não foi encontrada.**-a) is the ContourLock® plate with all six screws: Three Cortical Screws Ø6.5x70mm, and Three Distal Screws Ø4.5x40mm. **Model 2** (Figure 69-b) is also the ContourLock® plate with five screws: Three Cortical Screws Ø6.5x70mm and two Distal Screws Ø4.5x40mm.

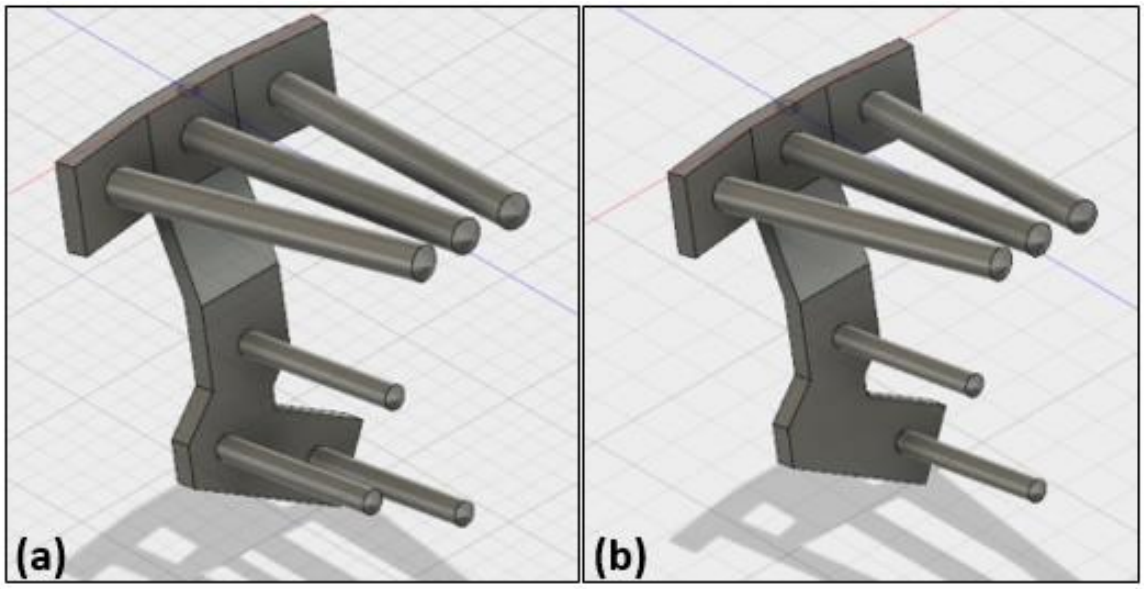

Figure 69 - (a) Model 1 ;(b) Model 2.

The next models follow the same design as the previous plate, but has a different distal configuration, reducing the required volume of material and adding a new position for the Distal Screws. This implant was created by the thesis' Autor.

The difference between **Model 3** (Figure 70-a) and **Model 4** (Figure 70-b) is the number of the Distal Screws: Model 3 has three Ø4.5x40mm Distal Screws while Model 4 has only two. The three Cortical Screws Ø6.5x70mm are equally used in both models.

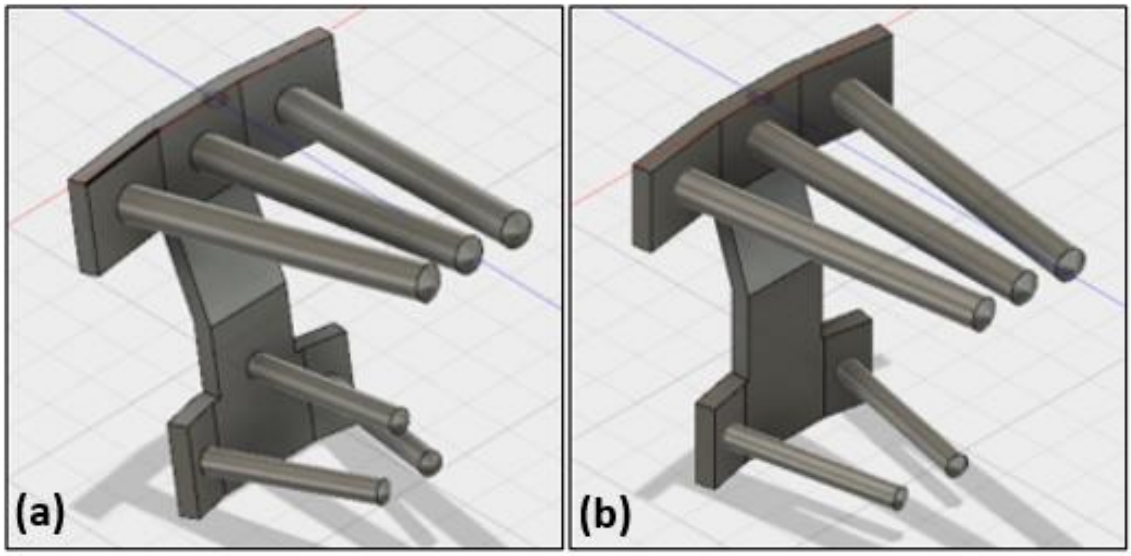

Figure 70 - (a) Model 3; (b) Model 4.

The two different implants were designed in Fusion360®, using an imported sketch of the tibial frontal contour (exported from the original model). Figure 71 and Figure 72 are Technical Drawings of both plates, with their respective volume. The first plate has around 8572 mm^3 and the second has 8401mm^3. Afterwards, the plates were imported in *STL* file to 3-MATIC® for its right positioning, applying some Remeshing Operations (non-assembly manifold, Meshing, etc.) and for the volumes creation. The material properties are assigned in MIMICS® and, finally, the *INP* file is obtained. It will be considered a tibial osteotomy length of 65 mm.

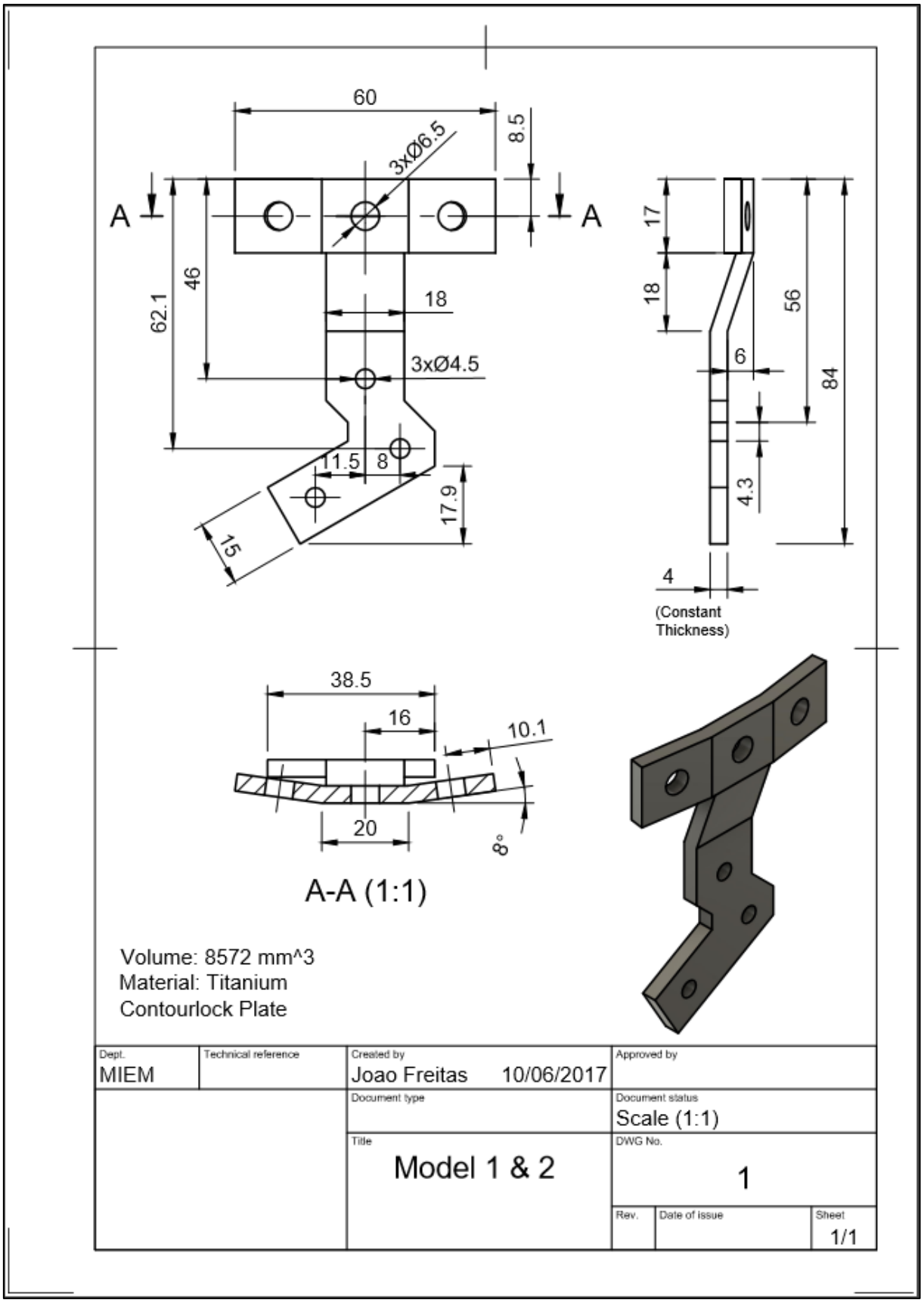

Figure 71 - Technical Drawing (Fusion360) of the CountorLock plate, used in Model 1 and Model 2.

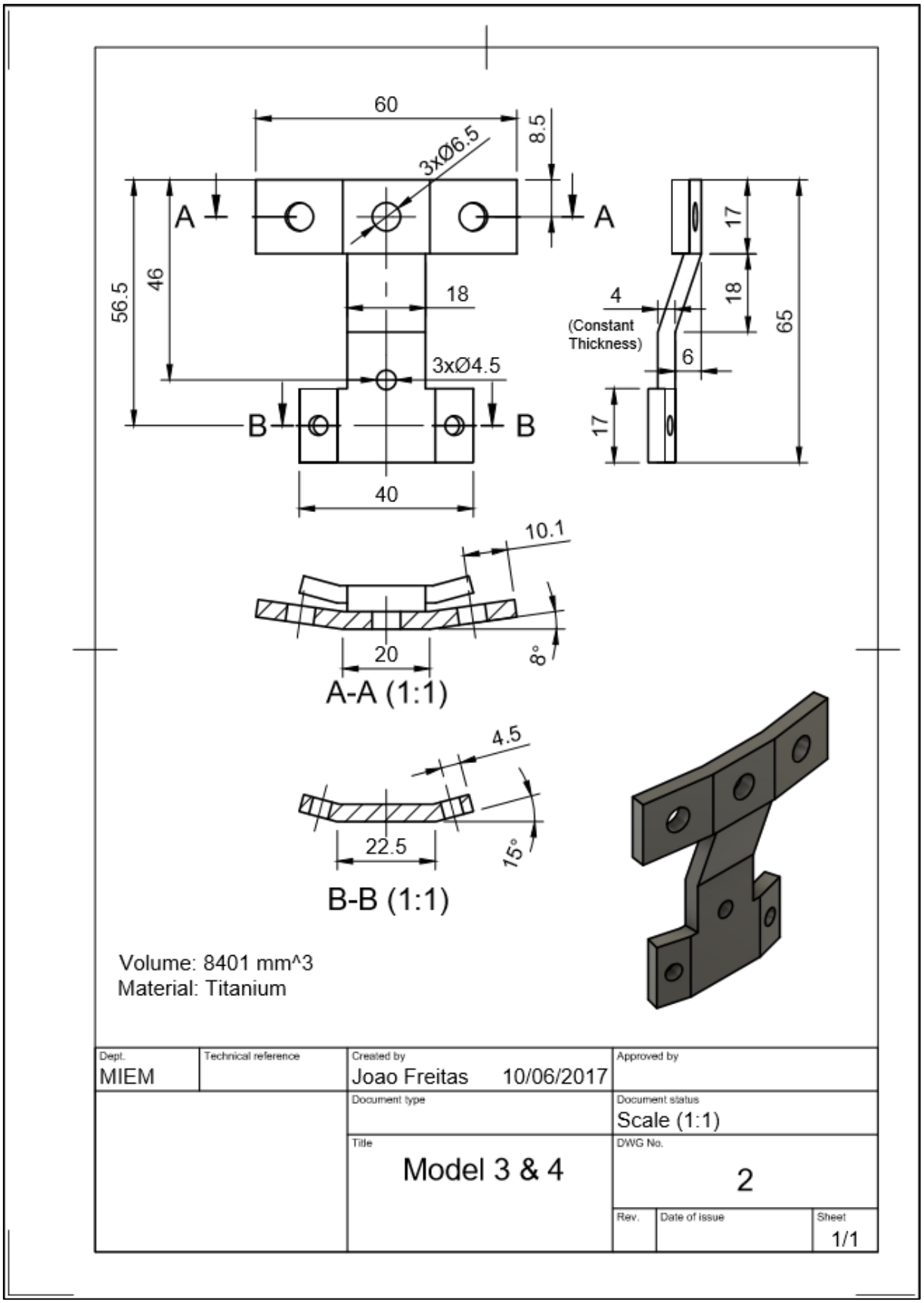

Figure 72 - Technical Drawing (Fusion360) of the second plate, used in Model 3 and Model 4.

The Final Models were built with the possibility of ignoring (or not) any of the Screws. For example, from Model 1 it is very easy to obtain the Model 2, ignoring one of the previous Distal Screws; The same happens from model 3 to model 4. This was achieved by dividing the whole model in a total of Fourteen Volumes: One Volume is the Bone, the other is the Metal Plate, and, the last twelve volumes, correspond to the six screws divided, in two volumes, by the bone (Figure 73).

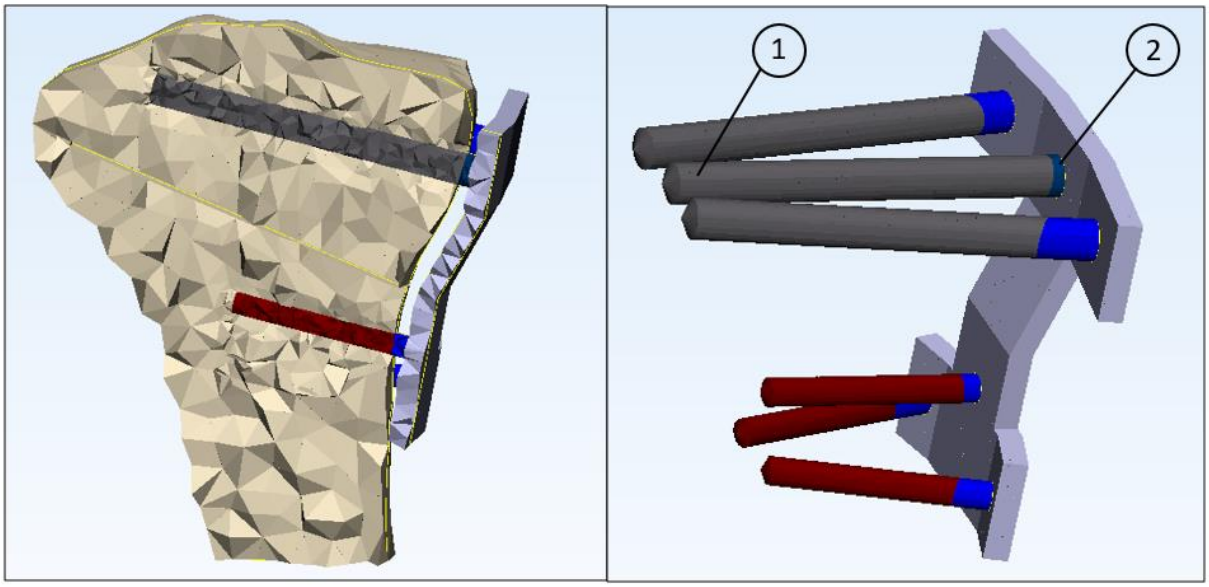

Figure 73 – Volume division of the model summing a total of 14 volumes, performed in 3-MATIC®. (1) Volume of the Screw inside the bone; (2) Volume of the Screw in-between the bone and the plate (outside the bone).

Assigning a Bone Young Modulus for the Screw interior volume ($E = 2579{,}23\ MPa$) and a low Young Modulus value for the outer volume (i.e. $E = 1^{-5}\ MPa$), the Screw is completely ignored. For the RPIM the group assignment, already presented in **section 4.5**, was repeated. Due to some inflexibility of the academic software used (FEMAS), the implant had to be placed on the tibial model before applying the opening displacement, meaning that the implant will stretch when applying the respective displacement (losing the original height dimension). The displacement was applied in 4 different points that belong to the upper side of the osteotomy cut.

After the "osteotomy opening" the new position of the nodes is saved using a programming routine (**Annex A-4**). The model is now ready for the Intraoperative and Postoperative analysis.

4.8 Intraoperative analysis

This analysis reflects the moment right after the positioning of the fixation implant, where the opened tibia is exerting a natural closing force, here named as Surgical Force. Again, the previous programming routine (**Annex A-4**.) was utilized, which also calculates the Surgical Force, resulting from the 10mm displacement, for each direction (equations (65)). Then, each force component is divided by 4 and applied at the same 4 points where the displacement was previously applied (Figure 74).

$$F_{xx} = -5678{,}40\ ;\ F_{yy} = 240{,}84\ ;\ F_{zz} = -1419{,}60\ ;\ F_{r} = 6386{,}40\ (N) \qquad (65)$$

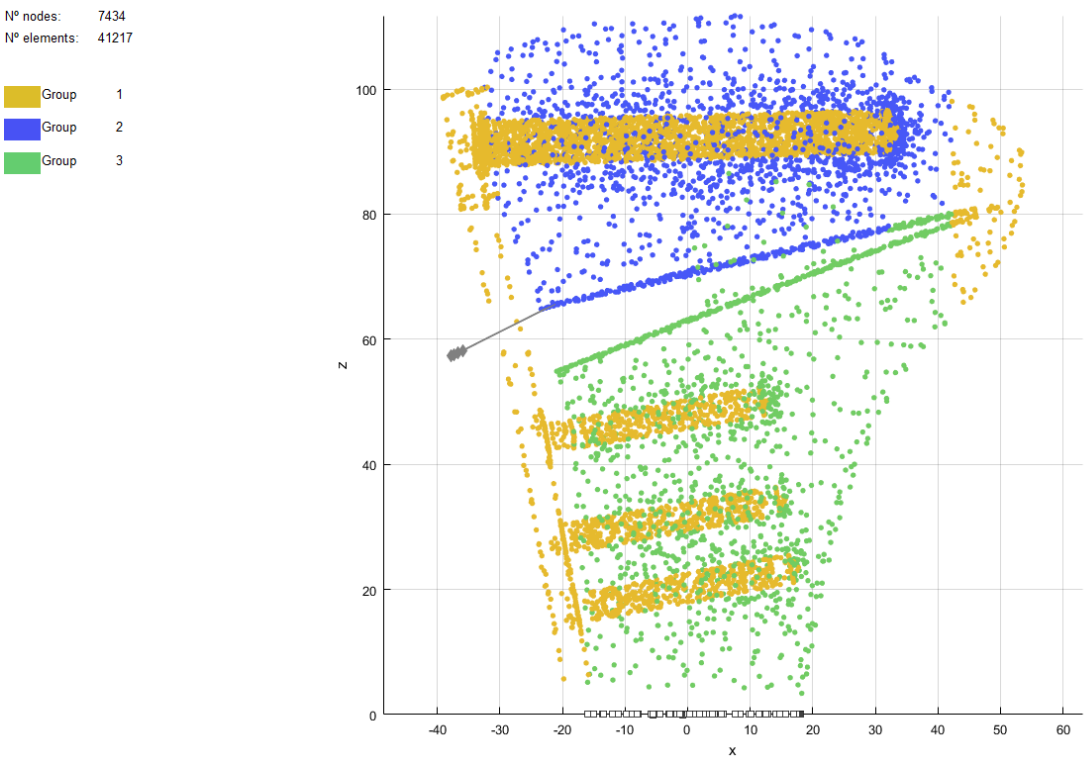

Figure 74 –Intraoperative Boundary Conditions with group assignment (Force scale = 0,01).

The results of the Intraoperative Linear-Elasto-Static analysis, that includes the number of nodes, the mean values of the Bone (Tibia) Stress, the Implant Stress and the Model Displacement, are presented in the following tables.

Table 34 – FEM results from the Intraoperative situation.

Variables	Model	Number of nodes	Mean
Bone Stress [MPa]	**1**	3337	12,28
	2	3669	12,73
	3	4285	10,23
	4	4097	10,61
Implant Stress [MPa]	**1**	3855	58,38
	2	3633	52,75
	3	4430	47,30
	4	3945	42,25
Model Displacement [mm]	**1**	7434	-1,10
	2		-1,10
	3	8285	-1,26
	4		-1,31

Table 35 – RPIM results from the Intraoperative situation.

Variables	Model	Number of nodes	Mean
Bone Stress [MPa]	**1**	3337	4,25
	2	3669	4,26
	3	4285	4,72
	4	4097	4,72
Implant Stress [MPa]	**1**	3855	38,52
	2	3633	36,54
	3	4430	26,98
	4	3945	23,96
Model Displacement [mm]	**1**	7434	-0,14
	2		-0,14
	3	8285	-0,36
	4		-0,36

Graphical comparison of the previous values, are presented in the following Figures Figure 75Figure 76Figure 77. In Tables Table 36Table 37 it is presented the plotted results of the Effective Stress (in MPa) and Displacement (mm) for each model.

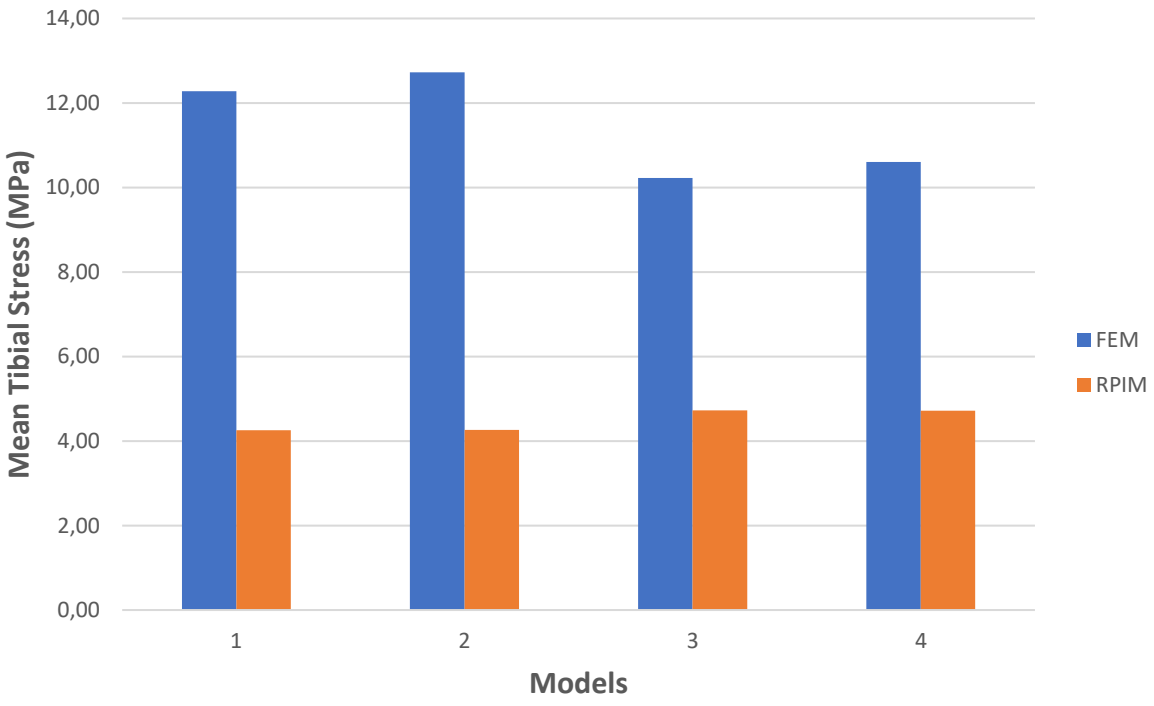

Figure 75 – Comparison of the Mean Tibial Effective Stress, between FEM and RPIM, for the Intraoperative situation.

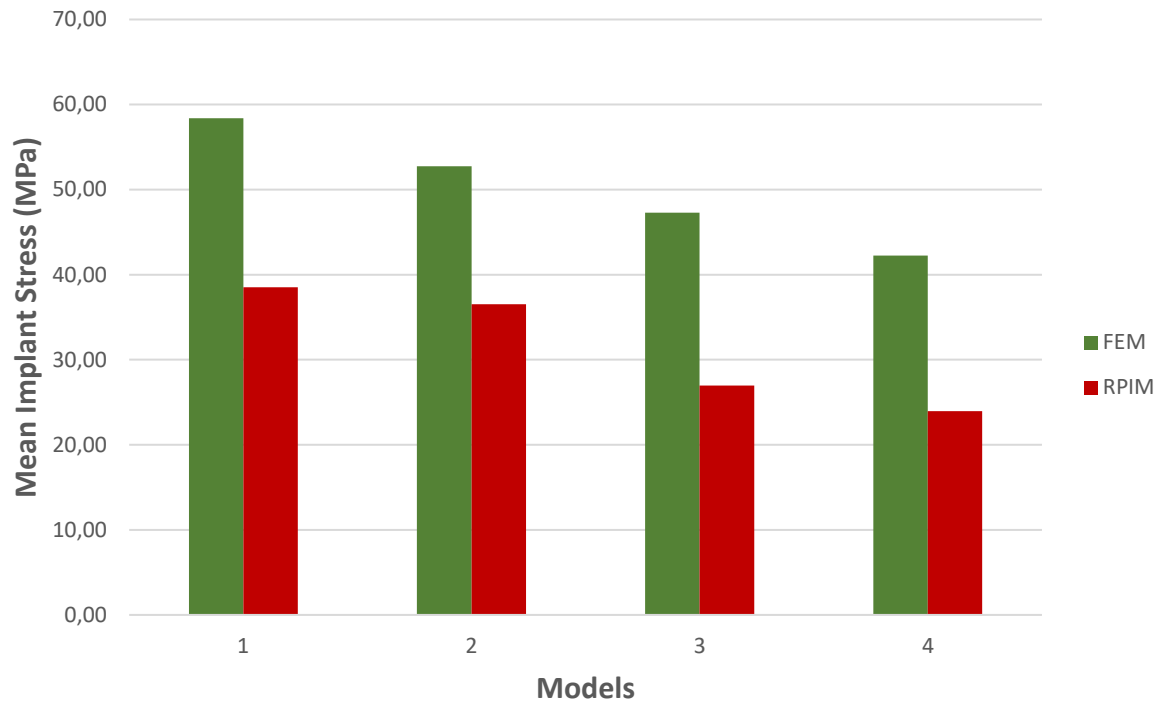

Figure 76 - Comparison of the Mean Implant Effective Stress, between FEM and RPIM, for the Intraoperative situation.

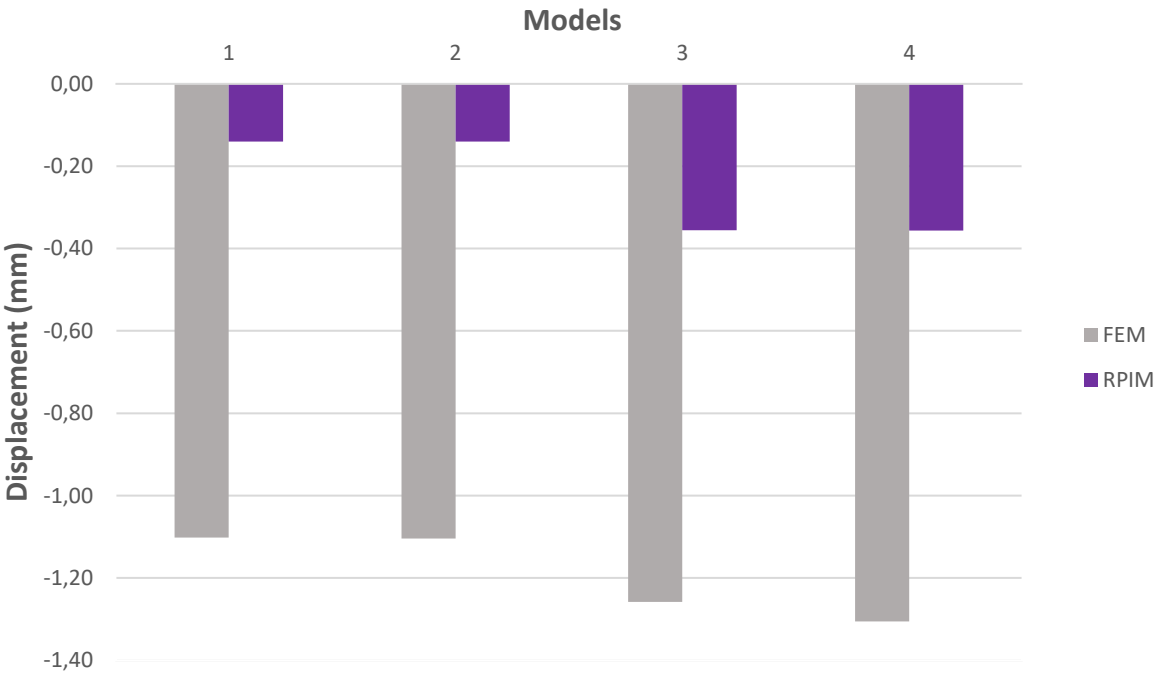

Figure 77 - Comparison of the Mean Model Displacement, between FEM and RPIM, for the Intraoperative situation.

Table 36 – Intraoperative Effective Stress and Displacement values, obtained with FEM, for each model.

Model	Effective Stress (MPa)	Displacement (mm)
1	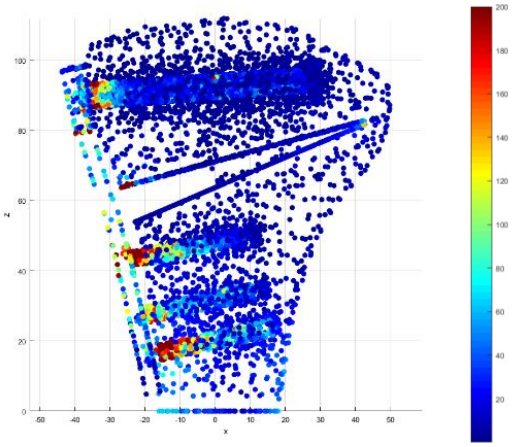	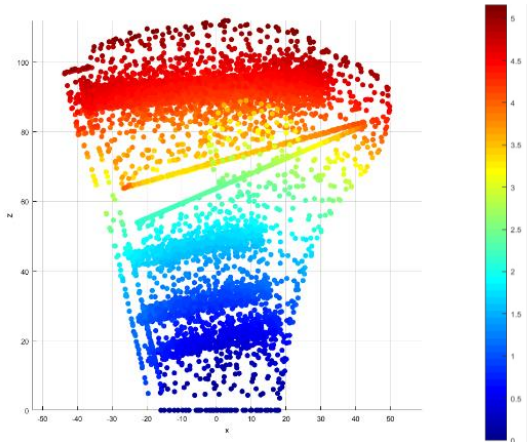
2	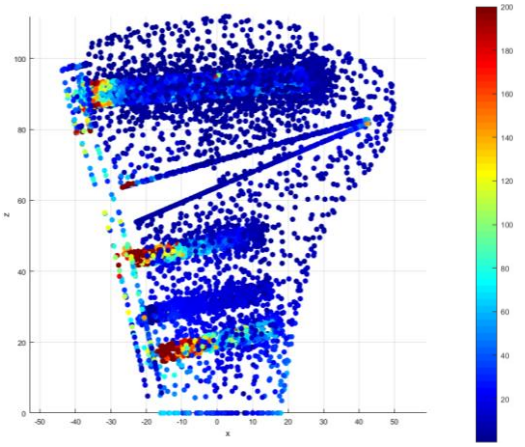	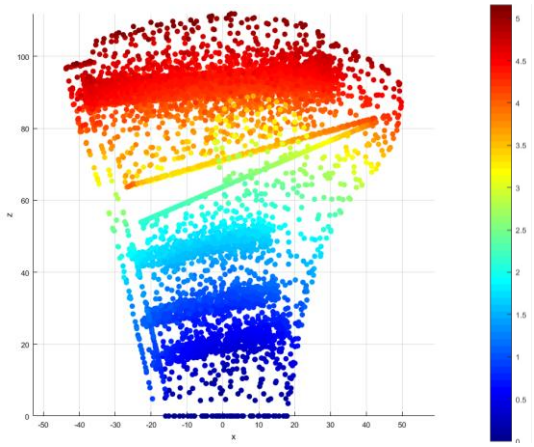
3	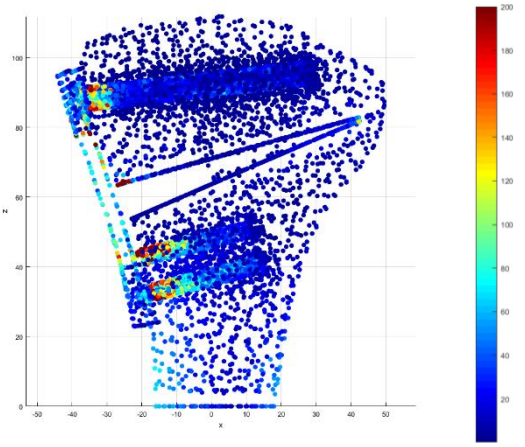	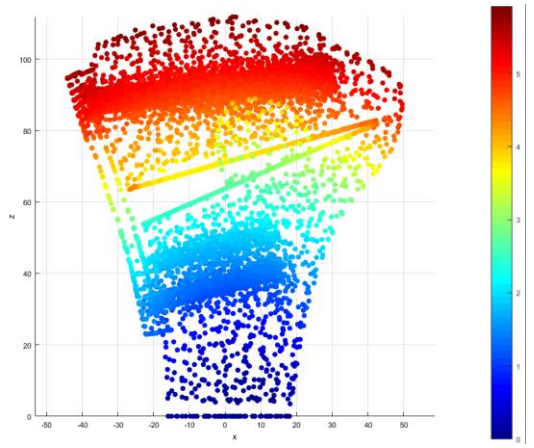
4	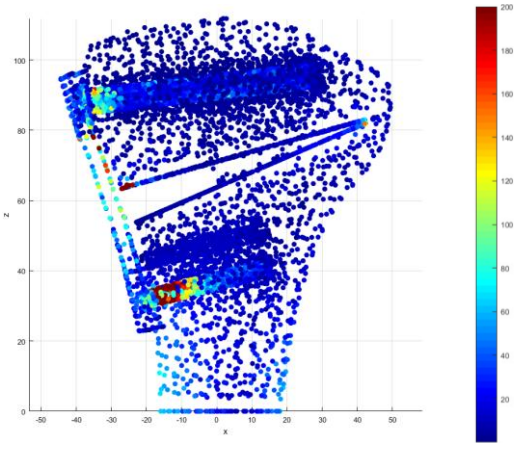	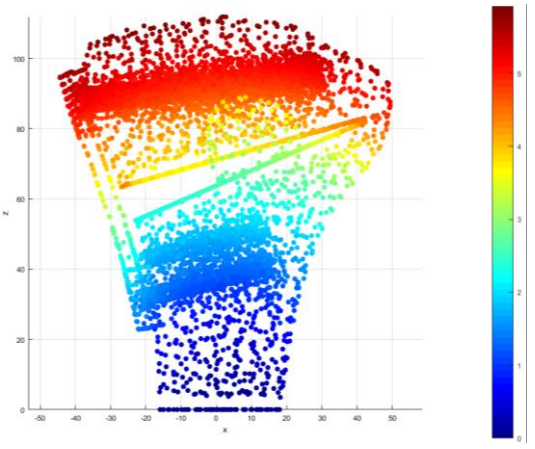

Table 37 – Intraoperative Effective Stress and Displacement values, obtained with RPIM, for each model.

Model	Effective Stress (MPa)	Displacement (mm)
1	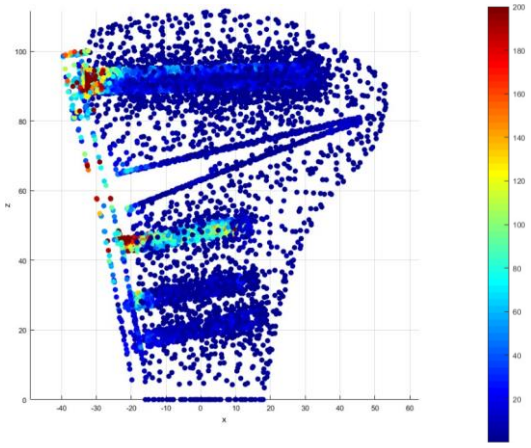	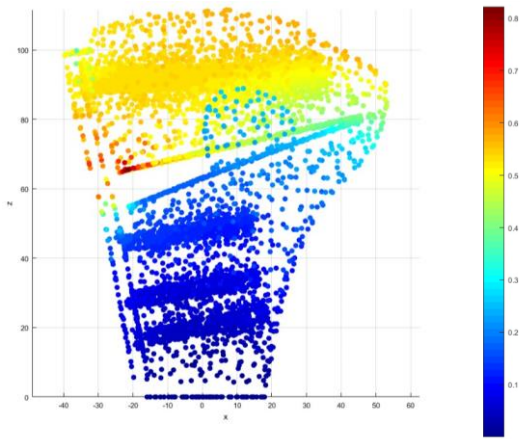
2	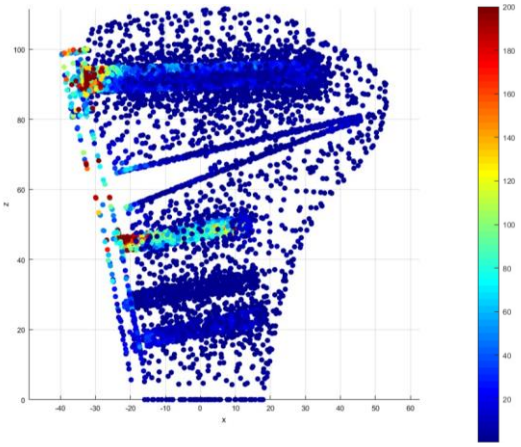	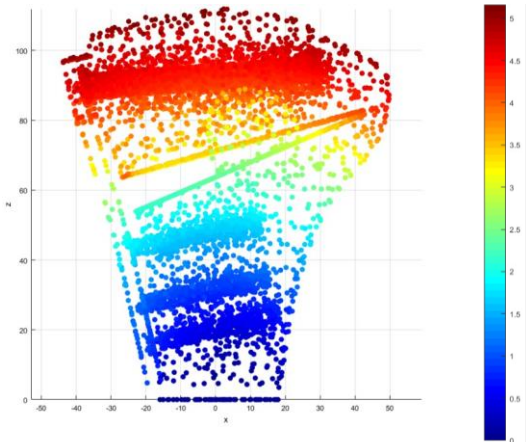
3	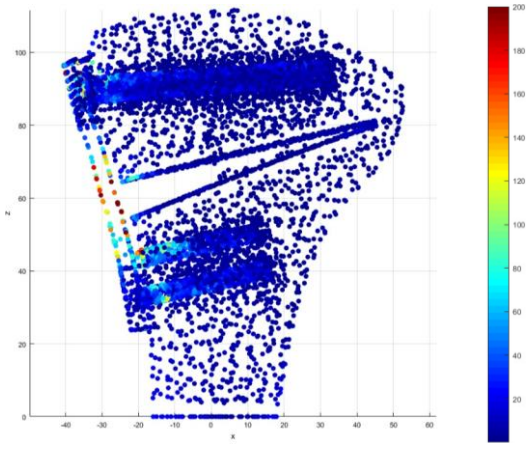	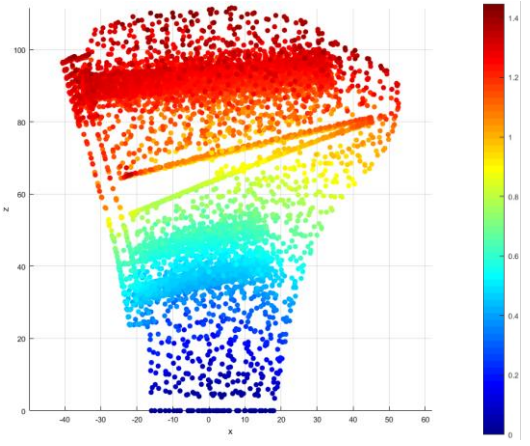
4	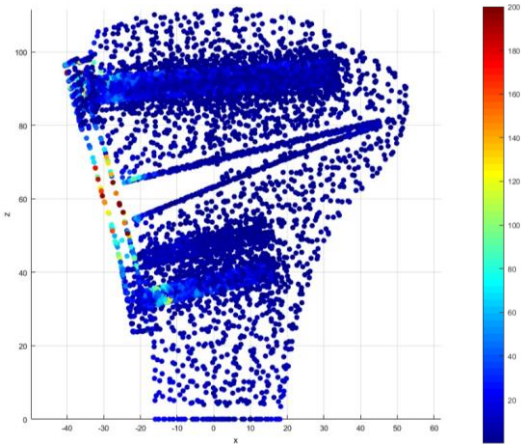	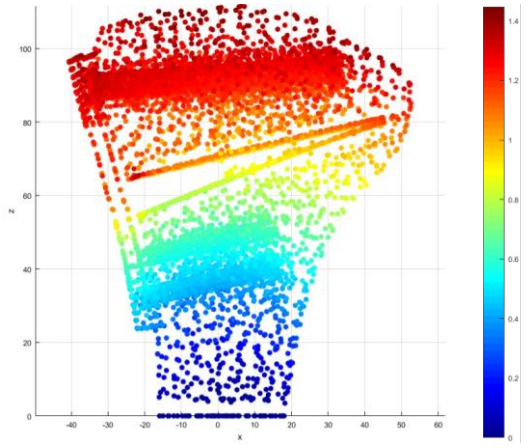

4.9 Postoperative analysis with Surgical Load

This analysis reflects the situation, right-after surgery, with the patient standing on his feet. The Surgical Load is still being exerted, adding the natural boundary conditions from the normal situation previously presented in **section 4.2**, in Table 3.

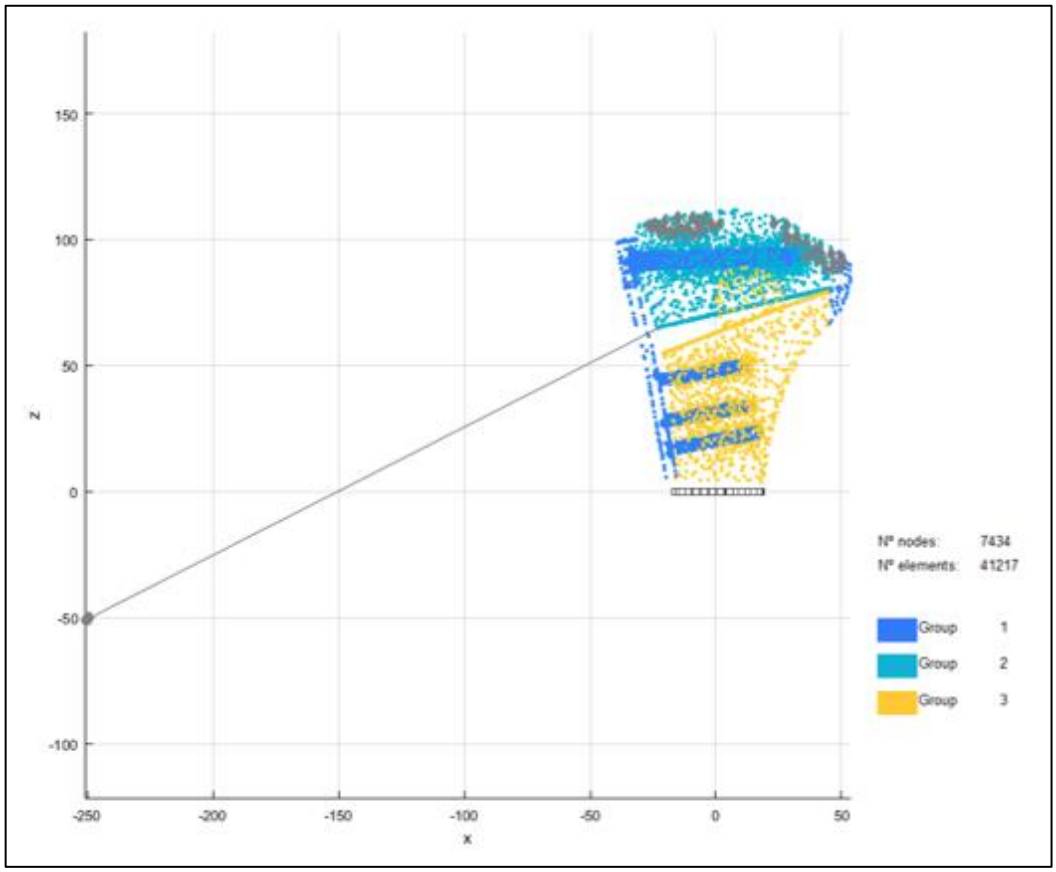

Figure 78 - Postoperative natural and essential boundary conditions (Surgical Force plus the Normal Loading) with group assignment (Force scale = 0,2).

Table 38 - FEM results of the Postoperative situation.

Variables	Model	Number of nodes	Mean
Bone Stress [MPa]	**1**	3337	12,11
	2	3669	12,64
	3	4285	10,02
	4	4097	10,39
Implant Stress [MPa]	**1**	3855	58,31
	2	3633	52,72
	3	4430	47,67
	4	3945	43,66
Model Displacement [mm]	**1**	7434	-1,05
	2		-1,05
	3	8285	-1,18
	4		-1,23

Table 39 - RPIM results of the Intraoperative situation.

Variables	Model	Number of nodes	Mean
Bone Stress [MPa]	**1**	3337	4,81
	2	3669	4,83
	3	4285	5,08
	4	4097	5,09
Implant Stress [MPa]	**1**	3855	40,19
	2	3633	37,88
	3	4430	27,79
	4	3945	24,75
Model Displacement [mm]	**1**	7434	-0,15
	2		-0,15
	3	8285	-0,28
	4		-0,28

Graphical comparison of the previous values, are presented in the following Figures 79,80 and 81. In Table 40 and Table 41 it is presented the plotted results of the Effective Stress (in MPa) and Displacement (mm) for each model.

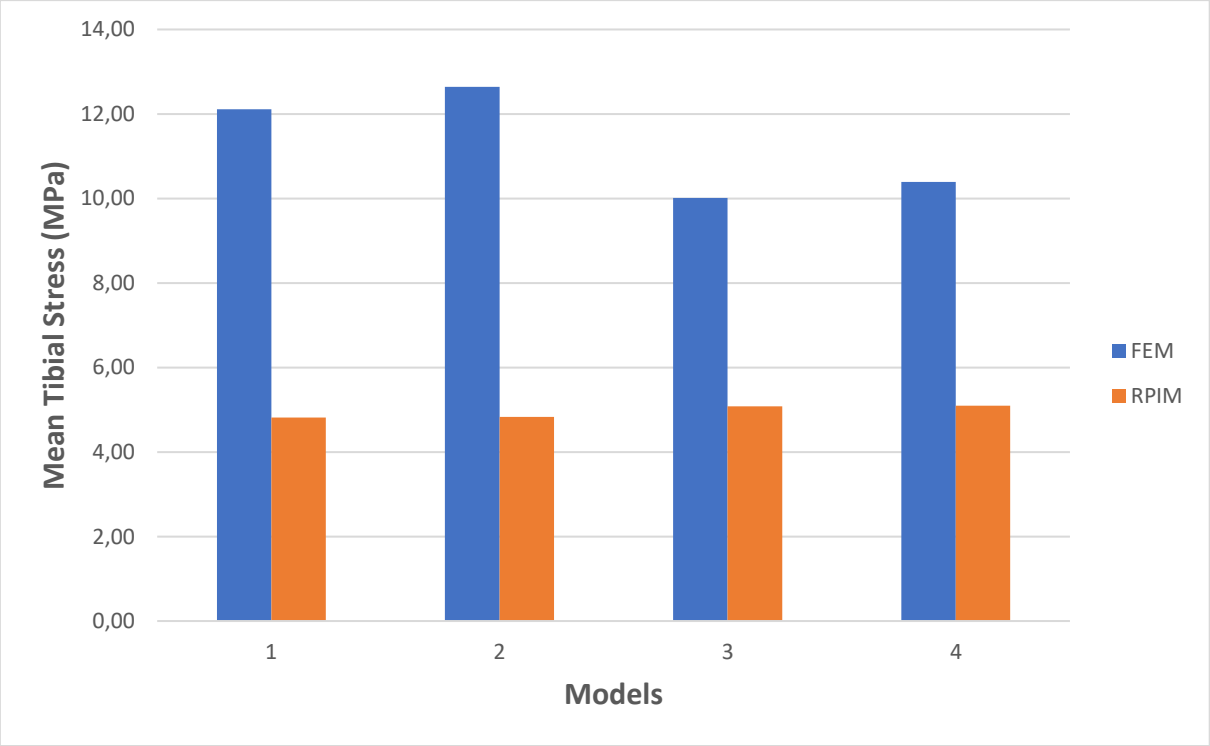

Figure 79 - Comparison of the Mean Tibial Effective Stress, between FEM and RPIM, for the Postoperative situation.

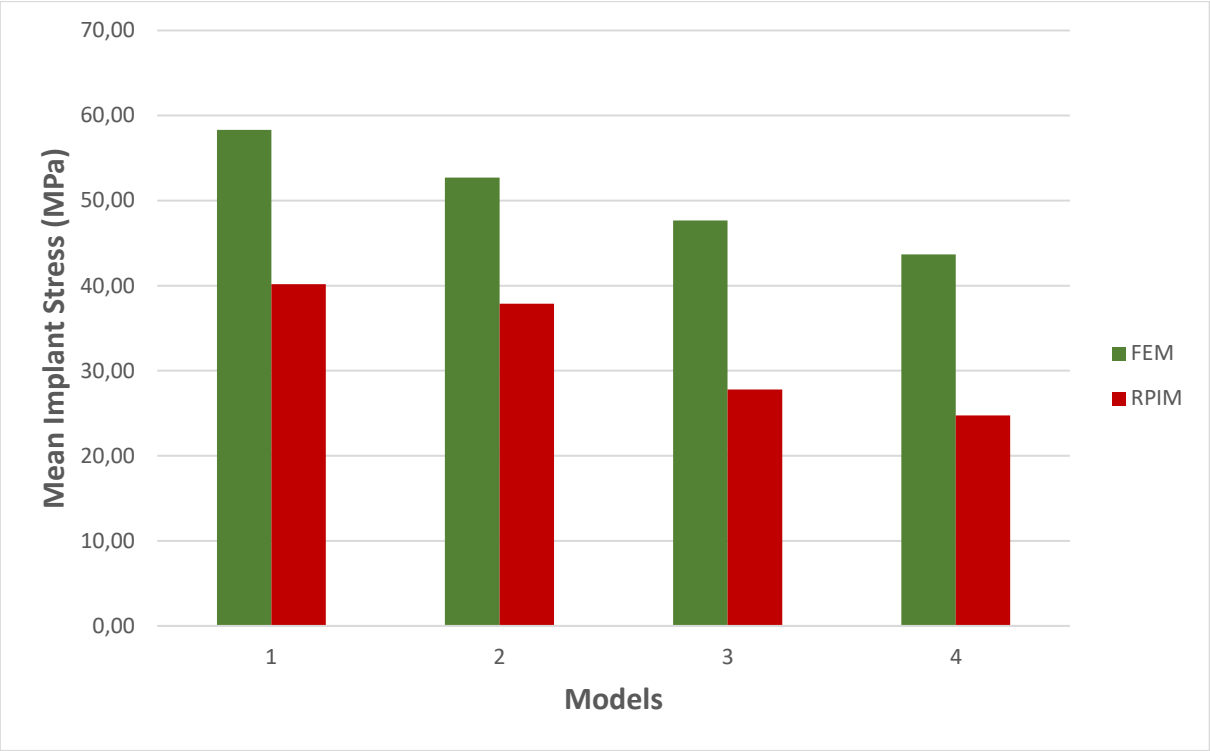

Figure 80 - Comparison of the Mean Implant Effective Stress, between FEM and RPIM, for the Postoperative situation.

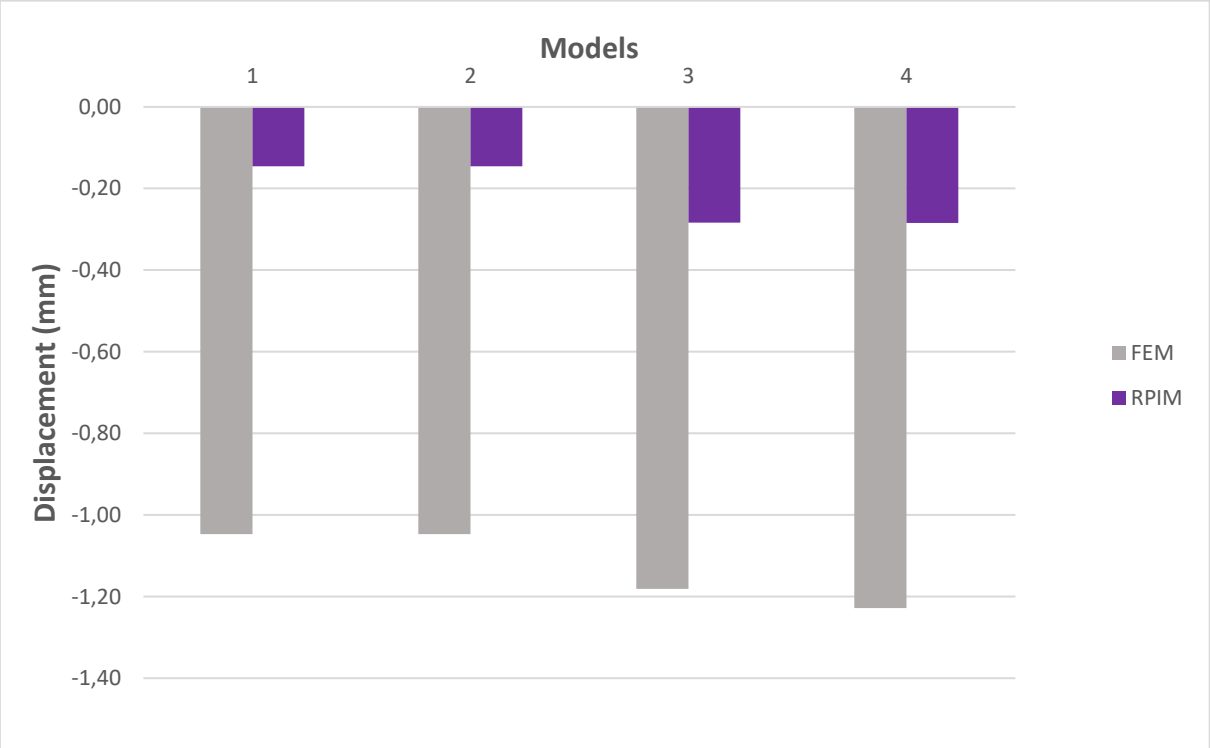

Figure 81 - Comparison of the Mean Model Displacement, between FEM and RPIM, for the Postoperative situation.

Table 40 – Postoperative Effective Stress and Displacement values, obtained with FEM, for each model.

Model	Effective Stress (MPa)	Displacement (mm)
1	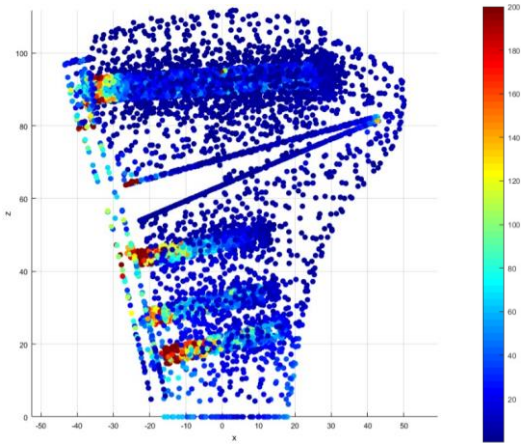	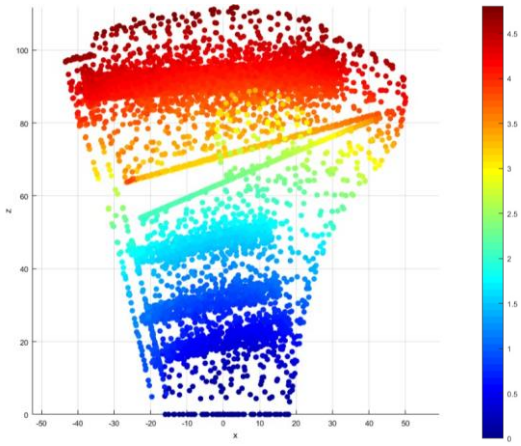
2	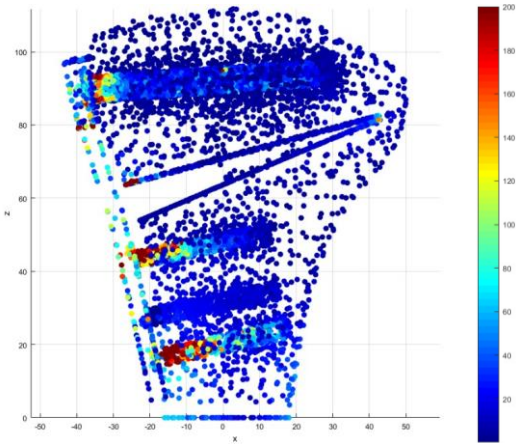	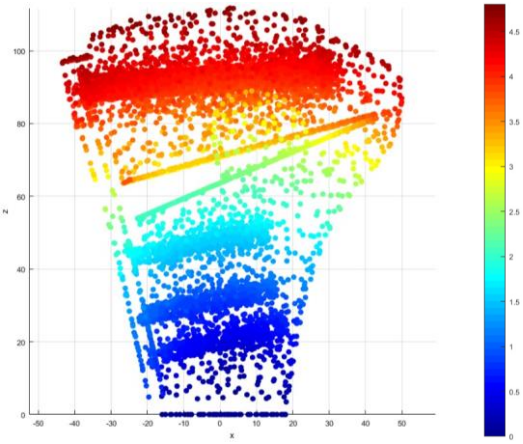
3	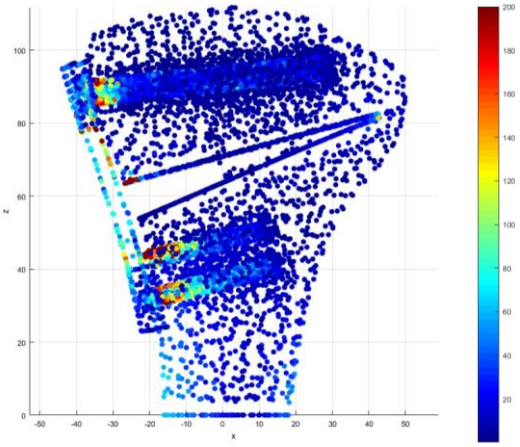	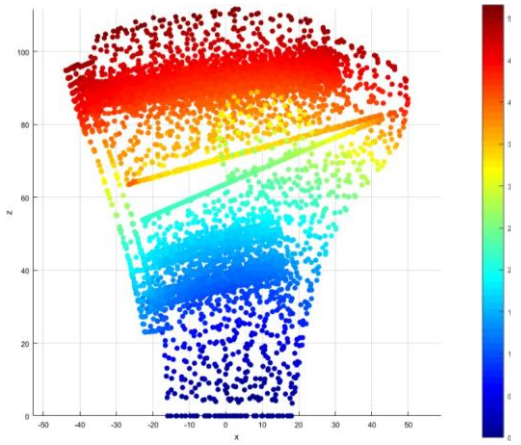
4	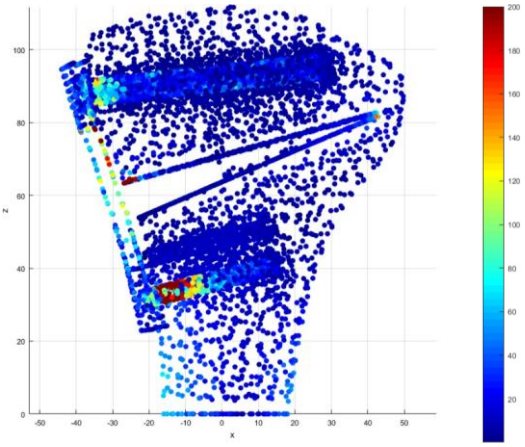	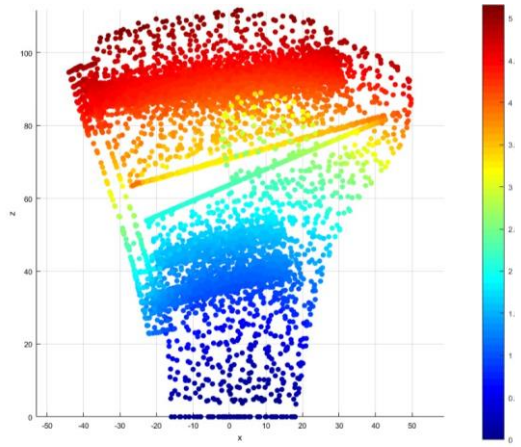

Table 41 – Postoperative Effective Stress and Displacement values, obtained with RPIM, for each model

Model	Effective Stress (MPa)	Displacement (mm)
1	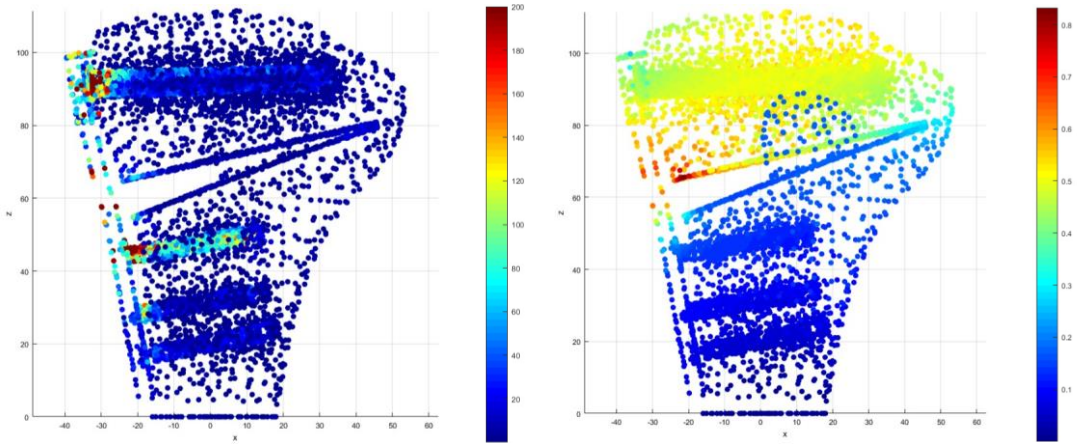	
2	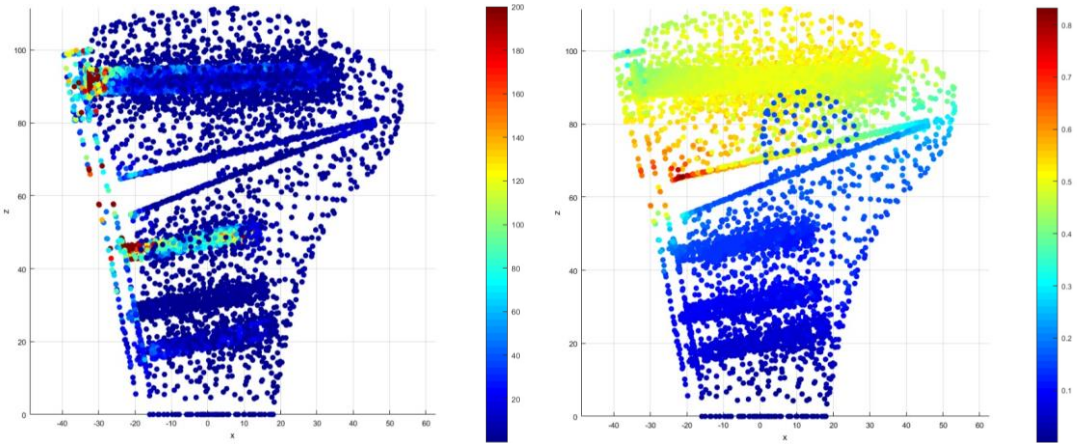	
3	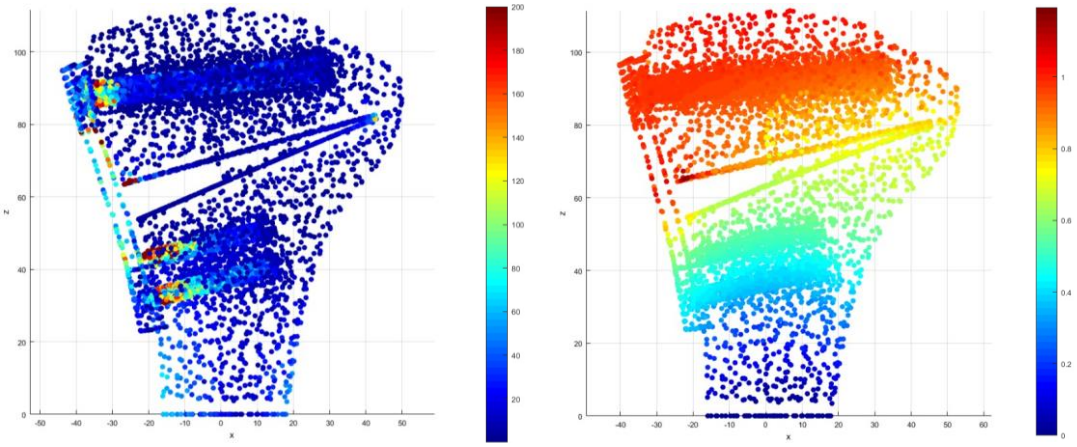	
4	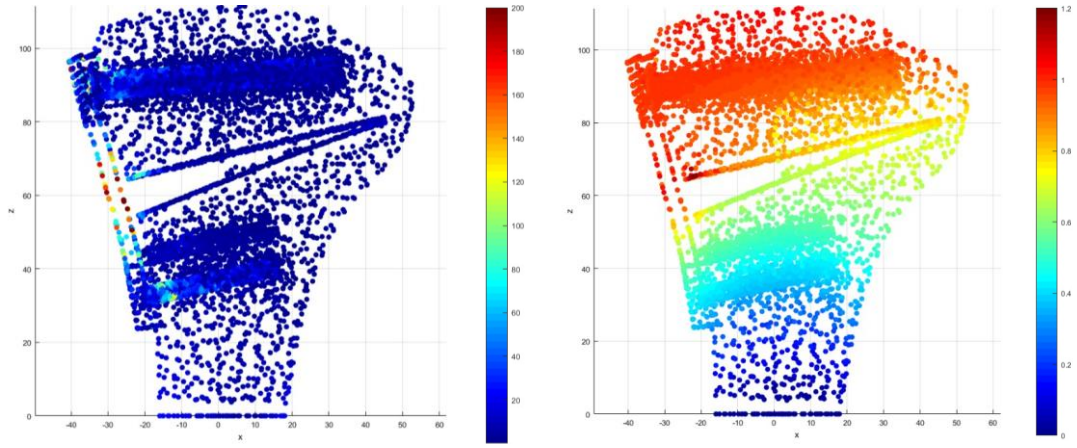	

4.10 Intraoperative and Postoperative results

In the study conducted by *Raja Izaham et al.*, it is said that higher values of the Effective Stress in the Implant mean a better anchorage (stability), displacing the stresses transmitted by the tibial acting forces. In clinical application, this stress shielding effect may cause severe osteoporosis in the long term. In the other hand, a higher degree of relative micromotion (higher model displacement) may result in implant loosening and loss of fracture stability. However, small amounts of motion may be good for fracture healing. (Raja Izaham et al. 2012) It was concluded that having a more rigid bone-implant system would be compensated with the loss of micromotion, that can lead to non-union and failure.

The characteristics of the load or stress distribution through every model were observed. The lowest mean effective Stress values, at the implant, were obtained in Model 4 (42.25 MPa from FEM and 23.96 MPa from RPIM), keeping a relatively low mean stress at the bone (10.61 MPa for FEM and 4.72 MPa for RPIM). However, a higher degree of motion or model displacement (-1.31 mm from FEM and -0.36 mm from RPIM) was also observed for this model. The contrary happens for Model 1, where the highest mean stress value and lower bone mean stress, and model displacement, are observed.

Following the same conclusions as *Raja Izaham et al.* it is possible to affirm that Model 1 will provide better stability (implant underwent a higher amount of stress with lower amounts of displacement) than Models 2, 3 and 4. However, the best compromise between the ideal amount of bone stress, implant stress and model displacement, providing the necessary structural stability, is still unknown.

The Postoperative results follow the same pattern of the Intraoperative analysis concerning the mean effective stress values of the implants, for both FEM and RPIM - Model 1 still has the highest value (58,31 MPa from FEM and 40,19 MPa from RPIM), followed by Models 2, 3 and 4. In every model, the bone underwent lower amounts of effective stress. For Model 3 and 4, using RPIM, the model displacement increased 0,1mm. However, the calculated normal forces acting on top of the tibia will reduce the amount of model displacement for the rest of the cases.

The implant stress values from the Intraoperative and the Postoperative situations (Figure 76 and Figure 80) are very similar. This means that the Surgical Load is the main contributor of the implant solicitation. To confirm this conclusion, a RPIM analysis, having only the Postoperative forces previously calculated (Table 3) was conducted, using Model 1, obtaining the following results (Figure 82):

$$Bone\ stress = 1{,}079\ MPa\ ;\ Implant\ Stress = 6{,}920\ MPa\ ;$$

$$Model\ Disp. = -0{,}006\ mm \tag{66}$$

The previous Intraoperative results for Model 1 using RPIM ($Bone\ stress = 4{,}250\ MPa\ ;\ Implant\ Stress = 38{,}52\ MPa\ ;\ Model\ Disp. = -0{,}14\ mm$) are four times higher than the one obtained with this analysis. Obtaining and applying the Surgical Force is a crucial step when designing the fixation implants for the OWHTO.

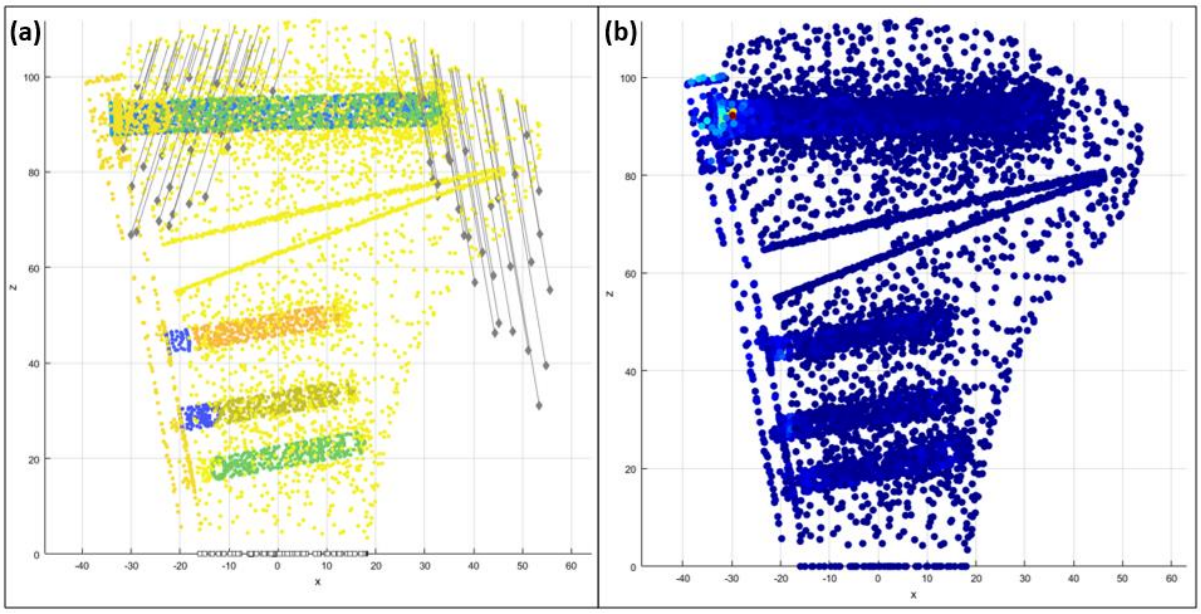

Figure 82 – (a) Additional analysis only considering the previous normal forces acting on top of the tibia (Force scale = 1); (b) RPIM results of the Effective Stress.

Another relevant analysis can be made regarding the maximum values of effective stress of the fixation implants, in comparison with the Ultimate Compression Tension of the Titanium (Table 7). For both Intraoperative and Postoperative situations and for every implant model, the maximum values of the effective stress (in at least ten points situated on the Cortical and Distal Screws) are higher than 275-290 MPa, meaning that a fail of the implant could be eminent. However, when only considering the forces acting on top of the tibial plateau (without the Surgical load) the maximum values of the effective stress are, for every model, lower than the strength of the material, and situated in the range of 150-200 MPa. Again, it is evident that the Surgical Force resultant from the right-after osteotomy cut opening is much more significative and, therefore, more demanding for the implant.

From the Intraoperative and Postoperative results analysis, it is possible to verify a significant difference between RPIM and FEM values.

5 Resume

The Open Wedge High Tibial Osteotomy is nowadays the best cost-effective option to treat knee osteoarthritis of the medial compartment for patients that are younger than 60 years old. (W. B. Smith et al. 2017) This problem affects a large group of individuals worldwide, where annual estimations of €5,7 billion are made for the current market of knee replacement surgeries. (W. B. Smith et al. 2017) The development and further optimization of the fixation implants used in OWHTO becomes a very important and promising task, for the future market.

Overall, all pre-objectives previously stated, in the **Introduction**, were completed. This present work had the ultimate objective of encounter an optimal prosthesis design, using FEM and RPIM, in an Academic program named FEMAS, always comparing both numeric results. From the structural analysis of the implants, the CountorLock® system (Model 1) was the best design in terms of stability, meaning that the primary objective was also accomplished.

It was defined the importance of some considerations when designing those implants, like having the pre-contoured shape and the bone-implant gap calculation, and the importance of studying the Surgical Load.

In terms of the osteotomy, it was demonstrated that the use of a circular hinge and a longer osteotomy cutting length, lead to lower levels of bone stress, reducing the risk of crack propagation and/or fracture and failure.

6 Conclusions and future recommendations

As primary conclusion, regarding the main objective of this thesis (developing the optimal implant design), the results showed that Model 1 offers the best anchorage of the bone-implant system, based on the same conclusion of *Raja Izaham et al*. This Model follows the design of an existing plate from Arthrex® named as ContourLock® plate, that uses six fixation screws. Still, further investigation should be made to determinate the ideal compromise between the ideal amount of bone stress, implant stress and model displacement, providing the necessary structural stability. It is important to refer that a pre-contoured plate is recommended in case the proximal tibia is highly concave, where the opening height of the osteotomy is insufficient to stretch the tibial profile, inflicting more effort in the implant. (Weng et al. 2017)

As secondary conclusion, the obtained results from RPIM are revealed to be "smoother", without abrupt variations of stress values, when compared to FEM results. This can be explained by the fact that the FEM has, in its nature, a reduced nodal connectivity (the shape functions are constructed using only 4 nodes, and for the RPIM, shape functions are built using 27 nodes). The major differences between both discrete numeric methods was verified at the Intraoperative and Postoperative analysis. The literature shows that one of the major advantages of the RPIM over FEM is the production of more accurate results. (Belinha 2014) Since there is no exact solution available for the problem analysed in the scope of the present work, the mentioned advantage could not be verified. Nevertheless, the RPIM possesses some disadvantages over the FEM, one of which is the higher computational cost. In Table 42 are shown the typical computational costs (measured in seconds) of both RPIM and FEM analyses. Another relevant disadvantage is the necessity to identify the independent parts of the domain (group assignment).

Table 42 – Computational cost from the Intraoperative analysis (Model 3), comparing FEM and RPIM.

Numeric method	Pre-processing (s)	Analysis (s)
FEM	8,2	931,2
RPIM	82,1	1016,5

Those stress values difference can also be explained with the low density of the discretization mesh. Since no convergence test was performed in this work, no conclusions can be made regarding the best solution. However, the literature shows that meshless methods converge faster than the FEM, specially the tetrahedral element. Notice that, due to hardware limitations, the computation is limited to a maximum number of 8285 nodes for 3D analyses, hindering further analysis using denser nodal discretisation. Additionally, the finite element mesh is highly distorted near the hinge (or crack tip), which can lead to unexpected results (high local strain/stress fields). On the other hand, the meshless method formulation shows a significant difficulty to recognize the crack tip. If a Boolean operation is not considered, the meshless formulation will consider (by definition) the nodes on one side of the cut and the nodes of the opposite side of the cut as part of the same continuum, naturally disregarding the cut opening. This effect can explain the values obtained for meshless methods (low stress values near the crack tip). The influence domain concept smooths the material properties of near nodes on the interface between distinct material, such as the implant/bone interface. This undesirable effect leads to errors in the stress/strain fields on those interfaces.

Despite the impossibility to compare directly the RPIM and FEM results, the experience acquired with this work allows to affirm that meshless methods are useful tools to analyse

complex biomechanical problems, allowing to discretize directly the problem domain from the DICOM's images and to set automatically the material properties to each node. Nevertheless, these meshless techniques require much more computational power than FEM, and therefore its massive use is dependent on the technologic evolution.

Multiple analyses were also performed along the present work and, consequently, other tertiary conclusions were obtained.

Starting with the geometric model made to calculate the tibial plateau forces (**section 4.2**), results showed that the vertical force values were always higher in the lateral condyle of the femur (even for the maximum varus situation), which goes against literature. This can be explained with the simplistic assumptions made for the natural boundary conditions and the femur contour used. However, the same vertical force magnitude grows in the medial condyle for a crescent varus deformation (decreasing in the lateral site), and grows in the lateral condyle for a crescent valgus deformation (decreasing in the medial site), which is a positive conclusion.

The Initial Stress distribution analysis (**section 4.4**) had the objective of comparing both FEM and RPIM results. The biggest difference was verified in Point 3, for the 3-material assignment, where the Effective Stress (and the principal stress component σ_{33}), obtained with FEM, is four times higher than RPIM's value.

Regarding **section 4.5**, it was concluded that the longer the osteotomy cut (towards the fibula tip) the lower stresses are at the bone. No relevant differences between both numeric methods was achieved. Still in this section, the circular hinge in the osteotomy was tested obtaining stress (at the bone) reductions around 30-35% compared to a normal hinge. The amount of stress reduction was not as high as the values obtained from Arthrex (Arthrex 2016), but it validates their conclusion, that this technique decreases significantly the maximum effective stress values by homogenization of the area around the hinge pin hole, preventing crack initiation and lateral cortex fracture. This technique is very relevant for future implementation in the OWHTO.

The present work had some limitations, and they are here listed:

i. The number of nodes used in every analysis was limited by the equipment available, where the computational cost, and time, were important factors to take into consideration. Furthermore, the academic software used (FEMAS) is not adapted for large computations. Those limitations affected, mostly, the Tibial Model shape and, consequently, the results accuracy;
ii. Not having a real patient case with experimental measurements was also a limitation in terms of precision of the results. Instead, a Geometric Model was made to generally calculate the Tibial forces;
iii. The Geometric Model assumptions to achieve the natural boundary conditions were very simplistic, not considering, for example, the knee ligaments, muscle attachment, and tendons;
iv. It was only considered Linear-Elasto-Static analysis, as the idealistic dynamic motion of the joint analysis was impossible in terms of resources;
v. The material assignment was very simplistic, only considering a homogenised bone for the majority of the numeric analysis, forgetting the real bone constitution (Trabecular and Cortical bone);
vi. The final models were built with the implant placed before "performing the osteotomy" losing some of the original shape (due to the inflexibility of the software used);
vii. The number of implants tested are not sufficient to declare which design is the best in terms of the compromise between displacement and stress;

The future recommendations are the following:

i. Use a real case study to obtain, with more accuracy, the external forces acting on the tibia. Instead of assuming an individual in a standing position, we could have an individual walking/running to obtain a more extreme case of tibial solicitations. This analysis could take place in the LABIOMEP, which is an experimental Biomechanics Laboratory, a biomechanical technological centre of the University of Porto;
ii. Reformulate the problem boundary conditions considering knee ligaments, muscle and the tendons that are attached to the tibia. The calculation of the Surgical Load should also be reviewed to achieve more accurate values;
iii. Use Bone Remodelling Algorithms, to correlate the actual stress distribution and stress path, from the mechanical bone stimulus, with the bone growth. This is a straight-forward step. The bone tissue remodelling algorithm, adapted from Carter's Model, for meshless methods (Belinha 2014), could be used here;
iv. In the Numeric Analysis, considering a nonlinear elastoplastic analysis, assuming a anisotropic yield criterion, for more accurate results;
v. Study other Implant designs varying the number of fixation holes and the volume of material, in order to understand the plate response and to study the stress distribution at the screws. The analysis of the Tomofix® plate should be performed and compared again with the implants presented in this work;
vi. Conduct a real experimental essay (static or dynamic) using the Bone-Implant system presented in this work, with the objective of determining which implant provides the best compromise between the bone stress, implant stress and whole model displacement, until failure.

References

Arthrex. 2013. “iBalance HTO System for Medial High Tibial Opening Wedge Osteotomy.”

Arthrex®. n.d. “Opening Wedge Osteotomy System Using PEEKPower , HTO Plate.”

Arthrex, Department of Reseach. 2016. “Hinge Pin Reduces Fracture Risk in Medial Opening Wedge Procedures ?”

Atluri, S. N., and T. Zhu. 1998. “A New Meshless Local Petrov-Galerkin (MLPG) Approach in Computational Mechanics.” *Computational Mechanics* 22 (2): 117–27. doi:10.1007/s004660050346.

Belinha, Jorge. 2014. *Meshless Methods in Biomechanics: Bone Tissue Remodelling Analysis*. *Lecture Notes in Computational Vision and Biomechanics.* Vol. 16. doi:10.1007/978-94-007-4174-4.

Belytschko, Ted, and M. Tabbara. 1996. “Element-Free Galerkin Method.” *International Journal for Numerical Methods in Engineering* 39 (6): 923–38. doi:10.1002/(SICI)1097-0207(19960330)39:6<923::AID-NME887>3.0.CO;2-W.

Benzakour, Thami. 2010. “Osteotomy around the Knee : State of the Art and New Challenges.” *International Orthopaedics* 34: 151–53. doi:10.1007/s00264-009-0.

Brinkman, J.-M, P Lobenhoffer, J D Agneskirchner, A E Staubli, A B Wymenga, R J Van Heerwaarden, J.-M Brinkman, et al. 2008. “Osteotomies around the Knee PATIENT SELECTION, STABILITY OF FIXATION AND BONE HEALING IN HIGH TIBIAL OSTEOTOMIES.” *The Journal of Bone and Joint Surgery* 90: 1548–57. doi:10.1302/0301-620X.90B12.

Brouwer, R W, S M Bierma-Zeinstra, T M van Raaij, and J A Verhaar. 2006. “Osteotomy for Medial Compartment Arthritis of the Knee Using a Closing Wedge or an Opening Wedge Controlled by a Puddu Plate. A One-Year Randomised, Controlled Study.” *The Journal of Bone and Joint Surgery* 88 (11): 1454–59. doi:88-B/11/1454 [pii]\r10.1302/0301-620X.88B11.17743.

“CESEdupack.” 2017. http://www.grantadesign.com/education/edupack/.

Cotic, Matthias, Stephan Vogt, Stefan Hinterwimmer, Matthias J. Feucht, Julia Slotta-Huspenina, Tibor Schuster, and Andreas B. Imhoff. 2014. “A Matched-Pair Comparison of Two Different Locking Plates for Valgus-Producing Medial Open-Wedge High Tibial Osteotomy: Peek–carbon Composite Plate versus Titanium Plate.” *Knee Surgery, Sports Traumatology, Arthroscopy* 23 (7). Springer Berlin Heidelberg: 2032–40. doi:10.1007/s00167-014-2914-8.

DePuySynthesis. 2014. “TomoFix ® Osteotomy System . A Comprehensive Plating System for Stable Fixation of Osteotomies around the Knee .”

Diffo Kaze, A, S Maas, D Waldmann, A Zilian, K Dueck, and D Pape. 2015. “Biomechanical Properties of Five Different Currently Used Implants for Open-Wedge High Tibial Osteotomy.” *J Exp Orthop* 2 (1). Journal of Experimental Orthopaedics: 14. doi:10.1186/s40634-015-0030-4.

Ellis, R E, C Y Tso, J F Rudan, and M M Harrison. 1999. “A Surgical Planning and Guidance System for High Tibial Osteotomy.” *Computer Aided Surgery : Official Journal of the International Society for Computer Aided Surgery* 4 (5): 264–74. doi:10.1002/(SICI)1097-0150(1999)4:5<264::AID-IGS4>3.0.CO;2-E.

Gaasbeek, R. D A, H. Sonneveld, R. J. Van Heerwaarden, W. C H Jacobs, and A. B. Wymenga. 2004. “Distal Tuberosity Osteotomy in Open Wedge High Tibial Osteotomy Can Prevent Patella Infera: A New Technique.” *Knee* 11 (6): 457–61. doi:10.1016/j.knee.2004.02.002.

Hankemeier, S., P. Mommsen, C. Krettek, M. Jagodzinski, J. Brand, C. Meyer, and R. Meller. 2010. “Accuracy of High Tibial Osteotomy: Comparison between Open- and Closed-Wedge Technique.” *Knee Surgery, Sports Traumatology, Arthroscopy* 18 (10): 1328–33. doi:10.1007/s00167-009-1020-9.

James, Oliver. 2017. “Anatomic Terminology.” http://teachmeanatomy.info/the-basics/anatomical-terminology.

Kansa, E. J. 1990. “Multiquadrics-A Scattered Data Approximation Scheme with Applications to Computational Fluid-Dynamics-II Solutions to Parabolic, Hyperbolic and Elliptic Partial Differential Equations.” *Computers and Mathematics with Applications* 19 (8–9): 147–61. doi:10.1016/0898-1221(90)90271-K.

KJ, Bathe. 2000. “The Method of Finite Spheres.” *Comput Mech* 25 (4): 329–45.

Lancaster, P., and K. Salkauskas. 1981. “Surfaces Generated by Moving Least Squares Methods.” *Mathematics of Computation* 37 (155): 141. doi:10.2307/2007507.

Lee, Dong Chul, and Seong Joon Byun. 2012. “High Tibial Osteotomy.” *Knee Surgery & Related Research* 24 (2): 61–69. doi:10.1007/s00167-012-2084-5.

Liu, Wk, Sukky Jun, and Yf Zhang. 1995. “Reproducing Kernel Particle Methods.” *International Journal for Numerical Methods in Fluids* 20 (8–9): 1081–1106. doi:10.1002/fld.1650200824.

Monaghan, R. A. Gingold and J. J. 1977. “Smoothed Particle Hydrodynamics: Theory and Application to Non-Spherical Stars.” *Royal Astronomical Society* 181: 375–89.

Monk, A. P., J. Van Oldenrijk, Nicholas D. Riley, Richie H S Gill, and D. W. Murray. 2016. “Biomechanics of the Lower Limb.” *Surgery (United Kingdom)* 34 (9). Elsevier Ltd: 427–35. doi:10.1016/j.mpsur.2016.06.007.

Nayroles, B., G. Touzot, and P. Villon. 1992. “Generalizing the Finite Element Method: Diffuse Approximation and Diffuse Elements.” *Computational Mechanics* 10 (5): 307–18. doi:10.1007/BF00364252.

Oñate, E, S Idelsohn, O C Zienkiewics, R L Taylor, C Sacco, and S Idelsohnl. 1996. “A Stabilized Finite Point Method for Analysis of Fluid Mechanics Problems.” *Computer Methods in Applied Mechanics and Engineering* 139 (96): 315–46. doi:10.1016/S0045-7825(96)01088-2.

Paley, Dror. 2005. *Principles of Deformity Correction*. Edited by J. H. Herzenberg. 3rd ed. Baltimore, Mryland: Springer.

Raja Izaham, Raja Mohd Aizat, Mohammed Rafiq Abdul Kadir, Abdul Halim Abdul Rashid, Md Golam Hossain, and T. Kamarul. 2012. “Finite Element Analysis of Puddu and Tomofix Plate Fixation for Open Wedge High Tibial Osteotomy.” *Injury* 43 (6). Elsevier Ltd: 898–902. doi:10.1016/j.injury.2011.12.006.

Reddy’s, J.N. 2005. *An Introduction to the Finite Element Method*. Edited by McGraw-Hill.

Ribeiro, Cristiano Hossri, Nilson Roberto Severino, Ricardo De Paula, and Leite Cury. 2004. “Opening Wedge High Tibial Osteotomy.” In .

Smith, J. O., A. J. Wilson, and N. P. Thomas. 2013. “Osteotomy around the Knee: Evolution, Principles and Results.” *Knee Surgery, Sports Traumatology, Arthroscopy* 21 (1): 3–22. doi:10.1007/s00167-012-2206-0.

Smith, William B., Joni Steinberg, Stefan Scholtes, and Iain R. Mcnamara. 2017. “Medial Compartment Knee Osteoarthritis: Age-Stratified Cost-Effectiveness of Total Knee Arthroplasty, Unicompartmental Knee Arthroplasty, and High Tibial Osteotomy.” *Knee*

Surgery, Sports Traumatology, Arthroscopy 25 (3). Springer Berlin Heidelberg: 924–33. doi:10.1007/s00167-015-3821-3.

Staubli, Alex E. 2011. "Open-Wedge High Tibial Osteotomy with a Locking Plate (TomoFix) for Treatment of Medial Monocompartment Osteoarthritis." *Operative Techniques in Orthopaedics* 21 (2). Elsevier Inc.: 156–62. doi:10.1053/j.oto.2011.01.004.

Stoffel, Karl, Gwidon Stachowiak, and Markus Kuster. 2004. "Open Wedge High Tibial Osteotomy: Biomechanical Investigation of the Modified Arthrex Osteotomy Plate (Puddu Plate) and the TomoFix Plate." *Clinical Biomechanics* 19 (9): 944–50. doi:10.1016/j.clinbiomech.2004.06.007.

Wang, G., and G. R. Liu. 2001. "A Point Interpolation Method for Two Dimensional Solids." *International Journal for Numerical Methods in Engineering* 50 (4): 937–51. doi:10.1002/1097-0207(20010210)50.

Wang, J. G., and G. Liu. 2002a. "On the Optimal Shape Parameters of Radial Basis Functions Used for 2-D Meshless Methods." *Computer Methods in Applied Mechanics and Engineering* 191 (23–24): 2611–30. doi:10.1016/S0045-7825(01)00419-4.

Wang, J. G., and G. R. Liu. 2002b. "A Point Interpolation Meshless Method Based on Radial Basis Functions." *International Journal for Numerical Methods in Engineering*, no. 54: 1623–48.

Weng, Pei-Wei, Chia-Hsien Chen, Chu-An Luo, Jui-Sheng Sun, Yang-Hwei Tsuang, Cheng-Kung Cheng, and Shang-Chih Lin. 2017. "The Effects of Tibia Profile, Distraction Angle, and Knee Load on Wedge Instability and Hinge Fracture: A Finite Element Study." *Medical Engineering & Physics* 0. Elsevier Ltd: 1–7. doi:10.1016/j.medengphy.2017.01.007.

ANNEXES

ANNEX A: Programming routines used in FEMAS (MatLab® R2017a)

1. Routine used to calculate the forces acting on both medial and lateral condyles. The reaction force vector is the product of the stiffness matrix ***K*** with the displacement vector ***u: F_reac=Ku***. Then, the routine searches the points in which were initially applied the imposed displacements and the it obtained the corresponding reaction forces, firstly on the left side ("condilo esquerdo") and then on the right side, ("condilo direito") accumulating them into a resultant force (fx_dir, fy_dir, fx_esq, fy_esq).

```
load('femas10001.mat')
load('stiff_mat_file.mat')

% reaction forces
f_reac = k_mat*displ_v;

lower_y = 10;
midle_x = 60;

% loop over all nodes
fx_dir = 0;
fy_dir = 0;
fx_esq = 0;
fy_esq = 0;
for ii = 1:num_x
        x_ii = x_nod(1,ii);
        y_ii = x_nod(2,ii);

        % condilo esquerdo
        if ( (x_ii < midle_x) && (y_ii < lower_y) )
                fx_esq = fx_esq + f_reac(2*ii-1,1);
                fy_esq = fy_esq + f_reac(2*ii-0,1);
        end


        % condilo direito
        if ( (x_ii > midle_x) && (y_ii < lower_y) )
                fx_dir = fx_dir + f_reac(2*ii-1,1);
                fy_dir = fy_dir + f_reac(2*ii-0,1);
        end
end

fx_dir
fy_dir
fx_esq
fy_esq
```

2. Routine used to calculate the stress and shear stress (σ_{xx}, σ_{yy}, σ_{zz}, τ_{xy}, τ_{yz}, τ_{zx}), the von Mises stress (σ_{ef}) and the main stress (σ_1, σ_2, σ_3), at the integration points. Firstly, two points are defined (x_int) and then a cycle through all integration points is made, and the distance between them is calculated (dist(jj,ii)). Finally, the closest integration point to the defined point is selected by calculating the minimum value of all the distances. Having the two integration points, the stress values are then obtained.

```
load('femas10001.mat')

x_int = [ -20   30 ;
          -10  -10 ;
           90   90 ];
num_x_int = 2;

% cycle through all integration points

for ii = 1:num_g
        for jj = 1:num_x_int

                x_gp=gp(1,ii);
                y_gp=gp(2,ii);

                x_jj = x_int(1,jj);
                y_jj = x_int(2,jj);


                dist(jj,ii) = ( (x_jj-x_gp)^2 + (y_jj-y_gp)^2 )^0.5;
        end
end


for jj = 1:num_x_int
[val_min(jj),id_min(jj)] = min(dist(jj,:));
end


% First point tension values
stress(1:6,id_min(1))
stress_ef(1,id_min(1))
stress_pri(1:3,id_min(1))


% Second point tension values
stress(1:6,id_min(2))
stress_ef(1,id_min(2))
stress_pri(1:3,id_min(2))
```

3. This routine has the objective of dividing the tibial model in various groups, making possible for the RPIM formulation to identify domain discontinuities. A loop over all nodes is made and the planar constant D is calculated and compared with the cutting plane (created with three points – A, B and C), dividing the nodes in two groups. Then other conditions (e.g. using point E) are used to divide correctly the model at the respective group.

```
clear all
close all

% load:
load('final_mesh_file.mat')
% e_are  e_nod  e_val  num_e  num_x  x_nod  x_val

% e_val(1,:) --> patch
% e_val(2,:) --> group
% e_val(3,:) --> property
% e_val(4,:) --> material
% e_val(5,:) --> layer

% e_nod(1,:) --> n1
% e_nod(2,:) --> n2
% e_nod(3,:) --> n3
% e_nod(4,:) --> n4

% x_nod(1,:) = x
% x_nod(2,:) = y
% x_nod(3,:) = z

% x_val(1,:) --> patch
% x_val(2,:) --> group
% x_val(3,:) --> property
% x_val(4,:) --> material
% x_val(5,:) --> layer


load('mater_groups_file.mat')

grp = 1;
mater_groups_array(grp,1) = 3; % how many groups group 1 sees
mater_groups_array(grp,2) = 1; % it sees g1
mater_groups_array(grp,3) = 2; % it sees g2
mater_groups_array(grp,4) = 3; % it sees g3
mater_groups_array(grp,5) = 1; % it sees g1

grp = 2;
mater_groups_array(grp,1) = 2; % how many groups group 2 sees
mater_groups_array(grp,2) = 2; % it sees g2
mater_groups_array(grp,3) = 1; % it sees g1
mater_groups_array(grp,4) = 2; % it sees g2
mater_groups_array(grp,5) = 2; % it sees g2

grp = 3;
mater_groups_array(grp,1) = 2; % how many groups group 3 sees
mater_groups_array(grp,2) = 3; % it sees g3
mater_groups_array(grp,3) = 1; % it sees g1
mater_groups_array(grp,4) = 3; % it sees g3
mater_groups_array(grp,5) = 3; % it sees g3
```

```
load('mater_struct_file.mat')
mater_struct_array(1,2) = grp; % this indicates how many groups there is..


% defining the plane
A = [ 42.24  -10.63  82.06 ]';
B = [ -22.76  -1.56  54.40 ]';
C = [ -22.76  -0.56  54.40 ]';
E = [ 8.03   -38.75  90.08 ]';

% alfa plane
vab = B-A;
vac = C-A;
n_alf = cross(vab,vac);
norm_n = norm(n_alf);
u_alf = (1/norm_n) * n_alf; % plane director (unit) vector

% plane
% ux*x + uy*y + uz*z = D
D_alf = u_alf(1,1) * A(1,1) + ...
        u_alf(2,1) * A(2,1) + ...
        u_alf(3,1) * A(3,1);

% Loop over all nodes
for ii = 1:num_x

    x_ii = x_nod(1,ii); % coordinates
    y_ii = x_nod(2,ii); % coordinates
    z_ii = x_nod(3,ii); % coordinates

        D_ii = u_alf(1,1) * x_ii + ...
               u_alf(2,1) * y_ii + ...
               u_alf(3,1) * z_ii;

        % condition plane alfa
        if D_ii < D_alf
            x_val(2,ii) = 2; % group 2
        else
            x_val(2,ii) = 3; % group 3
        end

        % conditon of the trocanter
        if y_ii < E(2,1)
            x_val(2,ii) = 3; % group 3
        end

        % right side
        if x_ii > A(1,1)
            x_val(2,ii) = 1; % group 1
        end

        % left side
       if x_val(4,ii) == 2% material 2 is the titanium
           x_val(2,ii) = 1; % group 1
       end

        if x_val(4,ii) == 3% material 3 is the titanium
           x_val(2,ii) = 1; % group 1
        end

       if x_val(4,ii) == 4% material 4 is the titanium
           x_val(2,ii) = 1; % group 1
       end

       if x_val(4,ii) == 5% material 5 is the titanium
           x_val(2,ii) = 1; % group 1
       end

       if x_val(4,ii) == 6% material 6 is the titanium
           x_val(2,ii) = 1; % group 1
       end
```

```
    if x_val(4,ii) == 7% material 7 is the titanium
        x_val(2,ii) = 1; % group 1
    end

    if x_val(4,ii) == 8% material 8 is the titanium
        x_val(2,ii) = 1; % group 1
    end

    if x_val(4,ii) == 9% material 9 is the titanium
        x_val(2,ii) = 1; % group 1
    end

    if x_val(4,ii) == 10% material 10 is the titanium
        x_val(2,ii) = 1; % group 1
    end

    if x_val(4,ii) == 11% material 11 is the titanium
        x_val(2,ii) = 1; % group 1
    end

    if x_val(4,ii) == 12% material 12 is the titanium
        x_val(2,ii) = 1; % group 1
    end

    if x_val(4,ii) == 13% material 13 is the titanium
        x_val(2,ii) = 1; % group 1
    end

    if x_val(4,ii) == 14% material 14 is the titanium
        x_val(2,ii) = 1; % group 1
    end
end


% Loop over all elements
for ii = 1:num_e
    for jj = 1:4
        id_nod = e_nod(jj,ii);
        nod_grp = x_val(2,id_nod); % group of node id_nod

% Loop over all elements
for ii = 1:num_e
    for jj = 1:4
        id_nod = e_nod(jj,ii);
        nod_grp = x_val(2,id_nod); % group of node id_nod
        e_val(2,ii) = nod_grp;
    end
end


save('mater_struct_file.mat', 'mater_struct_array');
save('mater_groups_file.mat', 'mater_groups_array');
save('final_mesh_file.mat', 'e_are', 'e_nod', 'e_val', 'num_e', 'num_x', 'x_nod', 'x_val');
```

4. Routine used to save the deformed mesh (update geometric configuration) after applying the 10mm displacement, opening the tibia. Also, the routine calculates the magnitude of the reaction forces, in directions *xx*,*yy* and *zz*, that are resultant from the displacements with the equation: $\boldsymbol{f} = \boldsymbol{Ku}$ ($reac_{force} = k\_mat * displ\_v$). At the end, the total force magnitude is calculated, and those force components are divided by 4. This force is called Surgical Force at the present work.

```
load('femas10001.mat');
% displ_v

load('stiff_mat_file.mat');
%k_mat

load('final_mesh_file.mat');
% e_are, e_nod, e_val, num_e, num_x, x_nod, x_val

%actualize mesh nodes
x_nod_new = zeros(3,num_x);
for ii=1:num_x
x_nod_new(1,ii) = x_nod(1,ii) + displ_v(3*ii-2,1); % x
x_nod_new(2,ii) = x_nod(2,ii) + displ_v(3*ii-1,1); % y
x_nod_new(3,ii) = x_nod(3,ii) + displ_v(3*ii-0,1); % z
end
x_nod  = x_nod_new;

save('final_mesh_file.mat', 'e_are', 'e_nod', 'e_val', 'num_e', 'num_x', 'x_nod', 'x_val');



% reaction force
reac_force = k_mat * displ_v;

% reaction force global vector and magnitude
mag_reac_x = 0;
mag_reac_y = 0;
mag_reac_z = 0;
mag_reac_g = 0;
for ii = 1:num_x
        if ( x_nod_new(3,ii) > 50 && x_nod_new(3,ii) < 80 )
                mag_reac_x = mag_reac_x  + reac_force(3*ii-2,1); % x
                mag_reac_y = mag_reac_y  + reac_force(3*ii-1,1); % y
                mag_reac_z = mag_reac_z  + reac_force(3*ii-0,1); % z
        end
end

mag_reac_g = ( (mag_reac_x )^2 + (mag_reac_y )^2 + (mag_reac_z )^2 )^0.5;


mag_reac_x
mag_reac_y
mag_reac_z
mag_reac_g

(mag_reac_x)/4
(mag_reac_y)/4
(mag_reac_z)/4
(mag_reac_g)/4
```